In situ TEM studies on the graphitization and growth of nanocrystalline graphene from polymers

TECHNISCHE UNIVERSITÄT DARMSTADT

Dissertation approved by the department of
Materials and Earth Sciences
in fulfilment of the requirements for the degree of
Doctor-Engineer
(Dr.-Ing.)
By

Shyam Kumar Chethala Neelakandhan
M.S. in Material Science
Born on February 04, 1986 in Kerala, India

Referee:	Prof. Dr. Ralph Krupke
Co-referee:	Prof. Dr. Christian Kübel

Date of submission: 18.06.2019
Date of oral exam: 29.07.2019
Darmstadt 2019
D19

Erklärung zur Dissertation

Hiermit versichere ich, dass ich meine Dissertation selbständig und nur mit den angegebenen Quellen und Hilfsmitteln angefertigt habe. Die Arbeit wurde bisher keiner anderen Prüfungsbehörde vorgelegt und noch nicht veröffentlicht.

Darmstadt, 18.06.2019

Shyam Kumar Chethala Neelakandhan

Abstract

Graphitization of polymers is an efficient way to synthesize graphenoid (graphene like) materials on different substrates with tunable shape, thickness and properties. [1] This catalyst-free growth results in domain sizes of a few nanometers and has been termed nanocrystalline graphene. Ease of fabrication, better control of shape, thickness and properties comparable to graphene makes ncg an easy to produce alternative for graphene for different technological applications. Since the properties of these graphitized carbon structures are largely affected by the domain size and other defects, a detailed understanding of the graphitization and domain growth as a function of temperature is essential to tailor the properties of the graphitic material. In the present thesis, *in situ* TEM techniques are employed to understand the graphitization and domain growth of free-standing nanocrystalline graphene thin films prepared by vacuum annealing of a photoresist inside a TEM. HRTEM, selected area electron diffraction (SAED) and electron energy loss spectroscopy (EELS) techniques are used to analyze the graphitization and the evolution of nanocrystalline domains at different temperatures. By *in situ* heating and current annealing, the present study tries to understand the graphitization and structural changes in the intermediate to ultrahigh temperature range.

The *in situ* studies showed that the graphitization process is highly dynamic in nature with a number of intermediate reactions leading to the formation of different carbon nanostructures. The free-standing membrane showed comparable graphitization to substrate supported films and a two-step growth mechanism was identified. At intermediate temperatures (600-1000 $^{\circ}$C) crystallite growth proceeds by consuming amorphous carbon around the crystallites and at high temperatures (1000- 1200 $^{\circ}$C) growth proceeds by merging of crystallites. The amorphous carbon transforms in two ways, by attaching to the active edges of domains and by catalyst free transformation on the top of graphitic layers. This catalyst free transformation forms new graphitic structures with different size shape and mobility. Some of these carbon nano structures are highly mobile on top of the already graphitized layers, which enabled to study the interaction of these structures with the graphitic substrate at high temperatures.

Time resolved HRTEM investigation of the high temperature dynamics of ncg supported by atomistic simulations gave insights into the fundamental processes controlling the graphene growth, high temperature

stability/mobility of the carbon nanostructures and their interaction with the graphitic substrate. High temperature *in situ* HRTEM investigations revealed the formation of graphene nano flakes and cage-like nano structures during graphitization. The study showed that the growth of the domains is mainly by the migration and merging of the graphitic subunits. In addition to lateral merging of domains, experiments also showed a merging of small flakes with an under laying substrate edge, which involves a slow vertical material transfer. In addition to this, strong structural and size fluctuations of individual graphitic subunits at high temperatures were observed. Graphene nano flakes are highly unstable and tend to loose atoms or groups of atoms, while adjacent larger domains grows by the addition of atoms indicating an Ostwald type of ripening occurring in these 2D materials as an additional growth mechanism. Beam off experiments confirmed that the observed dynamics are inherent temperature driven processes and the electron beam only provides additional activation energy increasing the reaction kinetics. Molecular dynamic simulations carried out to estimate the activation energy for the different processes indicates a critical role of defects in the substrate for the observed dynamics.

Furthermore *in situ* current annealing of free-standing ncg constrictions were carried out to understand the dynamics and structural changes at ultrahigh temperatures. Current annealing provides the possibility to reach temperatures in excess of 1200 ºC inside the TEM, which is the maximum temperature possible by commercial MEMS based heating chips. The graphitization at high temperature is comparable to the thermal annealing showing similar crystallite size evolution. However, growth of domains up to 50 nm was observed with current annealing to ultra-high temperatures (T > 2000 ºC). Unlike the formation of well oriented graphite during high temperature annealing, in current annealing of thick samples, formation of large multi walled cage-like structures were observed. The thickness of the sample and the heating rate seems to have a critical influence on the structural evolution during current annealing. These initial observations on comparable graphitization during current annealing at intermediate temperatures, growth of domains, formation of cage-like structures etc., open up new possibilities to tailor the microstructure and conductivity by controlling the thickness and heating rate of the sample.

Table of contents

Table of figures

List of symbols and abbreviations

2D	Two-dimensional
3D	Three-dimensional
ADF-STEM	Annular dark field scanning transmission electron microscopy
AE	Auger electrons
AFM	Atomic force microscopy
BF-STEM	Bright field scanning transmission electron microscopy
BF-TEM	Bright field transmission electron microscopy
BSE	Backscattered electron
CCD	Charged coupled device
CL	Cathodoluminescence
CNT	Carbon nanotube
CRT	Cathode ray tube
Cs	Spherical aberration
CTF	Contrast transfer function
CVD	Chemical vapor deposition
d	Interplanar distance
eV	electron volt
DF-TEM	Dark field transmission electron microscopy

e	Euler's number (≈ 2.71828183)
Ea	Activation energy
EBSD	Electron backscatter diffraction
EDX	Energy dispersive X-ray spectroscopy
EELS	Electron energy loss spectroscopy
EFTEM	Energy filtered transmission electron microscopy
ELNES	Energy loss near edge spectra
E_s	Spatial coherence envelop function
E_t	Temporal coherence envelop function
EXELFS	Extended energy loss fine structure
FEG	Field emission gun
FFT	Fast Fourier transforms
FIB	Focused ion beam
g	Spatial frequency
GIF	Gatan imaging filter
GNF	Graphene nano flake
H	Planks constant
HAADF-STEM	High angle annular dark field scanning transmission electron microscopy

HRTEM	High resolution transmission electron microscopy
I_D	Intensity of D peak
I_G	Intensity of G peak
K_b	Boltzmann constant
La	Crystallites size
Lc	Stacking thickness
m_0	Rest mass of electron
MDS	Molecular dynamics simulation
MEMS	Microelectromechanical system
MWCNT	Multi walled carbon nano tube
ncg	Nanocrystalline Graphene
NEB	Nudged elastic band
NEMS	Nanoelectromechanical system
PGMEA	Propylene glycol monomethyl ether acetate
PMMA	Poly methyl methacrylate
SAED	Selected area electron diffraction
SAM	Self assembled molecule
SE	Secondary electron
SEM	Scanning electron microscope

SiLi	Lithium drifted silicon (detector)
SMD	Steered molecular dynamics
STEM	Scanning transmission electron microscopy
t	Thickness of sample
ν	Rate constant
v	Velocity
V	Voltage
ν_0	Pre exponential factor
Vp	Projected crystal potential
XRD	X-ray diffraction
Z	Defocus
β	Semi-angle of collection of the magnifying lens
δ	Resolution of microscopy
θ	Incident angle of X-ray
λ	Radiation wavelength
σ	Interaction potential
ψ_e	Exit wave function
μ	Refractive index of the viewing medium

1. Introduction

1.1. Introduction

More than a decade since its first successful exfoliation, graphene continues to be an interesting material for different technological applications because of its unique properties. [2,3] Graphene is a sp^2 hybridized single layer of carbon arranged on a hexagonal lattice. Graphene can be regarded as the fundamental building block for other carbon nano structures like fullerene and carbon nano tubes. This 2D carbon allotrope has been explored in different applications such as electronics, photonics, composite materials and coatings, energy generation and storage, bio applications etc. to name just a few. [4,5]

The main reason for the interesting properties of graphene is its unique structure. Carbon is tetravalent with four outer shell electrons and these electrons bond differently to make different allotropes of carbon. The six electrons in carbon occupy the $1s,2s,2p_x,2p_y,2p_z$ orbitals in ground state with configuration $1s^2 2s^2 sp^2$. In graphene, the sp^2 hybridization leads to a trigonal planar structure consisting of a double occupied 2s orbital and two 2p orbitals. The structure consists of three in-plane σ bond between the two neighboring carbon resulting in short inter atomic covalent bond separated by 1.42 Å. This gives graphene its remarkable mechanical properties. The fourth bond is a π bond, formed by the $2p_z$ orbitals that are perpendicular to the planar structure and since each p orbital has one extra electron, the π band is half filled. This peculiar structure leads to interesting electronic properties in graphene. The band structure of graphene calculated using tight binding approach shows that it is a zero band gap semiconductor in which the conduction band and valance band meet at Dirac points. [4,5]

Because of this peculiar structure, graphene has outperformed existing materials in different field with some properties reaching close to the theoretical predicted values. Graphene shows superior electronic and optical properties, ultrahigh intrinsic strength, superior thermal conductivity and can sustain very high current densities. The room temperature electron mobility is 2.5×10^5 V^{-1} s^{-1} [6] and thermal conductivity is above 3000 W mK^{-1}. [7] Mechanical properties are also interesting with a Young's modulus of 1 TPa and an intrinsic strength of 130 GPa. [8] It is also impermeable to any gas and can be easily functionalized chemically to tune the properties. [2]

These interesting properties are for a defect free graphene and different top down and bottom up approaches have been used to synthesis graphene. [4] All these techniques involve a transfer process which induces defects and contamination on the graphene and is difficult to integrate in production. Thus the efficient use of these unique properties are largely hindered by the challenges involved in successfully transferring defect/contamination free graphene to various substrates for reliable device fabrications.

Graphitization of polymers in small length scales to synthesize graphenoid (graphene like) materials, emerged as an easy to fabricate alternative for graphene. [9,10] This method provides the flexibility of growing on different substrates with defined thickness and also for patterning to achieve different shapes. [10,11] Recently, thin graphitized films with comparable properties to graphene have been fabricated by pyrolysis of polymer films. [1,11] The catalyst-free growth results in a material with domain sizes of a few nanometers, which has been termed nanocrystalline graphene (ncg). The ease of fabrication, control over size, shape and thickness, and the possibility to tailor the properties by varying the polymer precursor and the graphitization temperature has made this material a potential alternative for polycrystalline graphene in different areas.

With the increasing application of polymer pyrolyzed ncg thin films, it becomes important to have a proper understanding of the structure, structural evolution during pyrolysis and structure property correlation in these materials. High resolution (scanning) transmission electron microscopy (HR(S)TEM) has already shown its effectiveness characterizing carbon nanostructures with sub-angstrom resolution. [12,13] Specifically in the case of graphene, HRETM/STEM was pivotal in understanding the nature of defects [14], edge structure [15] and defect dynamics (Figure 1.1) [16] Furthermore, development of Low voltage HRTEM facilitated the characterization of graphenoid materials without inducing significant beam damage or defects. [17,18] The improvements in resolution, analytical capabilities and *in situ* techniques made TEM a favorite candidate for the characterization of carbon nano materials. In particular, the *in situ* capabilities opened up new possibilities to understand highly dynamic processes, combining imaging and analytical methods. Also, there has been a growing interest to understand the dynamics during *in situ* heating [19,20] and electrical biasing [21,22] of graphene.

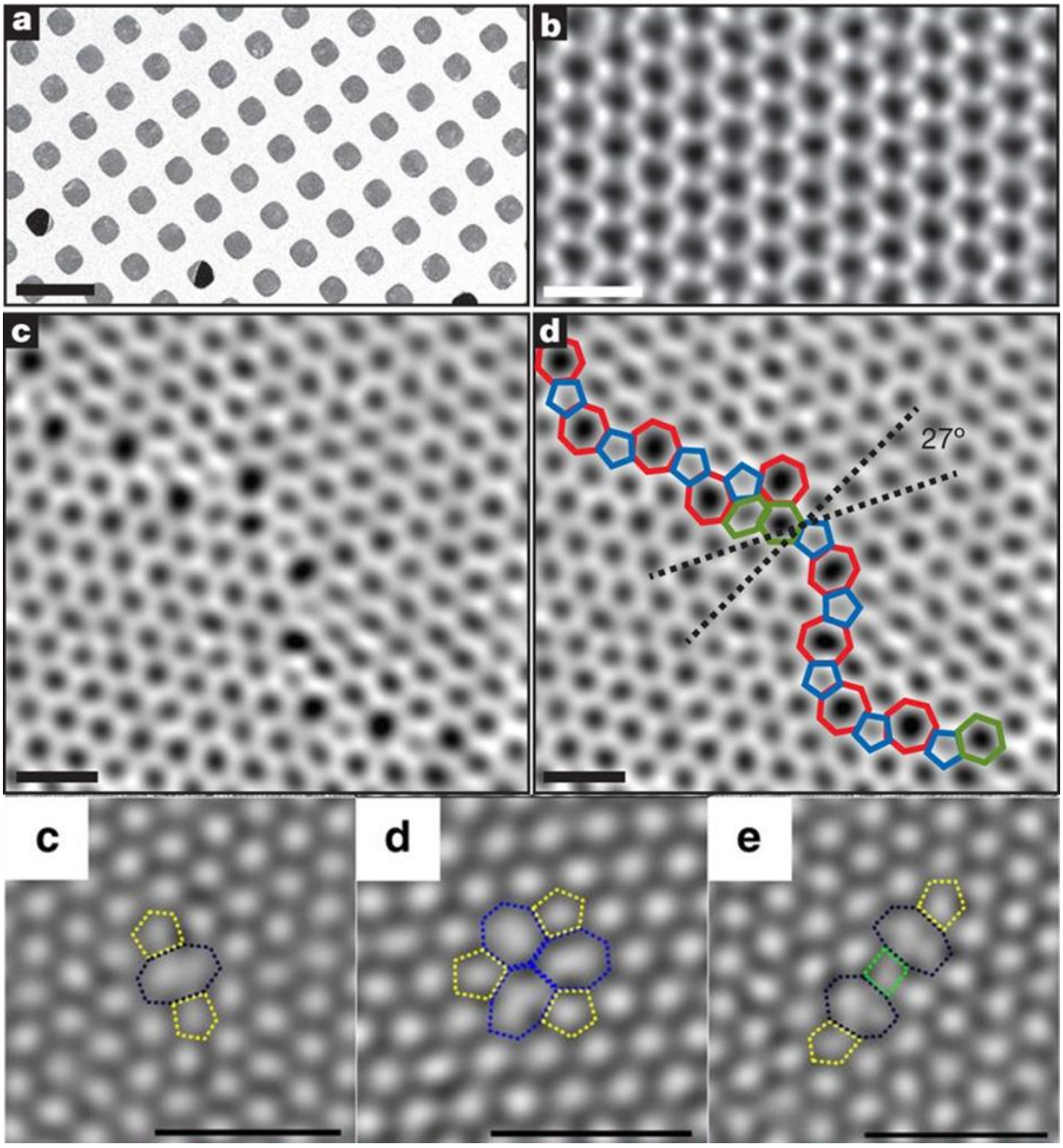

Figure 1.1: Transmission electron micrscopy of graphene (a) SEM image of single layer graphene transfered on to TEM grid, (b) HRSTEM image of the defect free graphene. (c,d) showing a grain boundary missoriented at 27 °. [23] (c-d) showing the transformation of a divacancy under the electron beam. [24]

Even though all these improvements in transmission electron microscopy have been explored well in understanding the structure and dynamics of graphene, these techniques have not been widely used to understand the structural evolution during the pyrolysis of thin polymer films. A proper understanding of structural evolution and structure property correlations during pyrolysis is essential in realizing a property

specific graphenoid material and low voltage *in situ* TEM can be the ideal characterization tool to completely understand this kind of highly dynamic processes. In the present thesis, we employ *in situ* TEM methods to understand the catalyst free formation of free-standing polymer thin films. By combining HRTEM, SAED and EELS, we look in to the chemical and structural evolution during graphitization of ncg. Furthermore with *in situ* current annealing studies, ultra-high temperature dynamics is studied along with understanding the evolution of resistance.

1.2. Structure and properties of ncg

As the name suggests, ncg can be seen as graphene with very small crystallite size. The catalyst free synthesis limits the growth of the crystallites, resulting in crystallite size on the order of a few nanometers as can be seen (Figure 1.2). The structure consists of stacked graphitic layers that are highly defective consisting of lot of defects and disordered edges. The SAED pattern in the inset shows continuous diffuse rings corresponding to the nanocrystalline nature. The Raman signature of ncg shows a G peak, a prominent D peak and a broad 2D peak. The D peak is a defect induced peak and is absent in defect free coarse grained graphene. The presence of a D peak is a signature of nanocrystallinity in ncg and the intensity ratio of the the D and G peak can be used as a measure of nanocrystallinity, where a more pronounced D peak indicates smaller grain sizes.

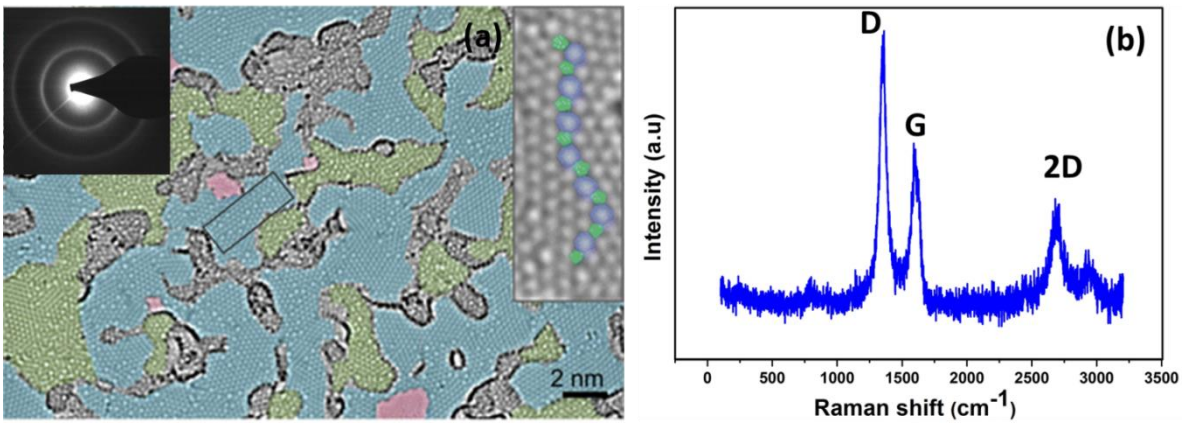

Figure 1.2: (a) HRTEM of ncg [25]and the defective grain boundary with pentagon and heptagon rings. SAED pattern of ncg is shown as inset, (b) Raman spectrum of ncg.

Nanocrystalline graphene shows interesting properties and can be a potential substitute to graphene in different areas such as electronics [1,26], photonics [9,11], strain sensing [11], and as transparent conducting electrodes. [27,28] The reported values for the sheet resistance are in the range of 20-50 $k\Omega/m^2$ for few layers of ncg [11], which is two orders of magnitude higher compared to cvd grown graphene. [29] The higher amount of grain boundaries and defects result in a reduction of the conductivity. Since the sheet resistance depends on the thickness of the film, this can be tuned by varying the thickness, e.g. the sheet resistance can be reduced to 150-200 Ω by increasing the ncg thickness to 180 nm. [1] Thus, the initial polymer structure makes it easy to tailor the resistance of final structure by controlling the thickness. The optical properties of ncg are comparable to graphene. Studies on photocurrent generation under illumination show that the behavior is similar to doped crystalline graphene. [11] Ncg also shows light emission under electrical biasing where the power density and the electron temperature is comparable with crystalline graphene. [11] Compared to crystalline graphene, ncg shows an enhanced piezo resistive effect, which has been attributed to the increased number of grain boundaries. [11] The easy to fabricate nature of ncg has made it a favorite candidate in transparent conducting electrodes also. With suitable conductivity (500 S cm^{-1}) and transmittance (88 %), ncg thin films appear to be a potential replacement for indium tin oxide (ITO), which is expensive and has limited availability.

It is also worth to mention some of the peculiar mechanical properties of ncg due to its nano crystallite size. While considering the two main mechanical properties, toughness and strength, theoretical studies have shown a strong dependence of toughness on the grain size of graphene in the nanocrystalline regime. The grain size dependent variation in toughness is limited only to the nano crystalline regime and after a critical grain size, the toughness is independent of the grain size. [30] The higher amount of grain boundaries and defects results in a flaw insensitive tensile behavior below critical length scales of the notch. [31] This means that the nanocrystalline graphene (grain sizes less than 100 nm) can withstand larger cracks compared to the polycrystalline graphene. In contrast, the strength continues to increase with grain size. This is due to the reduction in the number of grain boundaries and triple junctions, which act as stress concentration centers. These interesting properties in different areas and the ease of manufacturing made ncg an easy to fabricate alternative for graphene in lot of technological application.

1.3. Preparation of ncg

Different carbon sources and processes have been reported for the bottom up preparation of ncg films. Researchers have successfully grown ncg on different substrates such as SiN, Si, MgO Al_2O_3 and SiO_2 using CVD. [28,32–35] There are also studies on growth of ncg using molecular beam epitaxy on Al_2O_3 substrates. [36–38] Recently, polymer pyrolysis emerged as a convenient way to fabricate ncg by the graphitization of aromatic precursors at high temperatures. A wide variety of source materials and process are used for the initial polymer film, which is then graphitized by substrate supported vacuum annealing.

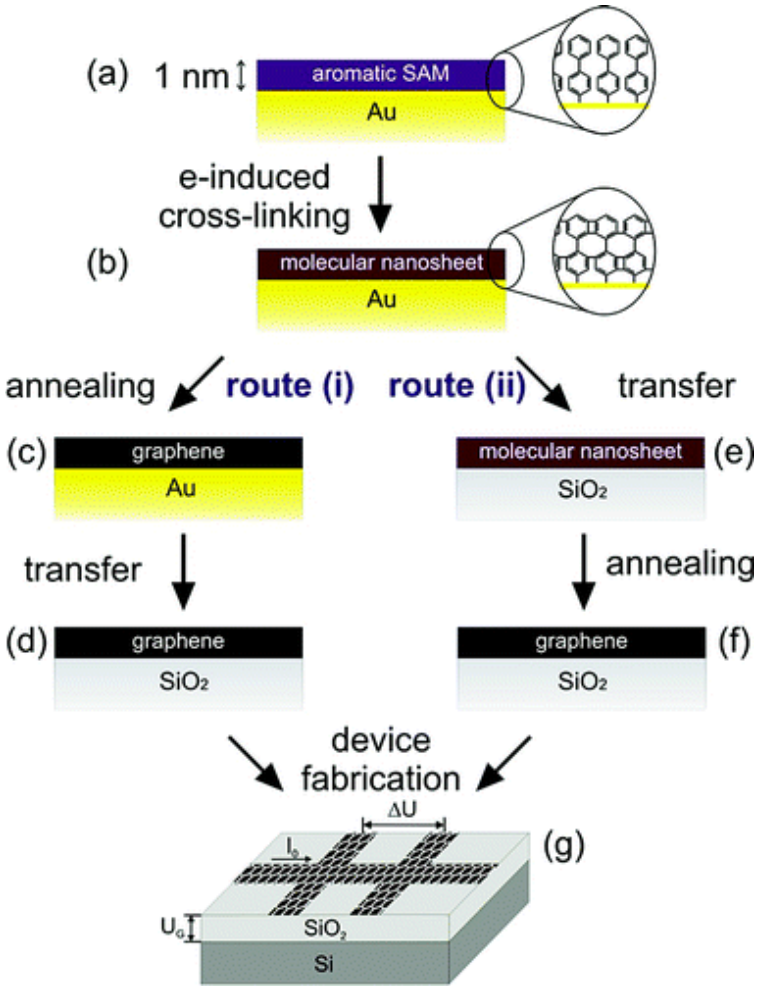

Figure 1.3: Process flow chart of ncg formation using SAMs on gold used by Turchanin *et al*. [25]

Turchanin *et al.*, demonstrated the thermal conversion of aromatic self-assembled monolayers to form nanocrystalline graphene (Figure 1.3). [25,26] These monolayers can be selectively crosslinked using an electron beam to produce desired structures. [39] Even though the process can synthesize very thin graphitized films ranging from 0.5 nm to 3 nm [26], the use of a gold substrate requires a transfer process for most applications, which limits the flexibility. Spin coating emerged as a versatile technique to make thin polymer films, which can be graphitized to form ncg on different substrates (Figure 1.4). [1,11,35,40] The thickness of the graphitized film can be precisely controlled by varying the initial thickness of the polymer. Photoresists and electron beam resists containing aromatic molecules are used as carbon source. This gives flexibility for patterning to different shapes in addition to the thickness control. Inert atmosphere or vacuum annealing is used to graphitize the initial polymer film to form ncg. The thickness reduction ratio is found to be around 1:10 and ncg can be fabricated with different thicknesses ranging from 1 nm to 180 nm. [35] The maximum graphitization temperature used in these studies is 1000 ºC. [1] Different substrates have been used and the graphitization seems to be independent of the substrate. The crystallite size in these studies, measured by Raman spectroscopy and TEM falls within a range of 2-5 nm. [1,11,25]

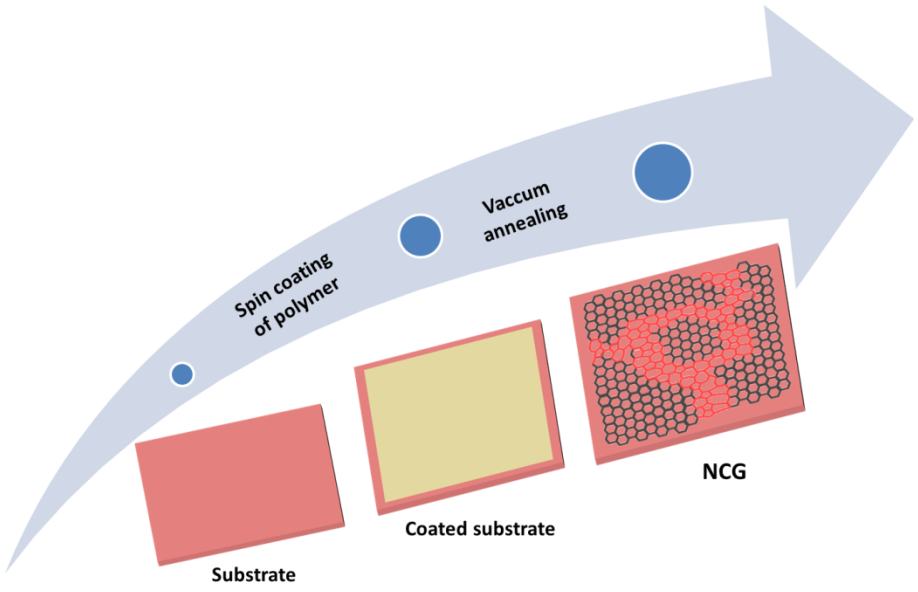

Figure 1.4: Ncg fabrication by the spin coating on substrates.

1.4. Structural evolution during pyrolysis

Pyrolysis refers to the thermal conversion of a material at high temperatures in an inert atmosphere. Pyrolysis of organic materials to form graphite or bulk glassy carbon is a well-studied field. [41–44] Initial pyrolysis studies were focused on the carbonization to form graphite at ultra-high temperatures. [41,45,46] The early precursors studied for graphitization are different types of cokes and chars. Pitch and petroleum coke, cokes prepared from coking coals and char prepared from pyrolysis of polyvinylchloride graphitize completely forming graphite when heated to around 3000 ºC. On the other hand, oxygen rich low rank coals like sugar charcoal and char prepared from polyvinylidene chloride etc. do not result in the development of a three dimensional graphitic structures, but forming highly disordered bulk glassy carbon structures. [47]

The early efforts to characterize the structure of glassy carbon were mainly done with the help of X- ray diffraction. The pioneering work to understand the structure of pyrolyzed carbon was carried out by B.E Warren in early 1940. [48] The structural interpretation was mainly based on the diffuse bands that corresponds to certain (00l) and (hk0) reflections. The proposed structure consists of small graphite-like layers which are arranged in stacks with the layers parallel to one another, but with random orientations. The (hk0) reflections give the crystallite size and the (00l) reflections give the stacking thickness. Later works by R. E. Franklin and the early proposed models were based on the X-ray diffraction data while the models after that were proposed based on TEM images and SAED patterns.

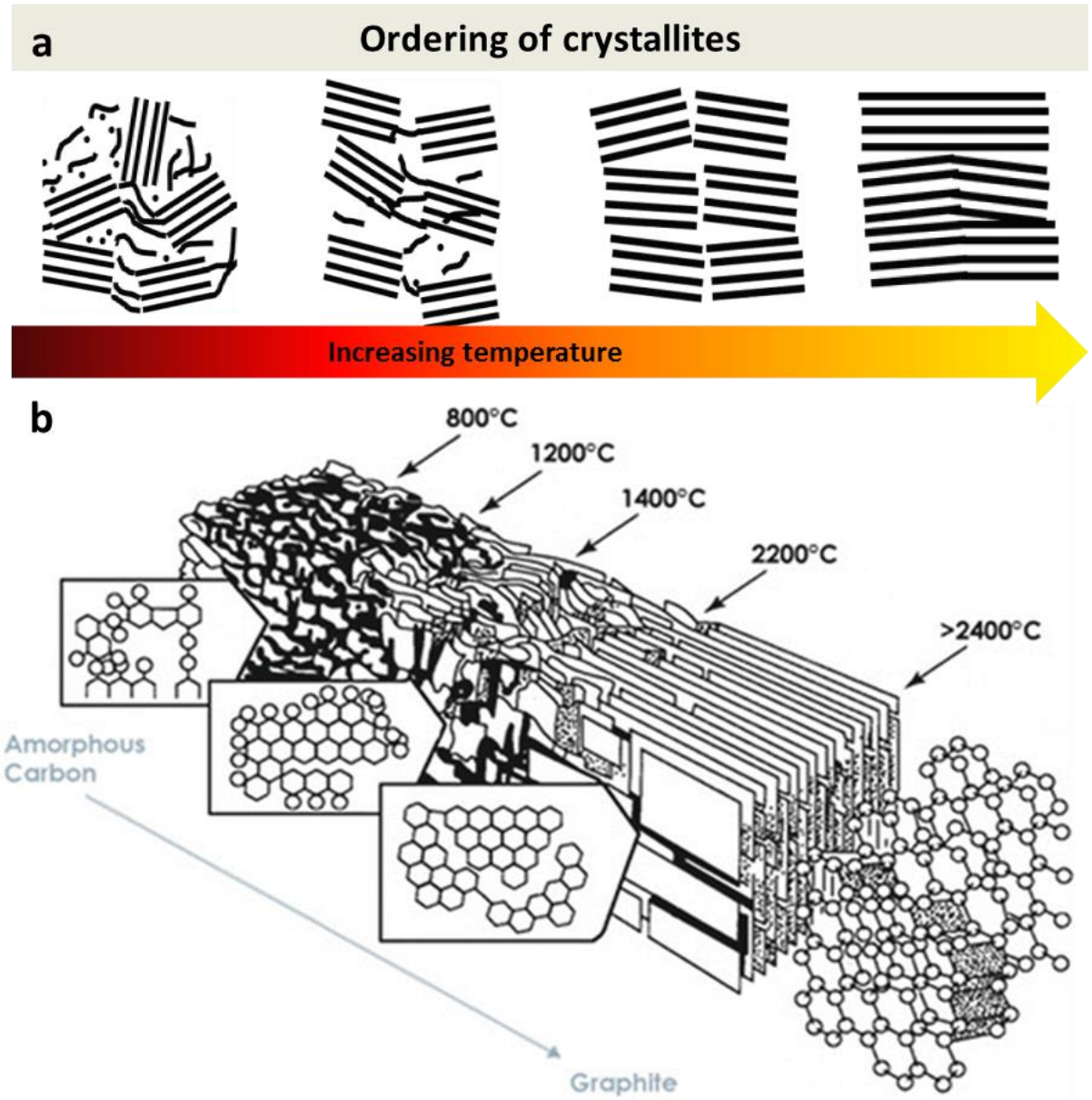

Figure 1.5: (a) Ordering of domains during evolution, (b) the microstructural evolution from an amorphous carbon to graphite during pyrolysis. [49]

According to the model proposed by R. E. Franklin (Figure 1.5). [41], at the initial heating stages, after the evolution of the volatile gasses, a carbonaceous backbone is formed. This serves as an initial structure for further graphitization. After this initial carbonization of the organic material, the structure consists of small misoriented crystallites with the space between them filled by uncoordinated amorphous carbon or voids.

These small crystallites contain up to 3 to 4 layers of hexagonally coordinated aromatic molecules with sizes extending up to a couple of nanometers. The graphitizability of these structures depends on the misorientation and void size between the crystallites. As the temperature increases, at intermediate temperature range, the size and the thickness of the crystallites increase mainly by consuming the amorphous carbon around the crystallites. Further at high temperatures (temperatures > 900 ^{o}C), the graphitization proceeds by the merging of crystallites. In graphitizing carbons, the graphitization will proceed further at very high temperature and crystallites will orient completely leading to the formation of polycrystalline graphite (Figure 1.6). On the other hand, in non-graphitizing carbons, some defects cannot be annealed and the complete orientation of the crystallites cannot happen even at high temperatures. This miss orientated crystallites results in large number of pores and voids and the material remains non-graphitizing with its characteristic low density. [41,43]

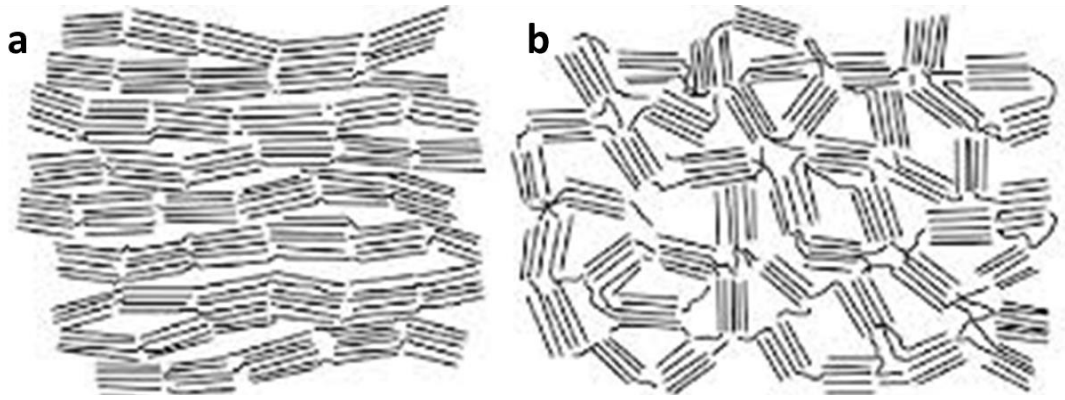

Figure 1.6: Model of (a) graphitizing carbons leading to the formation of graphite and (b) non-graphitizing carbons proposed by Franklin. [47]

The model attributes the graphitizability and non graphitizability to nature of cross linking in initial polymer structure. According to the study, for precursors that can be completely graphitized, the cross linking is weak which increases the mobility of the crystallites leading to an ordered graphitic structure. On the other hand, non-graphitizing carbons are formed from strongly cross linked materials, which immobilize the crystallites and thus hinder the ordering of crystallites and thus complete graphitization. This results in a hard structure with the fine porosity preserved even at high temperatures. Even though the model can explain the structure in a broad sense, it fails to explain the nature of the cross linking and the sharp property difference in graphitizing and non-graphitizing carbons. [47]

The initial pyrolysis studies were focused on complete graphitization to form three dimensionally ordered graphite, the later focus was more on the structure of non-graphitizing carbon. The main motivation for this is to understand the unique properties of the glassy carbon, which include high temperature resistance, low thermal and electrical resistance, low friction, high chemical inertness and very low permeability for liquids and gasses. The development of transmission electron microscopy enabled direct imaging which provided new insights in to the structural evolution during graphitization and models were proposed for non-graphitizing carbon. Glassy carbon models based on curved and twisted graphene flakes were proposed by Jenkins–Kawamura [50] and Ban *et al.* [51] Jenkins–Kawamura proposed a ribbon-like model for glassy carbon based on their HRTEM investigations. In the ribbon model, the thickness of the ribbon is the stacking thickness (Lc) and the width and length of the ribbon describes the crystallite size (La) in lateral dimensions (Figure 1.7a). The model proposed by Ban *et al.* is similar to the ribbon model with curved graphene flakes stacked in different orientations (Figure 1.7b). However, these models raise a number of questions like the high temperature stability of ribbon structures, explanation for closed pores and also the growth of graphene as ribbon rather than as a flake that grows in all directions.

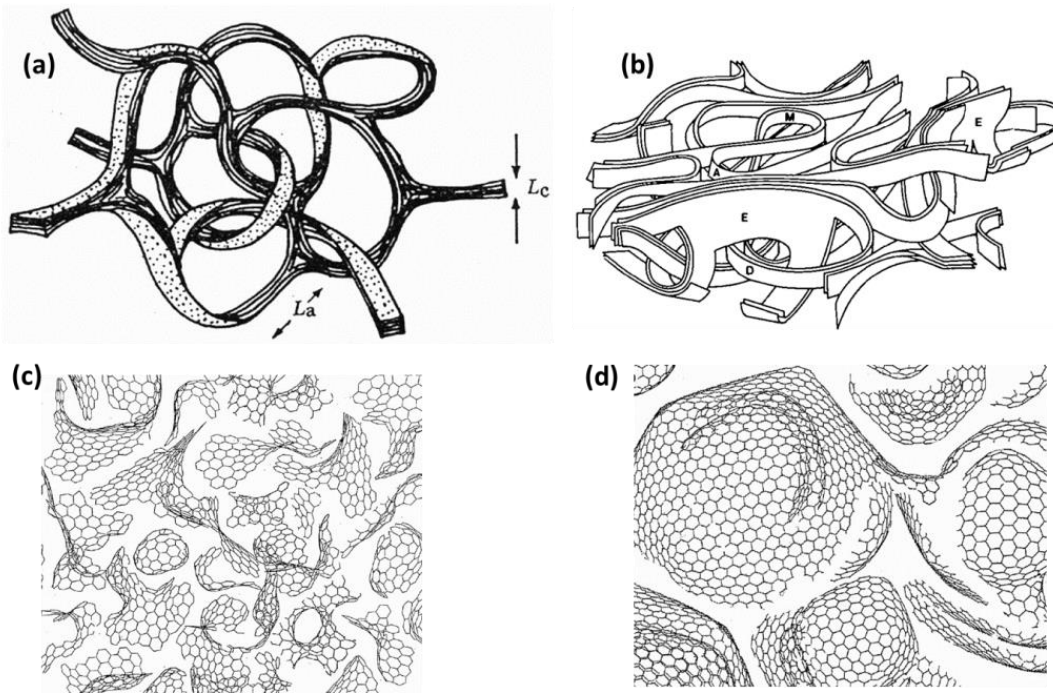

Figure 1.7: (a) Ribbon model by Jenkins–Kawamura, (b) model proposed by Ban et al., low temperature (c) and high temperature (d) fullerene related structure of glassy carbon proposed by Haris et al. [43]

These early studies based on TEM rely on bright field TEM imaging combined with X-ray diffraction. These TEM images largely resolve only the 002 fringes, which gives a ribbon like appearance for the structure. Oberlin *et al.* studied the structure of graphitizable thin carbon films extensively using imaging and diffraction techniques in TEM. [42,46,52] Combining SAED, BF and DF imaging, they proposed a model similar to the one proposed by Franklin, in which the graphitic carbons are built up from basic structural units of small group of planar molecules. A two-step growth mechanism was proposed in which the first step is the establishment of a turbostratic arrangement during the pre-graphitization stage. The structure is turbostratic until 2000 °C and mosaic elements of around 10 Å with 2-3 layers become mostly parallel with twist and tilt boundaries to form distorted layers. These layers are separated by defects such as tetrahedral or dangling bonds. During this pre-graphitizing regime, the thickness (Lc) increases while the crystallite size (La) remains the same. At temperatures above 2000 °C, the twist and tilt boundaries disappear and defects are annealed out resulting in an increase of La. The model ascribes the growth and the disappearance of defects between the layers during low temperature, increasing Lc, and of defects in the layers at high temperatures, increasing La. Even though the model explains the structural evolution of graphitizing carbons well, it fails to explain the non graphitizability of some carbons even at high temperatures.

Improvement in TEM capabilities and the discovery of curved nanostructures such as fullerenes, carbon nanotubes and other nano carbon materials containing stable non-six membered rings, initiated new investigations into the structure of glassy carbon. Based on the high-resolution studies on bulk glassy carbon, Harris *et al.* proposed a fullerene related structure of commercial glassy carbon. [53] This is mainly based on the observation of fullerenes, carbon onions and other curved/close cage structures in the glassy carbon pyrolyzed at different temperatures (Figure 1.7c,d). The model consists of discreet fragments of curved carbon sheets with non-six membered rings that are randomly dispersed between the hexagons. A low temperature model is proposed consisting of a high proportion of discrete fullerene like closed cage structures. This tightly packed microstructure makes the material more impermeable and less reactive. A high temperature structure is proposed with multilayer fullerene related nanoparticles, enclosing the pores, which are much larger than observed in the low temperature structure. The model predicts the presence of completely closed structures contributing to the observed low density of the glassy carbon structures. This model can explain the low density and impermeability of glassy carbon but fails to explain the high conductivity and the graphitizability of certain carbons at high temperatures.

Apart from the previously mentioned examples, there have been a number of efforts to understand the structure of glassy carbon using various characterization techniques. [54–59] It is worth to mention the work by Daniels *et al.*, where he carried out a systematic study on the carbonization and graphitization from an organic precursor using HRTEM EELS and XRD. [59] The variation in carbon core loss near edge spectra as a function of temperature was acquired and analyzed to understand the structural evolution of samples heated to different temperatures. Even though the structure of glassy carbon and structural evolution during pyrolysis have been studied a lot, there remains a lot of interesting questions on the exact structure of the glassy carbon, structure of the pores and edges, the origin of the the graphitizing and non-graphitizing nature of the carbons etc. This necessitates identifying new experimental and analytical methods combining with theoretical simulation studies to have a complete atomistic understanding of the structure and structural evolution.

1.5. Structural changes during passage of current in nano carbon structures

With the increasing interest in carbon MEMS and NEMS systems, graphenoid materials are widely used in different fields and it is necessary to understand the structural changes happening during the passage of current. This is even more important in the case of ncg, which has potential applications in electronics, photonics and transparent conducting electrodes etc. There are a number of studies carried out to understand the effect of passing current through different carbon nanomaterials. The passage of current can induce joule heating and also electron migration of carbon atoms. The high temperatures that can be reached during current annealing can be used as an effective way to tailor the structure and properties of carbons. Out of the different carbon nanostructures, CNT and graphene remains the most studied. Different studies are available on the current annealing of CNTs and graphene and most of them are carried out *in situ* inside the TEM. The early works on CNTs is by Huang *et al.* studying the mechanism of electrical break down and the tensile behavior of carbon nano tubes. The studies on MWCNTs show that the break down proceeds by breaking from the outer most walls to inside dropping the current passing through it. [60] Superplastic tensile behavior during the passage of current is observed when the CNT is strained under biasing. The tensile elongation was 280 % under bias compared to less than 15 % at room temperature. [61]

As in the case of CNTs, there have been growing interests to study the effect of current annealing of graphene and graphene nanoribbons. Early studies investigating the current carrying capacity of few layer

graphene nano ribbons using SEM showed a break down current densities of 10^8 A/cm^2 [62] and current induced control formation of nano gaps in suspended graphene was demonstrated by pulsed electrical break down. [63] While these studies focused more on the electrical properties of graphene during current annealing, information on the structural transformations were limited because of the resolution limit in SEM.

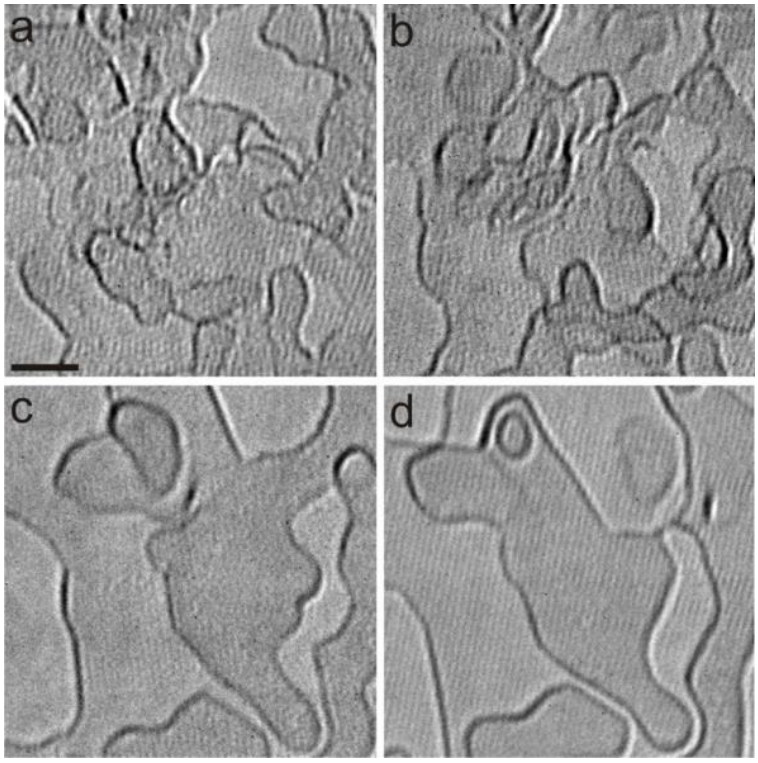

Figure 1.8: (a-d) Transformation of amorphous carbon to highly ordered graphene patches up on current annealing. [64]

Improvement in the *in situ* capabilities in TEM motivated the researchers to look in to the structural changes during current annealing leading to the better structure property correlations. Westenfelder *et al.* studied *in situ* current annealing to find out the structural changes inside the TEM. [65] In the investigations, the graphene sheet serves as both substrate and heating element. At temperatures around 1000 K, hydrocarbons absorbed on the graphene substrate, transformed into amorphous carbon and at higher temperatures a complete catalyst free conversion of the amorphous carbon in to polycrystalline graphene is observed. The study used melting of gold nanoparticles dispersed on the substrate to understand the local temperature profile. [65] Similarly Barreiro *et al.* studied the catalyst free transformation of amorphous carbon

precipitates on the graphene during current annealing (Figure 1.8). [64] The small amorphous carbon precipitates rearrange and crystalize to form polycrystalline graphene at higher temperatures.

Moving forward from understanding the structural changes during current annealing, efforts were taken to correlate the structural changes to the electronic properties on single and few layer graphene. In an early study, the conductance of graphene nano constrictions (GNC) with different widths sculpted by electron beam inside the TEM was studied. [66] GNCs show higher conductance than the exfoliated graphene and sustains high current densities in the order of $100\mu A/nm^2$. A controlled fabrication of mono and few layers of graphene nanoribbons down to a width of 0.7 nm were demonstrated using electron beam sculpting. Few layer graphene nanoribbons show higher conductance and it is attributed to the bonded edges, which provide structural stability and additional conduction channels. The disordered edges of the few layer graphene recrystallized to a sharp highly crystalline structure, increasing the conductance and the study shows that the breakage of the nanoribbons occurs layer by layer breaking of stacks.

The behavior under electrical biasing of bulk graphite was different from graphene. Harris *et al.* extensively studied the effect of electrical current on structural transformation of bulk graphite [67–69]. An arc discharge setup was used to pass current through the graphite and the transformed samples were examined using HRTEM. The studies claim that during current annealing there is transformation from a flat two dimensional to a closed three dimensional structures. [68] The structures consist of hollow three dimensional graphitic shells bounded by curved and faceted planes. Fullerene and carbon nanotube like structures are also observed after the passage of current. [67]

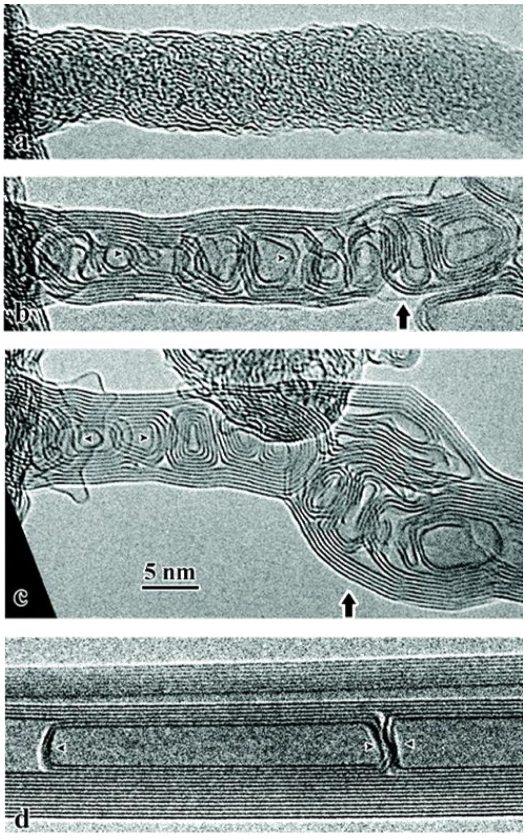

Figure 1.9: (a-d) Transformation of amorphous carbon fiber to a tube like structure up on current annealing. (c) shows the intermediate structure consisting of carbon onions and (d) shows the hollow tube like structure formed. [70]

Current annealing of amorphous and glassy carbon structures are not studied extensively compared to graphene or CNT. One of the early studies shows the formation of tubular structure of the carbon nanowire after current annealing. [70] Initially up on current annealing, crystallization of amorphous carbon outside the tube in to curved graphitic basal plane is observed. The amorphous carbon on the interior crystallized in to graphitic nano onions (Figure 1.9). With increasing power, the structure becomes continuous and parallel forming a structure similar to multi walled nanotubes. The structure shows a continuous increase in conductivity during graphitization.

In another study, amorphous carbon was deposited around the In As nanowire and was resistive heated inside the microscope forming CNTs inside the microscope. [71] Current annealing melts the nano wire and the amorphous carbon around it crystalizes in to carbon nanotubes. The length, diameter and the wall

thickness of the CNT can be precisely controlled by controlling the length, diameter of the nanowire and the deposition of carbon respectively. In another study, vapor grown single carbon fibers were current annealed inside the TEM to understand the structural evolution. [72] Current annealing decreased the resistivity by 3 orders of magnitude with current densities up to 10^6 A/cm^2. The study showed the exfoliation of graphene flakes, mostly bilayer from the skin of the graphitic nano fibers. The suggested mechanism for this exfoliation is the accumulation of charges between the layers leading to the exfoliation of surface layers. Apart from these experimental studies, there are some theoretical studies discussing the sp^2 ordering of highly disordered amorphous carbon precursors. The molecular dynamic simulations studies show that fully disordered carbon networks will self-assemble spontaneously to form highly ordered sp^2 bonded closed networks. [73,74] These theoretical studies also predict the formation of carbon nano onion, carbon nanotubes and graphite sheets from amorphous clusters, amorphous nanowires and amorphous slabs.

These experimental and theoretical studies show the different structural changes and transformations in carbon nano materials due to the passing current. This necessitates a better understanding of the structural changes during the passage of current. A better understanding of structural evolution can not only be helpful to predict the behavior of these materials in different application but also current annealing can emerge as a versatile method to tailor the microstructure by the passage of current.

1.6. Research Objectives

In the recent years, there have been growing interests in polymer pyrolysis at smaller length scales because of the development of new fabrication methods and identification of new applications. These materials have been explored for wide spectrum of applications and new areas are emerging by identifying new properties and fabrication method. The recent developments in these areas go beyond carbon MEMS and NEMS and new spectra of properties and application are identified with the fabrication of glassy carbon metamaterials. [75,76] These developments show the importance of an improved understanding of the polymer pyrolysis, especially the structural evolution and the structure property correlations in these kind of materials.

The different structural models proposed for bulk graphitizing and non-graphitizing carbons and the reasons for graphitizability and non graphitizability are yet to be completely understood. A better understanding of the intermediate structure and the transformation from the amorphous to complete graphitization also needs to be investigated. This can give information about the presence of fullerene like structures and other non-

six membered structures reported previously [43,44,53] The main difficulty in understanding the pyrolysis process is its highly dynamic nature involving a number of intermediate reactions and products at different temperatures. These reactions are inaccessible during the usual *ex situ* analysis. Thus, local *in situ* characterization is necessary to understand the structural evolution during pyrolysis. Imaging and understanding the structural evolution along with intermediate structures and processes can be an initial step towards structure property correlations enabling efficient tailoring of properties. *In situ* studies on the formation of nanocrystalline graphene can be ideal in this regard both as thin ncg films can be ideal for high resolution imaging/spectroscopy and can provide detailed information about the structural changes.

Apart from the in depth understanding of graphitization, nanocrystalline graphene with lot of defects, active edges and carbon nano-structures provides an interesting system to study the high temperature stability/dynamics of carbon nano-structures on the top graphitic substrate. Even though there are a number of studies on the high temperature structure and dynamics of pristine graphene. [24,77–79], only limited studies are there on these kind of highly defective systems. Defects and active edges can greatly influence the fundamental growth mechanisms. Thus with high temperature studies on ncg, we can look into the role of defects on the fundamental growth mechanism of graphene and the high temperature stability/dynamics of carbon nanostructures.

Along with the detailed understanding of structural evolution, it is equally important to understand the structure property correlations during pyrolysis. *In situ* current annealing studies can be used not only to understand the evolution of resistance during graphitization but also to induce joule heating to reach ultra-high temperatures in side TEM. Reaching ultrahigh temperatures by current annealing can increase the crystallite size and make ncg similar to polycrystalline graphene. This also helps to understand the structural evolution from the intermediate temperature range to the ultra-high temperature. By reaching ultrahigh temperatures by current annealing experiments, a complete understanding of the graphitization trajectory from the intermediate temperature to ultrahigh temperature can be achieved. This not only provides information about the graphitization and growth of ncg but also provides a comprehensive knowledge about the pyrolysis process in general.

The next chapter in the thesis, chapter 2 is intended to give an overview of the different experimental methods used in the present study. The chapter introduces TEM with detailed description of the background

and working principle of different imaging and analytical techniques in transmission electron microscopy. *In situ* transmission electron microscopy and the state of the art in *in situ* heating and current annealing techniques are also discussed in detail. Apart from TEM, the chapter introduces Raman spectroscopy and a brief description of electron beam lithography technique.

Chapter 3 discusses the graphitization and growth of free-standing nanocrystalline graphene. Firstly, the chapter discusses in detail the sample preparation method for fabrication free-standing thin films for *in situ* graphitization. The challenges involved and the optimizations of parameters are discussed. The chapter further discusses the *in situ* graphitization and the study on the structural evolution during the graphitization process by *in situ* TEM techniques. HRTEM, selected area electron diffraction (SAED) and electron energy loss spectroscopy (EELS) techniques are used to analyze the graphitization and the evolution of nanocrystalline domains at different temperatures.

By means of time resolved *in situ* transmission electron microscopy investigations, supported by atomistic simulations, chapter 4 shows the influence of reactivity of defects and unsaturated edges on the dynamics of ncg during high temperature heating. Different dynamics observed such as migration/merging of nanostructures, Ostwald like ripening etc. are discussed in detail. The effects of electron beam in the observed dynamics are analyzed by conducting beam off experiments. Furthermore, atomistic simulations are used to understand the activation energy associated with different process.

Chapter 5 discusses about the initial results on the ultra-high temperature dynamics of ncg using *in situ* current annealing experiments. Sample preparation for the *in situ* current annealing experiments are discussed with challenges faced and optimized parameters. The chapter further proceeds by understanding the structural evolution and evolution of resistance during current annealing. The results show an effect of thickness of the sample and the heating rate on the structural evolution during current annealing and possible mechanisms responsible are discussed.

Chapter 6 provides the conclusions of thesis and gives an outlook and future work.

2. Experimental Methods

2.1. Transmission electron microscopy- a brief history

In 1931 Max Knoll and Ernst Ruska demonstrated the first working transmission electron microscope and used an electron beam instead of visible light as a source for imaging. [80] The first commercially available electron microscope was produced by Siemens in 1939. Transmission electron microscopy became popular with the development of different sample preparation techniques to produce thin electron transparent samples. Improvements in sample preparation techniques and resolution resulted in lattice imaging of crystals and identification of dislocations. [81] Later, developments in optics improved the resolution of TEM, also the first practical STEM was developed in the late 1960s and became commercially available in the 1970s. In parallel, there was developments in combining analytical techniques like X-ray (EDX) spectroscopy [82] and EELS [83] with TEM. A major development in the history of TEM was the introduction of aberration correctors capable of correcting spherical aberrations during late 1990s, which improved the resolution limits further. [84] Today with the developments in sample preparation and instrumentation, sub angstrom resolution is reached with the capability of atomic scale analytical measurements. Also, there has been a growing interest in developing low voltage electron microscopes with improved resolution to reduce the beam induced damage and transformation when viewed with high energy electron beams. [85] With the possibility of atomic resolution imaging and analytical capabilities, transmission electron microscopy is one of the main structural characterization tool used in wide range of research areas.

2.2. Interaction of the electron beam with matter

To understand the different imaging and analytical techniques, we need to consider the interaction of the electron beam with the sample and the radiation emerging out of this interaction. This interaction produces different signals containing a variety of information about structure and chemistry of the sample. Figure 2.1 shows the radiation emerging from the interaction of the electron beam with a thin specimen. Unlike bulk samples, when the sample is sufficiently thin, the sample becomes electron transparent and most of the electrons will be transmitted through the sample. These transmitted electrons carry chemical and structural information and is used for different imaging and analytical techniques.

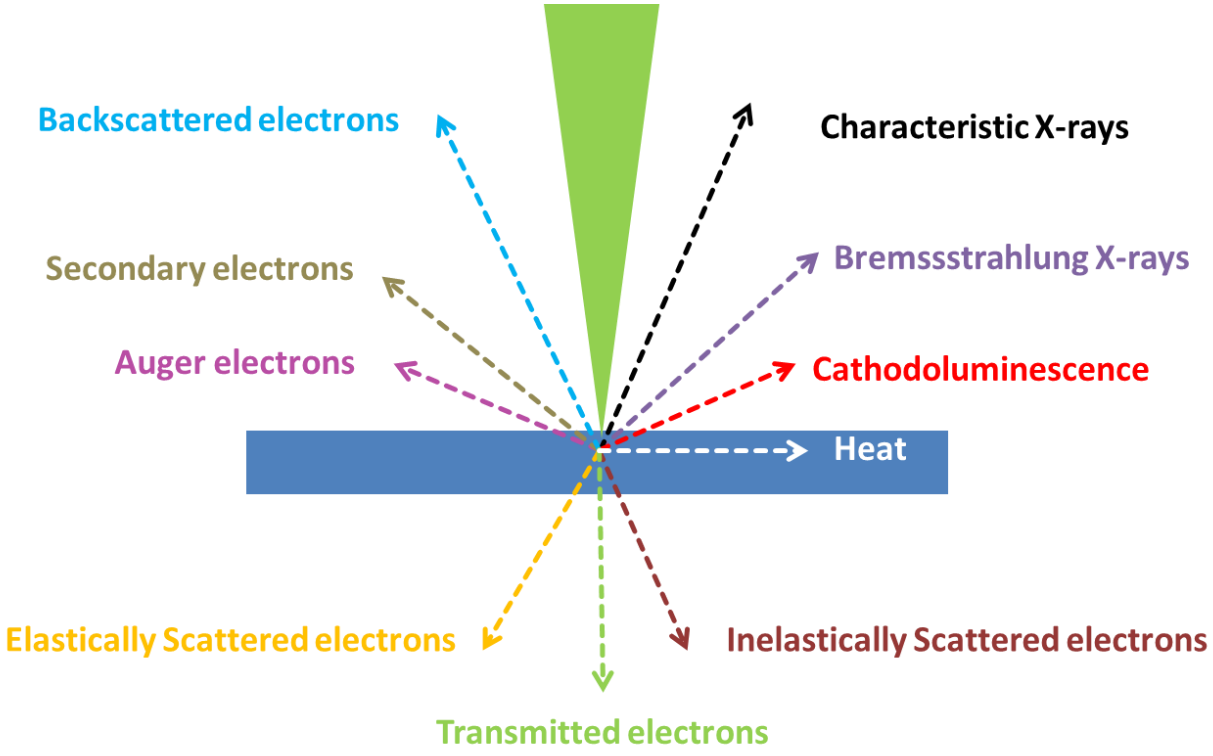

Figure 2.1: Interaction of the electron beam with a thin sample.

The interaction of the electron beam with the sample can be broadly classified into two types: elastic interactions and inelastic interactions. While the elastically scattered electrons are mainly used for imaging purpose, the inelastically scattered electrons are used for analytical purposes. During an elastic interaction, no energy is transferred from the beam to the sample. The elastic scattering/diffraction is the result of two types of interactions: the weak coulomb interaction between the incoming electron and the positive potential inside the electron cloud (Figure 2.2) and the strong interaction with the atomic nuclei (Rutherford scattering). The scattering angle changes depending on the projected potential. The closer the electron comes to the nucleus, the higher the scattering angle. If the sample is sufficiently thin for TEM analysis, most of the electrons do not undergo any deflection and form the so called unscattered or direct beam. Some of the electrons close to the nucleus can be back scattered by the nucleus in the direction of the incoming electron. These are high energy electrons with same energy as the incident electron. The probability of back scattering depends on the atomic number of the atom. For higher atomic number elements the probability for back scattering increases. During elastic scattering, coherent scattering processes will result in constructive and

destructive interference of the electrons deflected by ordered atomic planes, which gives rise to a diffraction pattern analogously to X-ray diffraction, which will be explained in more detail in section 2.4.2

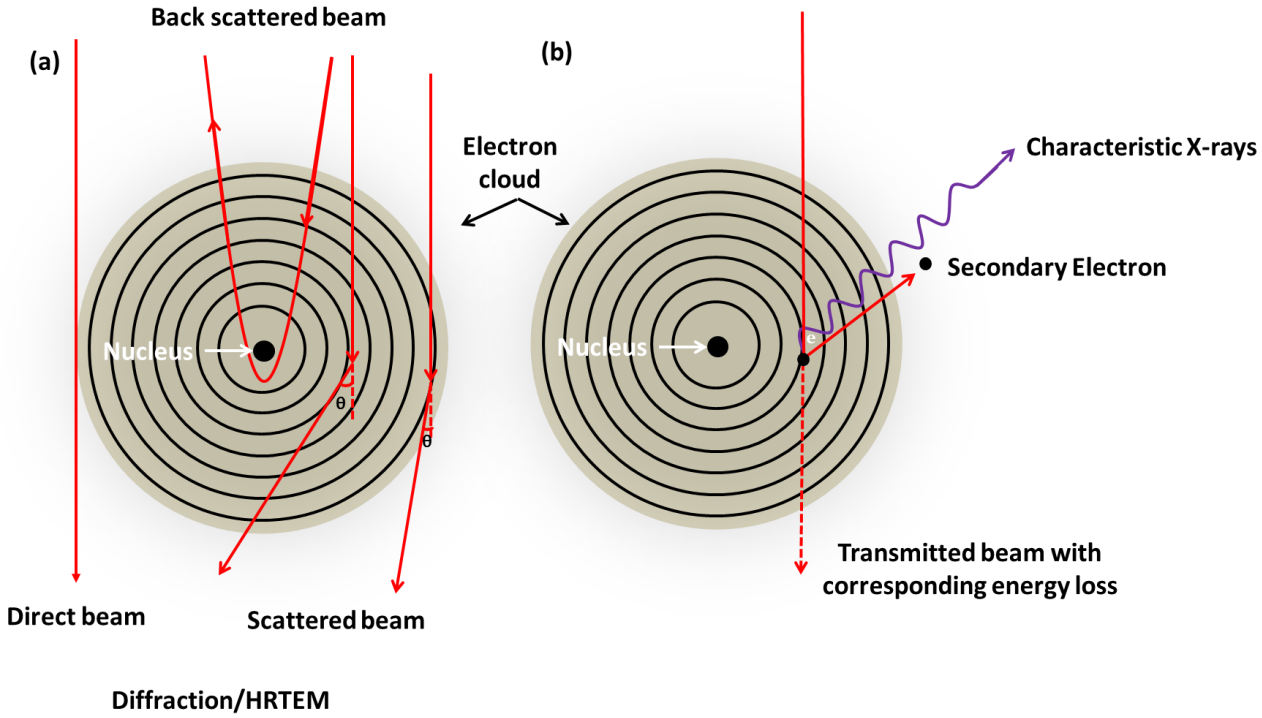

Figure 2.2: Atomic model for (a) elastic and (b) inelastic interactions.

During inelastic interaction, there is an energy transfer from the incident electrons to the specimen leading to a number of emitted signals containing structural and chemical information on the sample (Figure 2.1). These signals can be collected with different detectors to understand the structure and chemistry of the samples. Secondary electrons can be ejected because of inelastic scattering when an incident electron transfers enough energy to knock out an electron from the atom. Closely related, the excitation of an electron from an inner shell of the atom to an antibonding orbital takes it to an excited state. This inner shell vacancy will be filled by an outer shell electron and the corresponding energy difference will be emitted in the form of electromagnetic radiation (X-ray or photon). This energy is characteristic for a particular element and can be used to determine the elemental composition. Apart from the emitted signals, the transmitted beam can also be used for chemical and structural characterization of the material. The transmitted beam experiences an energy losses corresponding to the different elastic interactions and can be measured using

electron energy loss spectroscopy (EELS). While providing valuable information on the structure and chemistry of the material, the energy transfer from the incident beam can cause undesirable structural and chemical changes in the material. This is commonly referred to as beam induced transformation and can cause significant damage to the sample under observation. These beam induced transformations are discussed in detail in section 2.7.

2.3. Transmission electron microscopy - design and principles

Figure 2.3 shows a schematic representation of a TEM, similar to the one used in the present study. The source for the electrons is a field emission gun, which emits electrons from a very fine tip with a strong applied electric field. The FEG tip is made of tungsten with a thin layer of zirconia, which reduces the work function of the tip. The electrons are extracted by applying a positive potential on the extractor anode. The FEG is heated to a temperature of 1800 ºC in order to increase the number of electrons emitted and to reduce contamination on the tip. Compared to conventional thermionic sources, FEG sources have a higher brightness, greater coherence and lower energy spread. The extracted electrons are further accelerated by an accelerator unit, which determines the operation voltage of the microscope.

The electron beam is shaped by the condenser system, which consists of the condenser lenses and condenser apertures. Conventional TEM consists of two condenser lenses which control the beam diameter, intensity and convergence angle. In modern microscopes, a 3rd condenser lens is introduced which enables (almost) independent optimization of beam current, diameter and convergence angle, enabling a Köhler like illumination of the sample. Spot size and the convergence angle are controlled by changing the crossover between the condenser lenses thereby changing the part of the beam going through the apertures below. The third condenser lens is followed by the mini condenser lens and the upper objective lens. The objective lens is split into two parts, the upper and lower objective lens with the specimen in between them. The mini condenser lens is needed in order to switch between TEM and STEM mode. While the upper objective lens is essential to form a fine probe for STEM imaging, the upper objective lens would not be strong enough to enable a parallel illumination for large area TEM imaging. Therefore, the mini condenser lens is used to improve the flexibility of the illumination system, by providing additional focusing or defocusing of the beam when switching between STEM or TEM mode. The STEM coils allow the beam to be scanned across the sample in the STEM mode.

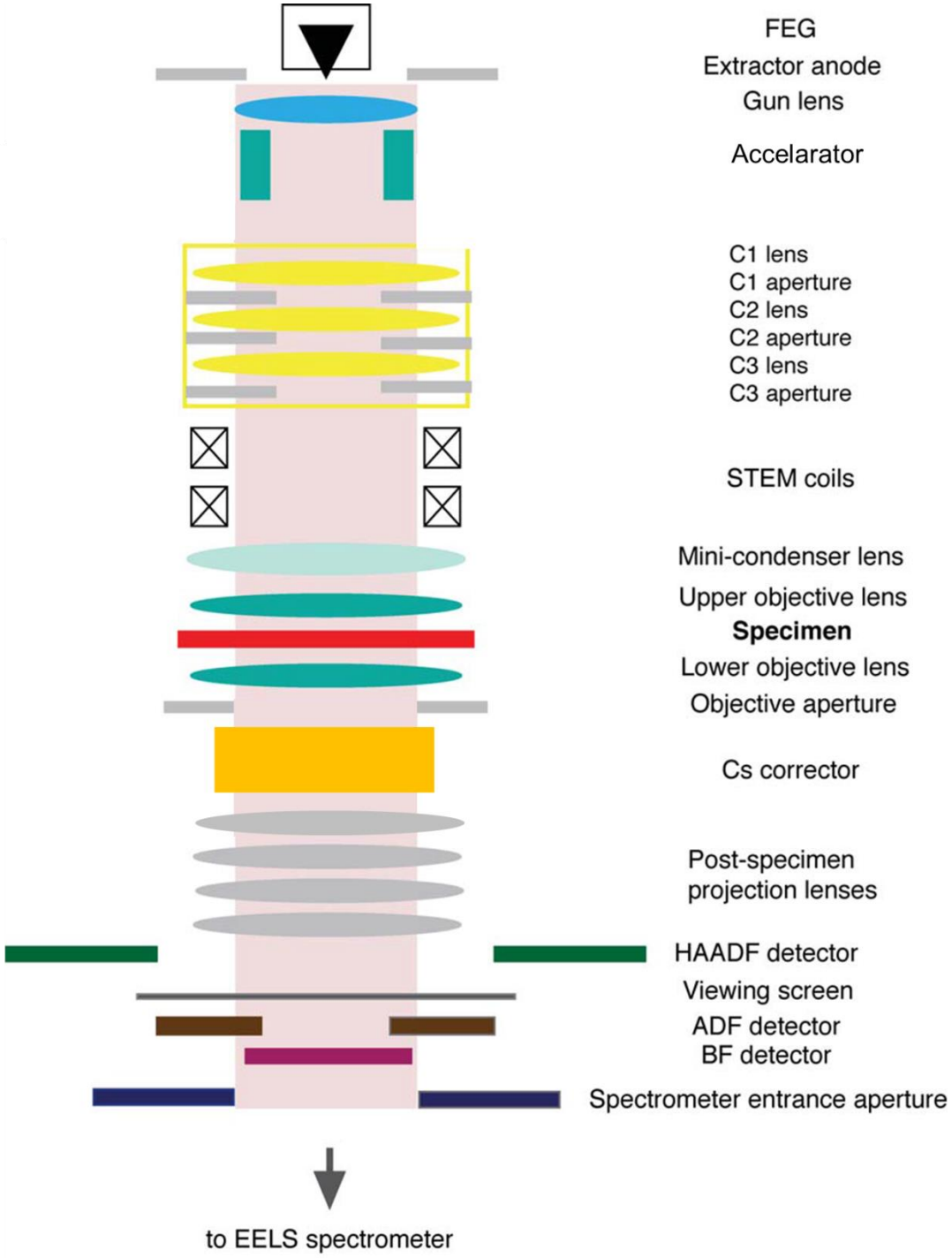

Figure 2.3: Schematic diagram of a TEM. [86]

After the beam interacts with the sample, an intermediate image is formed in the image plane and a diffraction pattern is formed at the back focal plane of the objective lens. The intermediate image or

diffraction pattern is further magnified by the diffraction and the projection lenses to form the final magnified image on the phosphors screen/camera attached at the bottom of the column. The microscope is further fitted with an image aberration corrector to compensate for spherical aberration and other higher order aberrations of the objective lens. Different cameras and detectors are attached after the projection system for image acquisition. This complex lens system in the TEM provides the flexibility in operating the microscope in different modes such as bright-field TEM, dark-field TEM and selected area electron diffraction (SAED).

The basic optics of a TEM is similar to a conventional optical microscope and it is easy to understand the image resolution of a TEM in terms of the classical Rayleigh criterion, which describes the smallest objects that can be resolved.

$$\delta = \frac{0.61\,\lambda}{\mu\, sin\beta} \qquad (2.1)$$

This equation provides the theoretical resolution limit of a microscope, where λ is the wavelength of the radiation, μ is the refractive index and β is the collection semi angle of the magnifying lens. The term μ sinβ is called the numerical aperture. From the equation, it can be seen that the resolution is limited by the wavelength and the numerical aperture. This leads to a resolution of ~200-300 nm in classical light optical microscopes. Based on the equation by Louis de Broglie, accelerated electrons have a much smaller wavelength compared to light, thus providing the possibility to increase the resolution in microscopy. The wavelength λ of an electron, accelerated by a potential V is given by the relativistic relation,

$$\lambda = \frac{h}{\sqrt{2m_0 eV\left(1+\frac{eV}{2m_0 c^2}\right)}} \qquad (2.2)$$

where m_0 is the rest mass of the electron and c is the speed of light.

The wavelength of electrons varies between $4.18\text{x}10^{-2}$ Å and $1.97\text{x}10^{-2}$ Å for the typical acceleration voltages between 80 kV and 300 kV used in TEM these days and thus sub-Ångstrom resolution is in principle accessible. However, in practice, the resolution is reduced by the small numerical aperture, which has to be used to prevent significant lens aberrations, and the temporal and special coherence of the beam and stability of the microscope, which are explained in detail in section 2.5.

2.4. Operating modes in TEM

2.4.1. Bright-field / dark-field imaging

The basic operating mode in TEM is bright-field TEM imaging (Figure 2.4). The beam interacting with the sample is scattered depending on the material, thickness and crystallinity/orientation. Parts of the scattered/diffracted electrons are blocked by the objective aperture in the back focal plane and the objective lens forms a magnified image with the remaining electrons in the intermediate image plane, which is further magnified by the projection system. Two different contrast mechanisms contribute to the image contrast in BF-TEM: mass-thickness contrast and diffraction contrast. Mass-thickness contrast is due to electrons scattered to high angles by the interaction with the nucleus. The scattering depends on the average atomic number and the thickness and the contrast is therefore called mass-thickness contrast. Areas with higher mass-thickens will scatter stronger leading to more electrons being blocked by the aperture and thus these areas will appear dark in the bright field images. Diffraction contrast arises as result of the coherent scattering events where the high angle diffracted beams are blocked by the objective aperture. The areas that are diffracting strongly will therefore appear dark in the bright field image. However, as the diffraction angle varies depending up on the orientation of the sample, there can be some small angle diffracted beams contributing to the image formation in BF-TEM. It is difficult to completely separate these contrast mechanisms and the contrast we see in normal BF-TEM images as these arises from the combination of both mass-thickens and diffraction contrast in crystalline samples.

Alternatively, the TEM can also be operated in dark field mode for imaging. In this case, the direct beam is blocked and diffracted beams are selected for the image formation. This is accomplished by tilting the beam to select a diffracted beam in the objective aperture and blocking the direct and other diffracted beams (Figure 2.4). In dark field mode, the image will be bright for the areas that diffract strongly in the selected angular range. Depending on the size of the aperture used, one or more diffracted beams can be selected.

2.4.2. Diffraction mode

Another operation mode in TEM is diffraction mode (Figure 2.4). A diffraction pattern is formed in the back focal plane of the objective lens where the direct and the diffracted beams intersect. By adjusting the strength of the intermediate lens, this pattern is imaged on the image plane of the first projection lens and thus

magnified further by the projection system onto the screen/camera. A selected area aperture can be inserted in the intermediate image plane of the objective lens to define the area from which the diffraction pattern is recorded. This is called selected area electron diffraction (SAED).

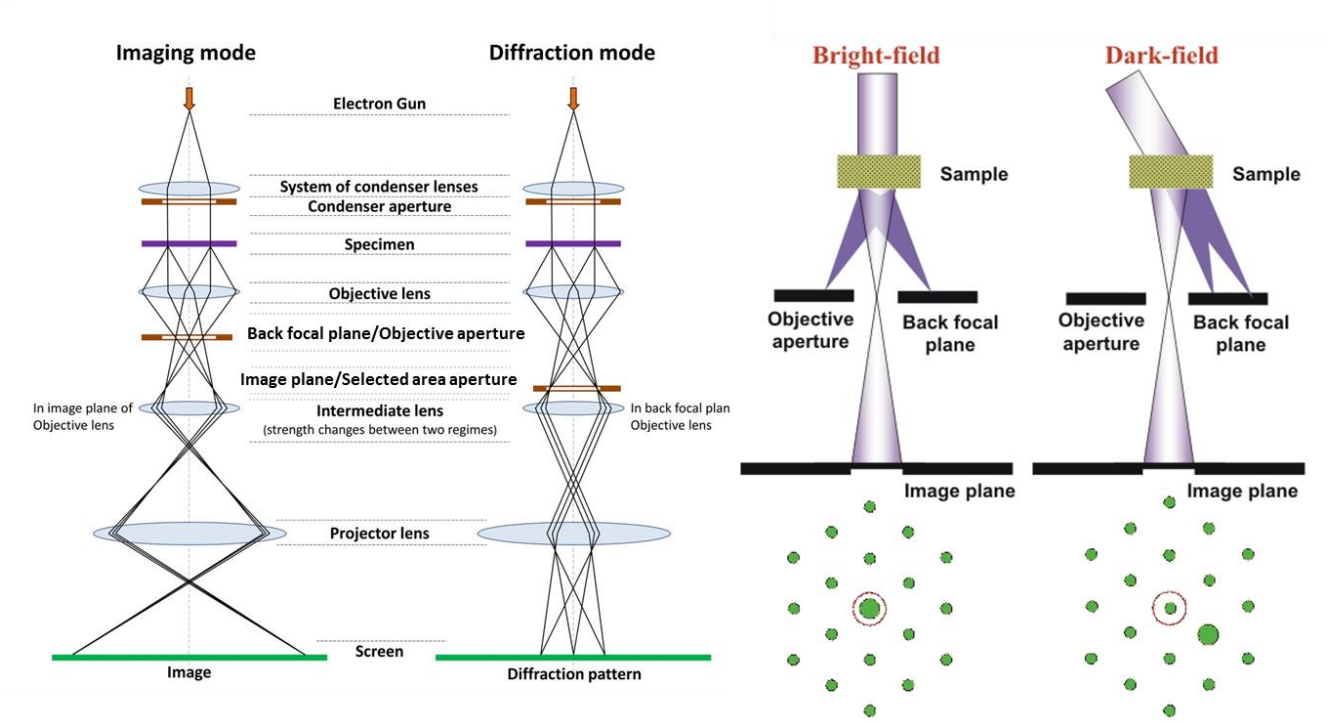

Figure 2.4: Different operation modes in TEM. [87,88]

The diffraction pattern contains crystallographic information about the structure, orientation and crystallite size of the material observed. Diffraction patterns are formed when the beam of electron is reflected by lattice planes, which satisfy the Bragg condition. According to Bragg's law, the condition for maximum intensity for interference is fulfilled when the path length difference travelled by the wave between parallel lattice planes is an integer number of the wavelength. This is fulfilled when

$$N \lambda = 2d \sin \theta \qquad (2.3)$$

where λ is the wave length of the incident beam, d is the lattice spacing between the planes and θ is the incidence angle. This shows that the diffraction patterns can be used to understand the crystal structure and orientation.

When the number of coherently scattering domains satisfying the Bragg condition in the area of interest in the TEM increases, the diffraction pattern transforms from a single crystalline pattern to a discrete ring (powder) pattern. The width of the ring is inversely related to the crystallite size. For nanocrystalline materials, the Scherrer equation [89] provides a good approximation to estimate the coherently scattering domain size D and thus the crystallite size from the width of the diffraction rings:

$$D = \frac{K\,\lambda}{\beta\,cos\theta} \qquad (2.4)$$

where K is called the shape factor, which is 1 for a perfectly isotropic particles and for all other shapes it will be less than 1. The Scherer equation can be usually used to calculate the crystallite size if instrumental peak broadening effects are compensated.

2.5. Phase contrast and high resolution imaging

High-resolution imaging allows direct imaging of the atomic structure of a sample. The contrast in HRTEM arises from the interference of the direct electron beam and diffracted electrons in the image plane. Interaction of a coherent plane wave electron beam with the specimen results in a modulation of its phase and amplitude. This modulation is a result of the interaction of the incoming plane with the potential of the specimen. For very thin specimens, we can assume that no electrons are absorbed, thus the amplitude is constant and only the phase is modulated by the potential of the specimen. In this phase object approximation, the electron wave function at the exit plane of the specimen can be described as

$$\Psi_e(r) = \exp[i\,\sigma\,V_p(r)\,t] \qquad (2.5)$$

Where V_p is the projected crystal potential, σ the interaction parameter, and t the thickness of the sample. For a very thin sample, acting as a weak scatterer, the phase modulation in the exit wave is small and can be approximated only taking into account the first order Taylor coefficient of the exponential function. In this weak-phase object approximation, the imaginary part of the exit wave is proportional to the projected potential:

$$\Psi_e(r) = 1 + i\,\sigma\,V_p(r)\,t \qquad (2.6)$$

This exit wave propagates through the lens system and the intensity I of the wave Ψ_i is recorded in the image. While moving through the lens, the wave is affected by lens aberrations, which can be expressed as a convolution of the exit wave with the transfer function describing the lens aberrations. These aberrations can be described by the transfer function T of the microscope. The image plane wave function Ψ_i can be obtained by convolving the exit wave function with the transfer function, which can be expressed as direct product of the exit wave function with the transfer function in reciprocal space.

$$\Psi_i(\vec{r}) = \Psi_e(\vec{r}) \otimes T(\vec{r}) \tag{2.7}$$

$$\Psi_i(\vec{g}) = \Psi_e(\vec{g}) * T(\vec{g}) \tag{2.8}$$

and the intensity I can be written as

$$I(\vec{g}) = |\Psi_i(\vec{g})|^2 = [\Psi_i(\vec{g}) * T(\vec{g})] * [\Psi_i(\vec{g}) * T(\vec{g})]^* \tag{2.9}$$

Using the weak phase object approximation, the intensity can be expressed as

$$I(\vec{g}) \approx 1 + 2Re\{ i\sigma V_p(\vec{g})t * T(\vec{g}) \} + \left| i\sigma V_p(\vec{g})t * T(\vec{g}) \right|^2 \tag{2.10}$$

When the object is assumed to be a weak scatterer the quadratic term in equation 2.10 will be small and can be neglected. So according to linear imaging theory

$$I_L(\vec{g}) \approx 1 + 2Re\{i\sigma V_p(\vec{g})t * T(\vec{g})\} \tag{2.11}$$

The transfer function T can be expressed as

$$T(\vec{g}) = A(\vec{g}) (\exp[-i\chi(\vec{g})] \tag{2.12}$$

where A is the aperture function (1 within the objective aperture, 0 outside) and χ the aberration function.

Thus the observed intensity I_L can be expressed as

$$I_L(\vec{g} \neq 0) \approx 2\sigma V_p(\vec{g})t \sin[\chi(\vec{g})] \tag{2.13}$$

This equation means that the lens aberrations introduce a phase shift sin [$\chi(\vec{g})$], which is modulating the intensity of the diffracted beams.

Only considering the aberrations due to spherical aberration C_s and defocus z, the aberration function χ can be expressed as

$$\chi\,(g) = 2\pi[\frac{C_s\lambda^3 g^4}{4} + \frac{z\lambda g^2}{2}] \qquad (2.14)$$

Combining equation 2.13 and 2.14, the relation between the image intensity and the exit wave depends on the aberrations of the microscope and can be described by the contrast transfer function (Figure 2.5) as phase factor, which depends on the spatial frequency (diffraction angle).

$$\text{CTF}\,(g) = \sin(\chi\,(g)) = \sin[2\pi\,[\frac{C_s\lambda^3 g^4}{4} + \frac{z\lambda g^2}{2}]] \qquad (2.15)$$

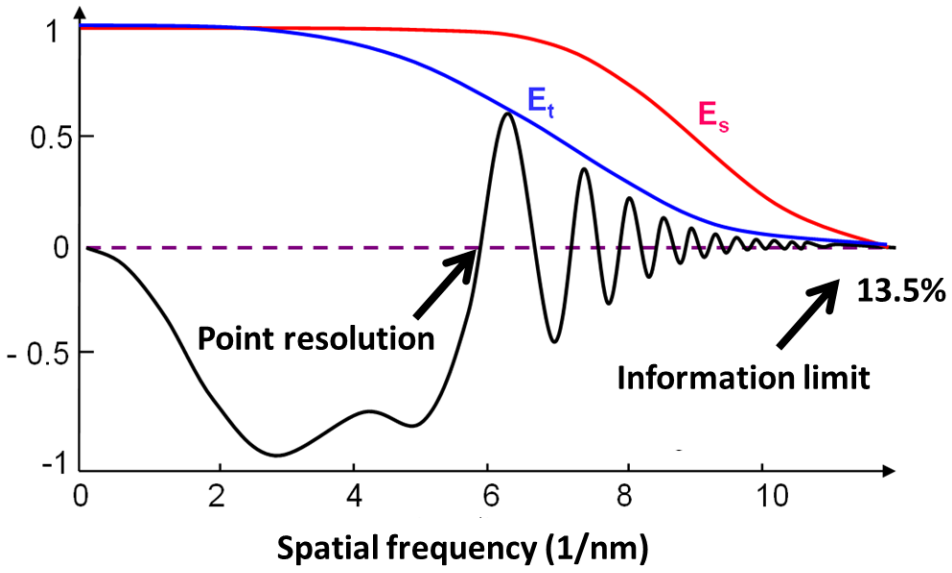

Figure 2.5: CTF of a microscope at Scherzer defocus with coherence envelop functions. [90]

The oscillation in the CTF results in difficulties in interpreting HRTEM images. At different defocus values, a set of lattice planes (and thus an atomic position) might appear dark (CTF = -1), bright (CTF = +1) or can be invisible when the CTF = 0. This means that the high intensity regions in a HRTEM image do not

necessarily represent the location of an atom, but the interpretation of the image intensities is affected by the defocus and other lens aberrations. Ideally, the CTF should be completely flat for a direct interpretation of the image intensities. A good approximation is reached at Scherzer focus, where the CTF exhibits a large plateau and is of the same sign up to the so called point resolution d_p of the microscope. Image intensities until this special frequency can be interpreted with less ambiguity with proper understanding of the exit wave. Only considering the spherical aberration of the microscope, the point resolution can be expressed as

$$d_p = \frac{1}{\sqrt{2C}} C_s^{\frac{1}{4}} \lambda^{\frac{3}{4}} \tag{2.16}$$

Nevertheless, additional information is present in HRTEM images even beyond the point resolution. This information limit determines up to which spatial frequency information is encoded in the microscope images and thus defines the resolving limit of the TEM. The information limit is defined by the temporal (E_t) and spatial (Es) coherence envelop functions of the microscope. The temporal coherence depends on the energy spread of the electron beam due to the instabilities in accelerating voltage and the electron gun emission. When the electron beam is not perfectly monochromatic, the chromatic aberration of the lenses result in a focus spread of the electron wave. This is enhanced further by any variations in the lens currents. This averaging of different focus conditions can be expressed as a damping function (E_t) superimposed on the contrast transfer function. The spatial (E_s) coherence envelop function is caused by the finite source leading to a finite convergence angle of the beam. The illumination of an object under different angles results in a distortion and shift of the object in the image plane depending on the spherical aberration of the lens. These two envelop functions dampen out the CTF at higher spatial frequencies and limit the maximum information that can be transferred in the microscope. Conventionally, the information limit is defined as the spatial frequency where the contrast falls (the temporal coherence function) to 13.5 %.

2.5.1. Higher order aberrations

From the previous discussion we can clearly see the effect of defocus and spherical aberration for the uniform information transfer and thus interpretable information in TEM. Apart from these aberrations, it is also important to understand the other lower and higher order aberrations. The two most common aberrations in TEM are astigmatism and coma. Two fold Astigmatism occurs when the focus of the lens is different in two perpendicular directions. Higher order astigmatism produces directional dependent defocus

along more than one axis. This arises due to the imperfect magnetic fields acting on the electrons. The main reason for the inhomogeneity in magnetic fields is the imperfection in the symmetry of the pole piece. Two fold astigmatism can be easy corrected using stigmator coils which induce counter fields to reduce the inhomogeneity. Coma occurs when the electron beam is tilted away from the optic axis of the electron beam. This results in a different phase shift for +g and –g beams creating an asymmetry in the image. Conventionally coma can be compensated by tilting the beam to find the coma free axis of the objective lens.

These lower order terms are sufficient in conventional microscopes considering the low spatial frequencies involved. But in modern microscopes, to reach sub Ångstrom resolution, high spatial frequencies have to be transferred in the image. At these high spatial frequencies, not only the lower order aberrations are significant, but higher order aberrations also become more important. The higher order aberrations with higher folndness of rotational symmetries thus gain importance with an increasing information limit of the microscope. This extended aberration function is expressed in terms of wave aberration function which denote the phase shift of the wave front during its transfer by the TEM optical system. Considering the higher order aberrations and expanding the aberration wave function χ (g) to fifth order gives

$$\chi(\omega) = \frac{1}{\lambda}\,\mathrm{Re}\{\frac{1}{2}C_{10}\,\omega\bar{\omega}+\frac{1}{2}C_{12}\,\bar{\omega}^2+\frac{1}{2}C_{21}\,\omega\bar{\omega}^2+\frac{1}{3}C_{23}\,\bar{\omega}^3+\frac{1}{4}C_{30}\,\omega^2\bar{\omega}^2+\frac{1}{4}C_{32}\,\omega\bar{\omega}^3+\frac{1}{4}C_{34}\,\bar{\omega}^4+\frac{1}{5}C_{41}\,\omega^2\bar{\omega}^3$$

$$+\frac{1}{5}C_{43}\,\omega\bar{\omega}^4+\frac{1}{5}C_{45}\,\bar{\omega}^5+\frac{1}{6}C_{50}\omega^3\,\bar{\omega}^3+\frac{1}{6}C_{52}\omega^2\,\bar{\omega}^4+\frac{1}{6}C_{55}\omega\bar{\omega}^5+\frac{1}{6}C_{56}\bar{\omega}^6\}, \qquad (2.17)$$

Where $\omega = \lambda g$ is the complex scattering angle, λ is the wavelength used. According to this nomenclature, the aberration coefficients are C_{10} defocus, C_{12} twofold astigmatism, C_{21} second-order coma, C_{23} threefold astigmatism C_{30} third-order spherical aberration, C_{32} third-order star aberration, C_{34} fourfold astigmatism, C_{41} fourth-order coma, C_{43} three-lobe aberration, C_{45} fivefold astigmatism, C_{50} fifth-order spherical aberration, C_{52} fifth-order star aberration, C_{54} rosette aberration, and C_{56} sixfold astigmatism. Figure 2.6 shows the effect of mentioned aberration until the 6^{th} order. All these aberration induces an additional phase shift and a tolerance limit of 90° is proposed for each aberration with in the information limit. The effect of these individual aberrations can be understood by expressing as phase plates up to the 6^{th} order in g.

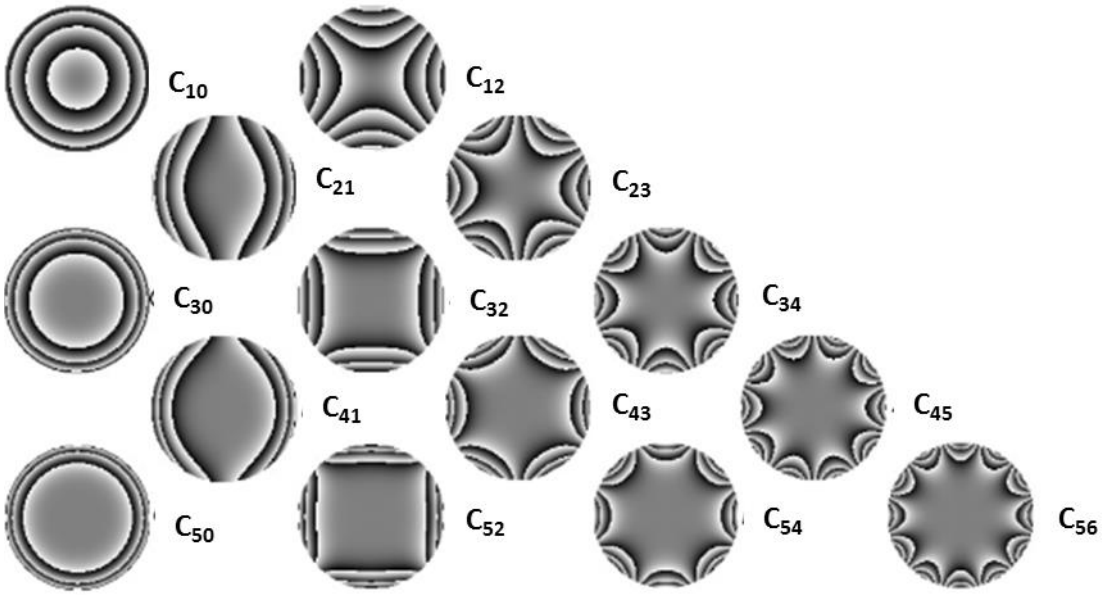

Figure 2.6: Phase plates of individual aberrations arranged with rotational symmetries. [91]

In conventional microscopes, only two fold astigmatism and coma can be compensated. Modern microscopes are equipped with aberration correctors, which correct for the spherical aberration and other higher order aberrations. [92] The spherical aberration correction is carried out using special correctors consisting of non-round lenses. In the case of the Titan 80-300 used in this work, the core consists of two hexapoles. Unlike in round electron lenses, these can induce a negative spherical aberration. By changing the strength of the corrector, it is possible to compensate the positive spherical aberration of the objective lens. Higher order wave aberration can be determined using beam tilt diffractogram series, which in turn can be used to tune the corrector to compensate these aberrations. [93,94] This can extend the point resolution of the microscope beyond the information limit (Figure 2.7a). [93] Figure 2.7b,c shows the effect of aberration correction comparing the diffractograms of the corrected and uncorrected system. The distortion in the diffractograms at higher tilt angles shows the effect of spherical aberration and other higher order aberrations on the phase shift. In the corrected system, the diffractograms show identical shapes even at high tilt angles.

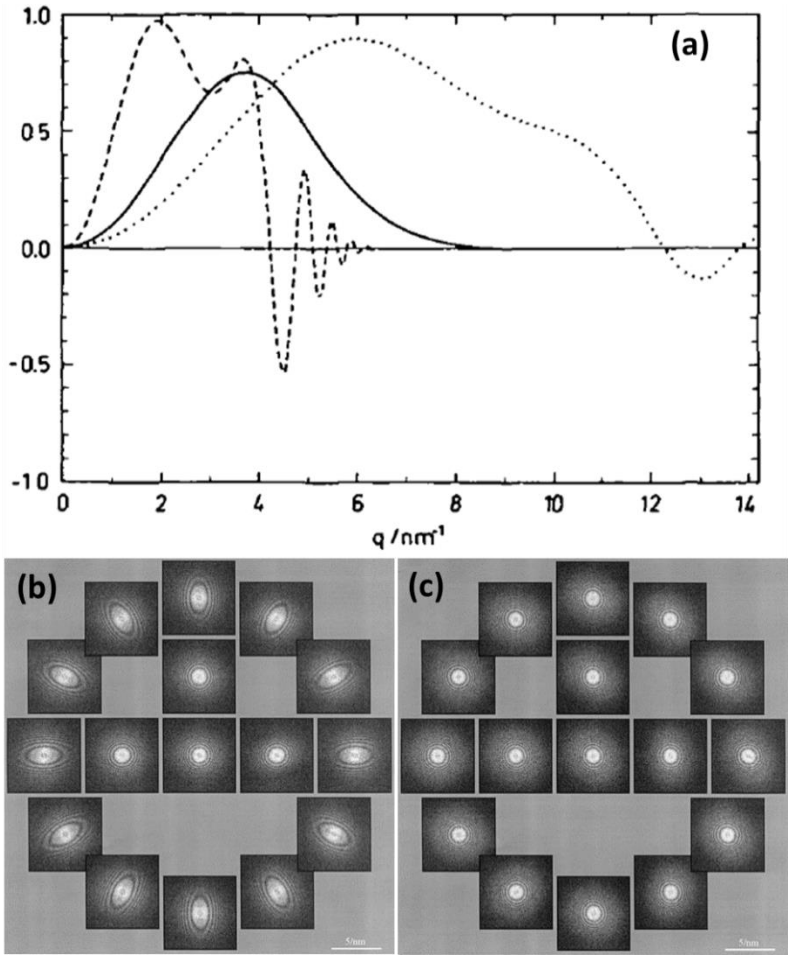

Figure 2.7: (a) CTF of an uncorrected system (dashed line) and uncorrected system (solid line) at Scherzer defocus. The dotted line represents the improvement in information limit by reducing the energy spread form 0.7 ev to 0.2 ev using a monochromator (b) Diffractograms obtained from non-corrected system and (c) corrected system. [93,94]

2.6. Spectroscopy in TEM

2.6.1. Energy dispersive X-ray analysis

As mentioned earlier, the X-rays emitted as a result of the beam specimen interaction can be used as a tool to understand the chemical composition of the sample. When the energy from an incoming beam is high enough to knock out an inner shell electron, the vacancy is filled by an outer shell electron. This process results in the emission of X-rays corresponding to the energy difference between the shells. The energy of

the emitted X-ray can be detected and analyzed by electron dispersive X-ray (EDX) spectroscopy. Every element has characteristic X-ray energy distribution corresponding to the possible transitions (Figure 2.8, note that not all these transition are detected by EDX). The allowed transitions can be used to identify the elements. The peaks are characterized by the shells between which the transition is occurring. These characteristic X- ray peaks provide both qualitative and quantitative information on the presence of different elements in the material.

The X-rays produced by the electron beam are measured using a semiconductor detector. The most commonly used detector is a lithium drifted silicon (SiLi) detector and more recently silicon drift detectors have been implemented. An X-ray reaching the detector creates electron hole pairs corresponding to the energy of the incident X-rays. By applying a bias to the detector, the electron hole pairs are separated and will move to the collection electrode. Here they produce a current corresponding to the number of electron hole pairs produced. By measuring the amount of current produced by each X-ray, the original energy of the X-ray can be measured and the elements identified. The detector crystal is isolated from the high vacuum using a window. Previously beryllium windows were used which absorbs low energy X-rays (< ~ 1 keV) and detection of elements below Na (Z = 11) was difficult. Modern microscopes uses ultra-thin windows made of polymer films, boron nitride or silicon nitride which allows the passage of low keV X-rays down to ~0.1 keV. Si(Li) detectors are cooled down to liquid nitrogen temperatures to reduce the noise as the thermal energy can produce electron hole pairs.

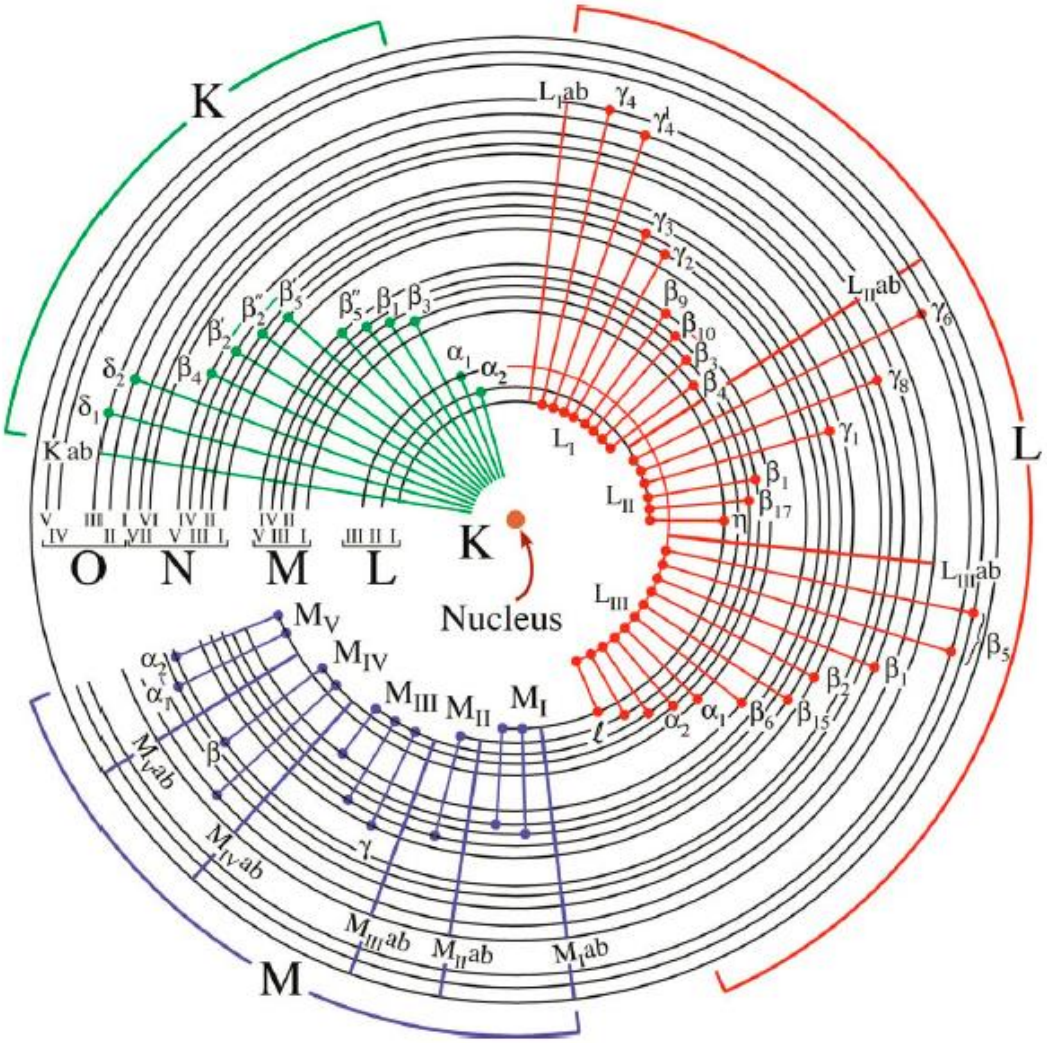

Figure 2.8: Possible electron transitions that give rise to K,L and M series of characteristic X-rays. Not all of these are detected by X-ray analysis. [95]

A quantitative compositional analysis requires knowledge of the X-ray emission efficiency of each element. However, the quantification is not straightforward and different factors have to be taken into account. Reabsorption of X-rays within the specimen and at the detector entrance is particularly important for light elements, which produce low-energy signals owing to the low ionization potential and low-energy X-rays are strongly reabsorbed by matter. Higher energy X-rays can excite a lower energy emission leading to X-ray fluorescence, which becomes important when two elements have similar emission energies. Also proper

subtraction of the Bremsstrahlung background is necessary, which is difficult for losses less than 1 keV. These factors make the detection and quantification of low atomic number elements difficult.

2.6.2. Electron energy loss spectroscopy

Electron energy loss spectroscopy analyzes the energy distribution of the electrons after the interaction with a specimen. The inelastic interaction provides information on the composition, electronic structure, valance state and band gap etc. down to atomic resolution. The major advantage of EELS is that unlike EDS, it can detect and quantify all elements in the periodic table and is particularly sensitive to light elements. The main component in EELS instrumentation is a spectrometer mounted below the viewing screen/detectors in the TEM column (Figure 2.9). The electrons are selected by an entrance aperture and travel down the drift tube through the spectrometer. The spectrometer consists of a magnetic prism, which can bend electrons through the Lorentz force depending on the energy of the electrons. The electrons that have experienced higher losses by the interaction with the sample are deflected more than the ones without energy loss.

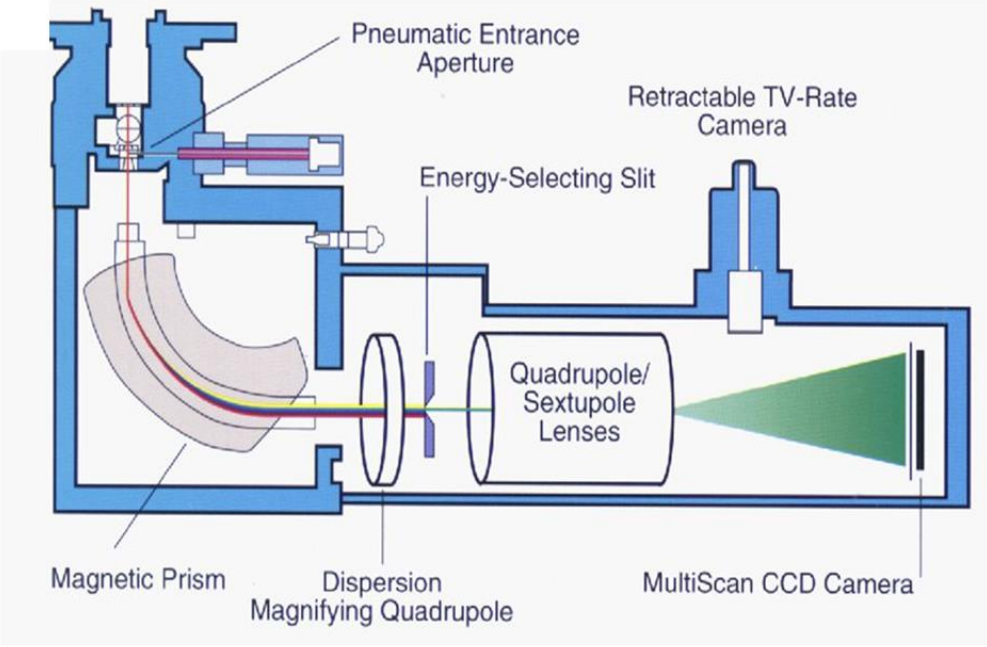

Figure 2.9: Schematic of Gatan Imaging Filter. [95]

In the Gatan Imaging filter (GIF), the spectrometer is also equipped with energy filtering slit, after the magnetic prism, to select electrons with a specific energy. The energy selected electrons pass through an optical system, consisting of a complex lens system, to create an energy filtered image. This technique is called energy filtered TEM (EFTEM) and provides energy specific images. Even further, a series of images can be acquired of the same region with varying selected energy. These images can be combined to form an EELS data cube in which each pixel carries the spatial information in 2 dimensions and the 3rd dimension provides the information of the energy. Using this, it is possible to produce chemical maps of the elements present.

A typical EELS spectrum consists of two main regions, the low loss region and the core loss region. The low loss region consists of both elastically scattered electrons (zero loss) and inelastically scattered electrons with low energy loss (Figure 2.10a). The region close to the zero loss peak is dominated by collective excitation of valance electrons (plasmon excitations) and inter-band transitions. They give information about the dielectric properties of material, i.e. band structure and plasmons. Since this low loss region contains both the elastically and most of the inelastically scattered electrons, this can also provide information about the sample thickness by subtracting the inelastic interaction from the elastic interactions. [96] At higher energies, the spectrum shows characteristic core loss edges which can be used to identify different elements and their bonding/coordination (Figure 2.10b). These edges are called ionization edges and formed when the incident beam transfers sufficient energy to a core shell electron to excite it to the fermi level or an antibonding state. The possible transitions are similar as shown before (Figure 2.8). This ionization loss is characteristic for the atom involved and gives direct chemical information about the atom. The core loss edges contain further information, because the bonding effects and the density of states in the sample. This result in complex near edge oscillations called energy loss near edge spectra (ELNES), which usually extend up to 50 eV from the core loss edge. There can also be energy losses due to the diffraction effects from the atoms surrounding the atom and can extend above 50 eV and are called as extended energy loss fine structure (EXEFLS).

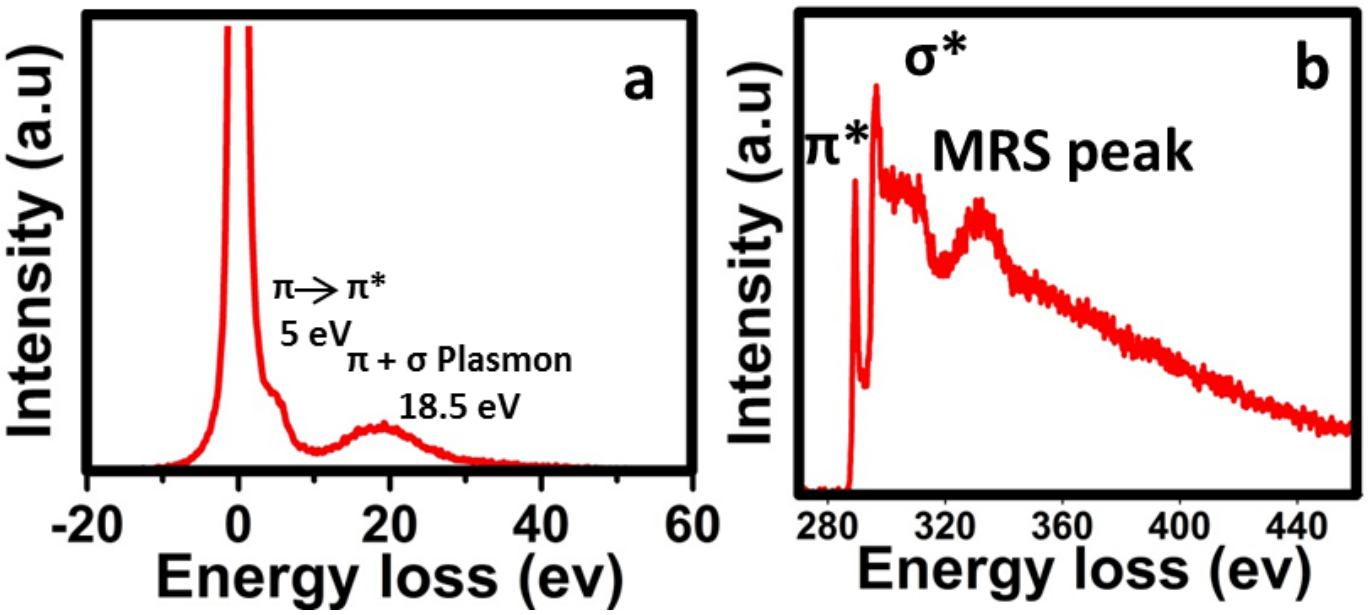

Figure 2.10: EELs low loss region (a) and core loss region (b) of carbon.

Figure 2.10 shows a typical low loss and core loss edge of a graphitic material. In the low loss region, the peak in the range of 4-7 eV, results from the interband π to π^* transitions and a second peak in the range of 15-26 eV is due to the collective oscillation of bulk valance plasmons. The core loss edge contains two prominent peaks which starts at 285 eV by the transition from 1s to π^* and the excitations corresponding to excitations to the σ^* state. We can also see a peak called multiple scattering resonance (MSR) peak, which corresponds to the scattering from the nearest neighboring atoms. An increase in the intensity of the MSR peak corresponds to an increasing order of the nearest and next nearest bonds. In the core loss edge, the first peak is characteristic for sp^2 bonding.

The experimental conditions for acquiring EELS spectra are also important for a precise quantification. The most important acquisition parameters are the convergence angle α of the incident beam and the collection angle β, which is determined by the width of the GIF entrance aperture. This is particularly important for quantifying EELS of graphitic materials, where anisotropy exists for the π and σ bonds in the lateral and perpendicular direction. This anisotropy effects can be cancelled by selecting a suitable combination of α and β, where the intensity of the π^* and σ^* peak is independent of the bond orientation. This combination is called magic angle and can be experimentally determined for different accelerating voltages. [97,98]

With the magic angle acquisition, integrated intensity ratios of the π peak over the π+σ peak can be used to quantify the sp^2 percentage in disordered carbon by comparing it with a completely graphitized sample. [59,99] The integrated intensity of the π^* peak is calculated using a 5 eV window starting from 282.5 eV and the π+σ intensity is calculated using a 20 eV window from the same starting point.

2.7. Electron beam induced transformations

During the interaction of an electron beam with the specimen, the beam can induce transformation to the sample, which is usually termed as beam damage. [100] The main damages caused are electrostatics charging, radiolysis (ionization damage), displacement damage and sputtering (Figure 2.11). Electrically insulating samples will suffer electrostatic charging due to the charge transfer from the incoming beam or secondary electron generation. If the energy transfer to an atom is more than the displacement energy, this can lead to a displacement of an atom to an interstitial site thereby degrading the crystallinity of the specimen. If the energy transferred is even higher, this leads to the removal of an atom to the free space (sputtering).

The beam can induce ionization damage in which the inelastic scattering leads to degradation of the structure. Unlike the knock on damage, this occurs by creating an excited state due to electronic transitions. While gaining sufficient energy from the incoming beam, one electron is excited above the fermi level in to the conduction band or an anti-bonding state. If the de- excitation process, the filling of the hole, is not rapid enough, some of the excitation energies stored will lead to the change in inter atomic bonding and breaking of bonds, thus degrading the structure. The mechanisms responsible for beam damage can be different for different materials and in a broader sense, the beam damage depends on the delocalization of the excited state and the possible pathways for that.

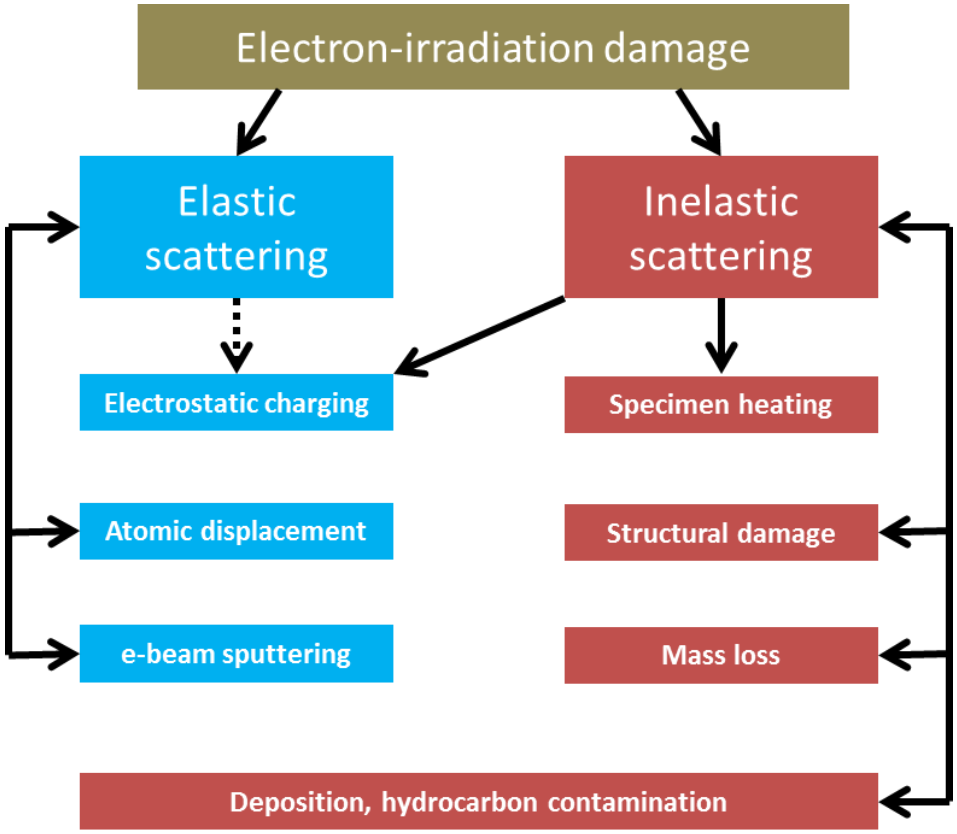

Figure 2.11: Beam damage due to high energy electron beam. [100].

There are also secondary effects due to the electron beam. Frequently observed beam induced effect is the carbon deposition on the sample, which occurs due to the cracking of hydrocarbon impurities in the TEM column. These impurities can attach and carbonize on the sample under the electron beam making it difficult to do imaging and analysis on the sample. Furthermore, the electron beam can activate oxygen, hydrogen and other metallic impurities, which may react with the sample forming undesirable products.

Considering carbon materials, the main damage mechanisms identified are sputtering and radiolysis. [101,102] Beam induced transformation of graphite and other carbon nanostructures like fullerene, carbon nano tubes and graphene is a well-studied field. Studies of graphitic layers show that the displacement threshold is highly anisotropic in nature. It is easier to displace atoms normal to the plane than in any direction parallel to the plane. The displacement threshold for graphitic layers reported earlier is about 100 kV. [103] The displacement threshold for fullerene is reported to be below 80 kV [104] and for singled wall carbon nanotubes, a value of 86 kV [105] is reported.

The studies on electron beam transformation became more prominent after the successful exfoliation of graphene. There has been a lot of work focusing on beam damage in single and few layer of graphene. The studies show that the interaction with electron beam can introduce structural changes and bond rotation in the graphene lattice. [16] One of the important works in this area is carried out by Jannik Mayer *et al.*, where they studied the threshold for beam induced sputtering on single layer graphene. [102] The beam induced sputtering threshold is found to be just above 80 kV in the case of defect free graphene and it is considered safe to image graphene with beam energies of 80 kV and below. However, the threshold decreases to around 50 kV for defective graphene and edges. [106]

There are also studies which show low voltage beam damage in graphene [107–109] and CNTs [110,111] which results in a degradation of the electrical and optical properties. At these low voltages, which is well below the threshold for knock on damage, radiolysis will be the main damage mechanism. In these low voltage studies on graphene, continuous exposure with 5 to 20 kV electrons led to the introduction of disorder in the crystalline material. This has been characterized by the emergence of the D peak in Raman spectroscopy after exposure to the electron beam. [108] Continuous exposure resulted in a transformation of graphene to ncg and finally to an amorphous phase. It is clear that the beam damage caused by this low energy beam is not because of the sputtering of atoms. The possible mechanisms discussed are the C-C bond breakage and a subsequent excitation of the atoms due to the energy transfer from the beam. Also large inelastic scattering strength can effectively excite an atom to higher energy antibonding states, which will lower the activation energy for bond rearrangement or breakage. Collective oscillations of plasmon and valance electrons are also possible with this low energy electron beam. Even though the mechanism of damage due to sputtering is well studied, the low energy beam induced damage in these carbon nanostructures are yet to be completely understood. [109]

Apart from this direct damage, a high-energy electron beam is known to induce different structural changes in graphene and carbon nano-structures on top of a graphene substrate even at 80 kV. There are a number of studies on purely beam-induced transformations of carbon nano-structures on top of graphitic substrates at 80 kV. The direct transformation of graphene to fullerenes [112,79] and graphene nano ribbons to carbon nano tubes [113] were observed with an electron beam even at 80 kV. Carbon nano structures are seen to be highly active on top of the graphitic substrate under the electron beam. Furthermore, the electron beam can also act as a source to add new atoms. A high amount of ad-atoms have been observed previously during

in situ heating of graphene in the TEM. [114] These ad-atoms are highly mobile on top of the graphitic substrate and can attach and heal vacancies and nano pores at high temperatures. [114] The source of these ad-atoms can be sputtering of carbon atoms by the electron beam or residual hydrocarbon impurities in the TEM column. [64,114,78] The hydrocarbon impurities in the TEM column can be cracked and act as a carbon source, graphitizing on the top of a graphitic substrate with and without the support of a catalyst. [64,78] Similarly, activation of oxygen, hydrogen and metallic impurities in the column by the electron beam results in catalytic type etching of graphene edges.

2.8. Electron beam lithography

The electron beam induced transformations are not always undesired. The interaction of an electron beam with samples can be used favorably in electron beam lithography. Electron beam lithography is a process, which uses a focused beam of electrons to precisely pattern a beam sensitive polymer film (Figure 2.12). The process is one of the most important techniques in nanofabrication. Electron beam lithography is similar to photolithography and is usually carried out using a scanning electron microscope. A focused beam of electrons is precisely scanned across a substrate, which is covered by an electron beam sensitive material. This results in a change of the solubility of the polymer in the exposed and unexposed areas. The difference in solubility is used to precisely pattern at the nano scale. The solubility upon exposure from the electron beam changes depending on the resist. The most widely used electron beam resist is PMMA, which is a positive resist. In positive photoresists, the exposed areas will have higher solubility and can be selectively removed by developing it using a suitable solvent. There are also negative beam resists, which decrease the solubility after the interaction with the electron beam. The resolution of electron beam lithography depends on the focused electron beam diameter, precise movement of the sample stage and the properties of the resist used. [115]

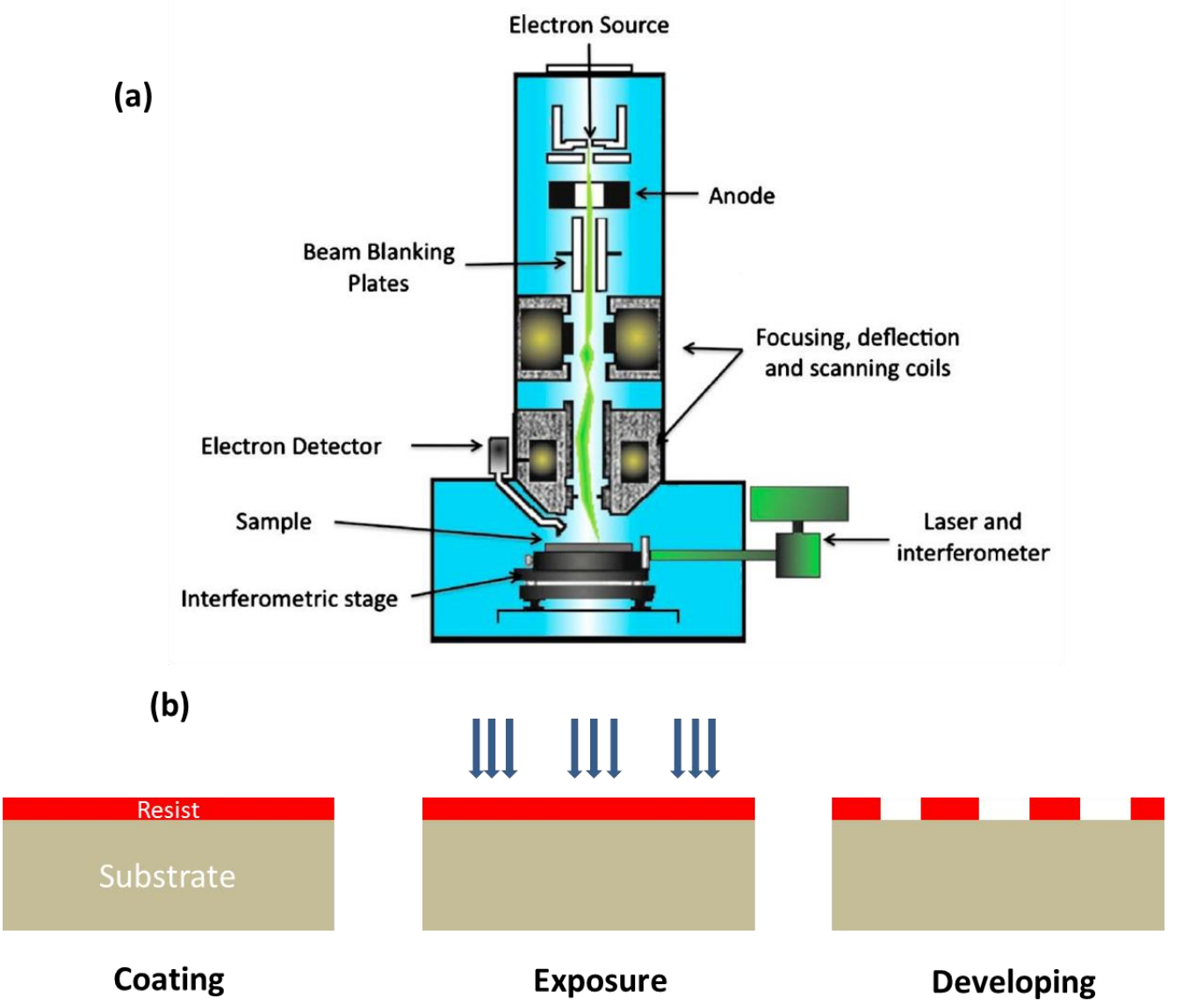

Figure 2.12: (a) Schematic diagram of an EBL system, (b) schematic digram of the electron beam lithography process. [115]

2.9. *In situ* TEM

Along with the improvements of the imaging and analytical capabilities, there has been a growing interest in the development of *in situ* capabilities for TEM. The main objective is to shift from postmortem characterization to live *in situ* measurements of structure, chemistry and properties of materials. This enables the detailed examination of transient stages of different dynamic processes at various length scales, which

are otherwise difficult to observe. A wide variety of holders have been developed for imaging and analytical measurements under applied heat, stress, electrical biasing, magnetic field, optical excitation and in liquid. This has been revolutionized with the introduction of MEMS based systems, which provide better control over the applied stimuli and have better stability for high-resolution imaging. A number of commercial systems are available for heating and electrical biasing of different materials.

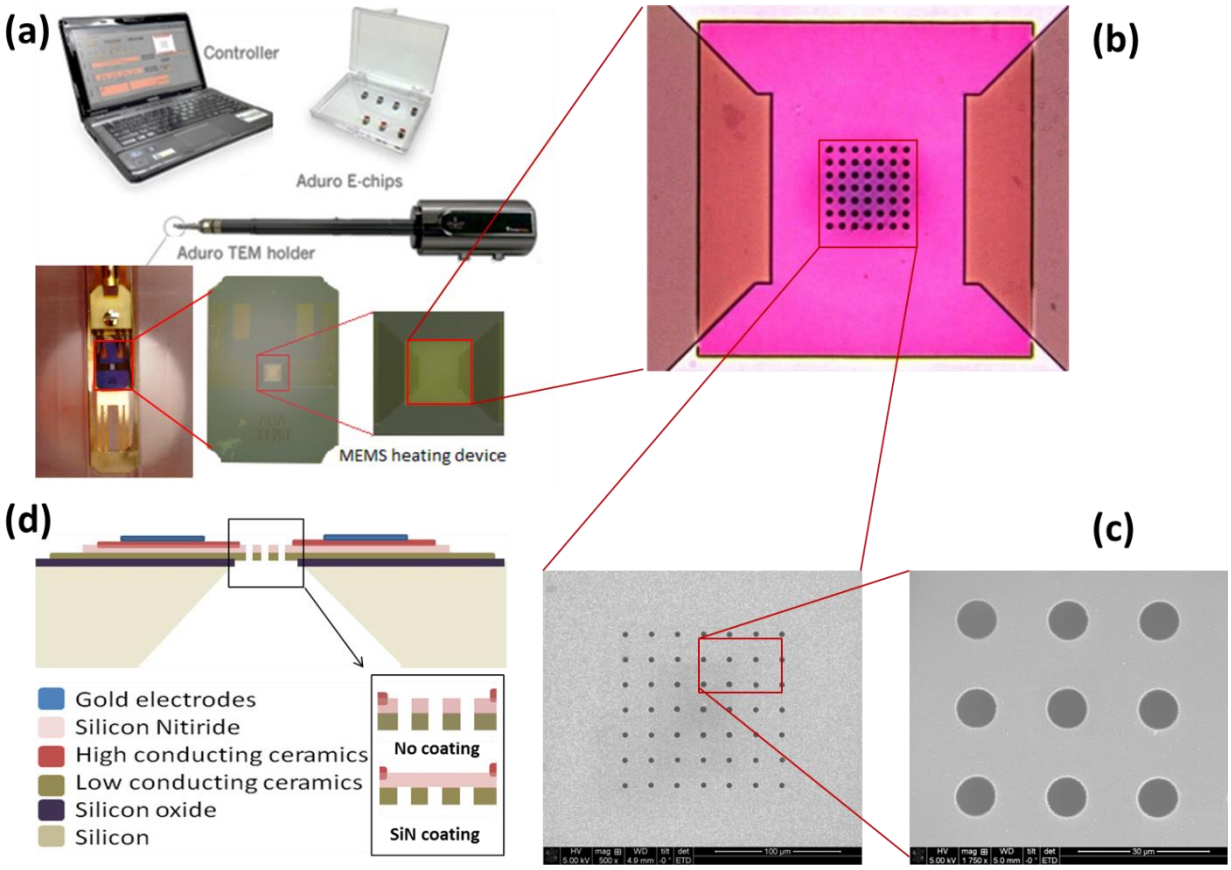

Figure 2.13: (a) Schematic diagram of Aduro system, (b,c) magnified images of the free-standing heating area and (d) detailed cross section view of the heating chip. [116].

An example for a MEMS based heating system, the commercially available Fusion system from Protochips, is shown (Figure 2.13). The system consists of a holder onto which MEMS based heating and electrical chip can be mounted. The holder consists of 4 electrical contacts, which can be connected to a potentiometer (Keithley) and controlled by software. The heating chips consist of a 500 micron square free-standing membrane which acts both as heating element and sample support. This free-standing region is resistively

heated using the contacts in the holder connected to a source meter. The chips are pre calibrated for temperature. Very thin small free-standing areas facilitate rapid heating and cooling rates.

The electrical biasing system uses the same holder, but different MEMS based chip. An electrical biasing chip consists of a free-standing 50 nm thick SiN window on to which electrodes are lithographically patterned. This free-standing membrane acts as electron transparent window with electrodes on to which the sample can be attached. In the Fusion system, 4 different electrodes are patterned facilitating 4 point electrical measurements. Combinations of heating and electrical biasing chips are also available in which two contacts will be used for heating and the other two will be used to electrically contact the sample. The maximum temperature that can reach with these MEMS based heating systems is 1200 to 1300 ºC depending on the manufacture. The heating electrical systems normally work below 1000 ºC due to the stability of the patterned electrode on top. The number of contact pads for electrical biasing also varies from 4 to 9 depending on the design and manufacture.

2.10. Raman spectroscopy

Raman spectroscopy is a vibrational spectroscopic technique, which provides information on the structure of a material. This is carried out by exciting with a monochromatic laser excitation. Raman spectroscopy is based on Raman effect which arises because of the interaction of incoming photon with the molecule. During the interaction, most of the light is elastically scattered by the molecule and the scattered light has the same wave length of the incident light. However a small fraction undergoes inelastic scattering where the scattered intensity is different from the incident intensity and this difference can be used for spectroscopy. The energy transfer from the incident radiation to the scattering molecule results in the excitation of the molecule to a virtual state and can result in two different processes. If the molecule is situated in the ground state it can be excited to a virtual state. This result in a lower energy (higher wave length) for the scattered radiation and the process is called stokes process. If the molecule is already in the excited state, it will be de excited to the ground state this results in higher energy (lower wave length) for the scattered beam and the process is called anti stoke process.

Raman spectrum of graphene consists of two prominent peaks named as G peak and 2D peak (Figure 2.14). [117] The position of G peak is at 1580 cm^{-1} and the position of 2D peak is at 2700 cm^{-1}. Apart from these two peaks, with increasing defects, another peak called D peak (defect peak) is observed at 1300 cm^{-1}. The

Raman signature of ncg shows a G peak, prominent D peak and broad 2D. The presence of D peak is the signature of nanocrystallinity in ncg and the ratio of intensity of the D peak over G peak can give a measure of nanocrystallinity, where a more pronounced D peak indicates smaller grain sizes. [118]

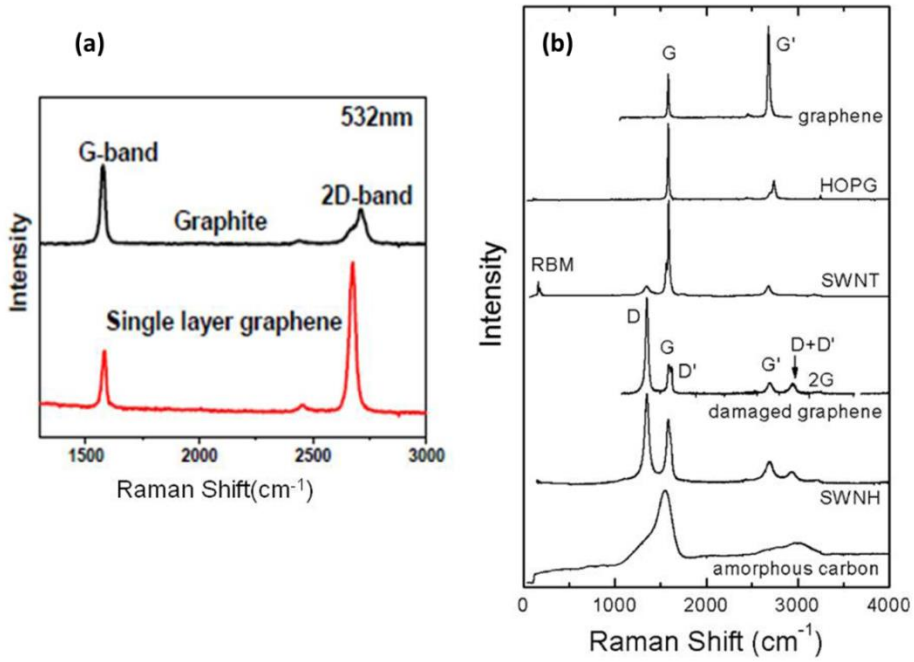

Figure 2.14: Raman spectrum of graphite and graphene at 532 laser excitations (a) and (b) Raman spectrum of different types of nano carbons. [117]

Even though Raman spectroscopy of graphite and nanocrystalline graphite [119] was studied long ago, this technique became increasingly popular with fabrication of ncg thin films. Raman signature especially the I_D /I_G ratio is a quick and easy was to get the quality of the graphitization and the crystallite size associated with it. Early efforts were made to quantify the defects and crystallite size with the help of Raman spectroscopy in graphite and nano crystallite graphite. F.Tunstra *et al.* identified that the single crystalline graphite shows only one peak at 1575 cm^{-1} and polycrystalline graphite exhibits one more band at 1355 cm^{-1}. [119] The intensity of the second peak is inversely proportional to the crystallite size in the direction of the graphitic plane. The study correlated the I_D/I_G ratio to the crystallite size using the equation

$$I_D/I_G = C(\lambda)/La \qquad (2.18)$$

Where C is the proportionality constant (C for 515 nm laser is 440 nm). This relation is valid only for low defect concentration and large crystals. This equation was later modified by Lucchese *et al.* for higher defect concentration and lower crystallite size [120]. As the defect in graphite increases, the I_D/I_G ratio also increases to a maximum and then it will start to decrease because of the introduction of amorphous carbon. This initial high defect region, where an increase in the I_D/I_G ratio is observed can be called as nanocrystalline graphite in which the material is completely sp^2 with lot of associated defects. The initial increase in the D peak intensity and the I_D/I_G is because of the increase in the scattering from defects and the later decrease can be attributed to the decrease in all Raman peaks because of amorphous carbon.

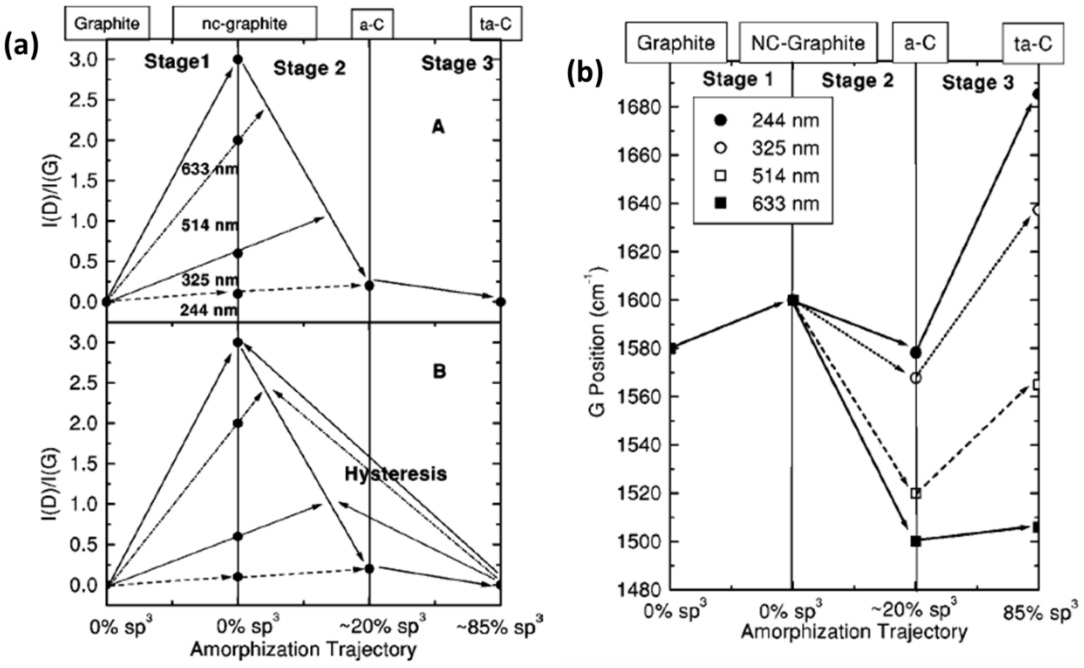

Figure 2.15: Amorphisation trajectory proposed (a) I_D/I_G ratio for different and (b) G peak position for different laser excitations. [121]

Ferrari *et al*. characterized the amorphisation trajectory of carbon from graphite to disordered carbon base on the intensity ratio of D and G peak (Figure 2.15). A 3 stage amorphisation trajectory is identified comparing the I_D/I_G intensity ratio in which graphite transforms in to nanocrystalline graphite in the first stage. Further increase in the defect density leads to the amorphisation of the graphite leading to a sp^2 amorphous carbon and will further lead to the third stage containing completely disordered tetrahedral

amorphous carbon. Depending on this amorphisation trajectory, he proposed that the I_D/I_G ratio is directly proportional to the square of the crystallite size in the high defect region, giving the equation

$$\frac{I_D}{I_G} = C(\lambda)La^2 \quad (2.19)$$

Where C(λ) has a value of 0.0055 at 514 nm laser excitation. In the low defect region the study shows that the relation follows the equation proposed by Tunstra *et al.* This study uses same laser excitation of 514 nm. The later work by Cancado *et al*. [122] generalized the approach to find out the crystallite size taking in to account the excitation wave length of Raman laser giving the equations

$$\frac{I_D}{I_G} = \frac{560}{{E_l}^4}(La) = \frac{2.4\times10^{-10}(\lambda^4)}{La} \quad (2.20)$$

Where E_l is the energy (eV) and λ is the wave length of the laser in nm.

Further in another study Cancado *et al*. [123] showed that the full width at half maximum (FWHM) of all the 3 peaks of graphite is independent of laser excitation and gave the relation between crystallite size and FWHM as

$$\Gamma(\text{FWMH}) = A + B\,La^{-1} \quad (2.21)$$

A and B are linear fit parameters obtained from the plot of FWMH for D G and 2D peaks at different laser energies are given as

FWMH	A(cm^{-1})	B(cm^{-1}nm)
Γ_D	19	500
Γ_G	11	560
Γ_{2D}	26	1000

2.11. Molecular dynamics simulations

To get an atomistic understanding of the different structural changes observed, the *in situ* TEM studies were supported by molecular dynamics simulation. Simulation studies were carried out by Manuel Konrad and Prof. Wolfgang Wenzel at INT, KIT. The molecular dynamics simulations were carried out using the LAMMPS package [124] with the AIREBO force field for hydrocarbons. [125] Nudged elastic band (NEB) calculations [126] were used to calculate the activation energies associated with the structural changes and size reduction. NEB calculations were carried out with the ASE package in conjunction with the semi-empirical solver MOPAC (MOPAC2016, Version: 18.117L) [127], using the PM7 functional. [128] The visualizations of the changes are created with the OVITO software. [129] The NEB method is used to find the saddle point of the minimum energy path between given initial and final atomistic configurations. Therefore, intermediate states of the system (images) are coupled by harmonic springs, which ensure a uniform distribution of sampling points along the path. This coupled system is then minimized, which results in the minimum energy path. Additionally, a climbing image, which doesn't feel any spring forces but tends towards the saddle point, can be used to improve the transition state. Detailed information about this method can be found in Henkelman *et al.* [126]

3. Graphitization and growth of free-standing nanocrystalline graphene

3.1. Introduction

Preparation of different types of carbon materials with varying structure and properties by polymer pyrolysis is a well-studied field. [41,43,46] Advances in carbon based NEMS and MEMS attracted interest in graphitization at smaller length scales for the preparation of carbon materials in different substrates with controllable shape, thickness and properties. [130,131] Since the properties of these graphitized carbon structures are largely affected by the domain size and other defects, a detailed understanding of graphitization and domain growth as a function of temperature is essential for the controlled tailoring of the properties of the graphitic material. This chapter discuss the graphitization and domain growth of free-standing nanocrystalline graphene thin films prepared by vacuum annealing of a photoresist inside a TEM. *In situ* TEM techniques such as HRTEM, selected area electron diffraction (SAED) and electron energy loss spectroscopy (EELS) are used to analyze the graphitization and the evolution of nanocrystalline domains at different temperatures.

3.2. Method development for *in situ* graphitization

Nanocrystalline graphene can be formed from different source materials, which are polymers containing aromatic molecules that can be carbonized and graphitized at higher temperatures. In this study, we use commercially available S1805 photoresist from Microposit. The photoresist was diluted with propylene glycol monomethyl ether acetate (PGMEA) to tune the viscosity and resulting film thickness. Initially *ex situ* studies were carried out to understand the thin film formation and graphitization. The polymer was spin coated onto a Si-SiO_2 membrane (1 cm^2 size) with rotation speed of 8000 rpm. Graphitization was carried out in a quartz furnace under a vacuum of around 10^{-6} MPa. The graphitization temperature was 1000 ºC for 10 hours similar to the previously reported studies. [11]. After graphitization, samples show a Raman signature (Peak positions and I_D/I_G ratio), which is similar to the reported values in the literature.

To perform *in situ* graphitization, it is required to form thin polymer films on MEMS based heating chips. Fusion heating chips without any coating over the holes were used in the study. This is to form large area free-standing thin films which are ideal for TEM characterization. Graphitizing the films on the chip can eliminate defects and artifacts associated with sample preparation and transfer processes. This was

accomplished by spin coating the photoresist directly on the heating chip. Figure 3.1 shows the experimental process flow for graphitization on MEMS based heating chip. The photoresist was diluted with PGMEA with a solution ratio 1:12 to form thin polymer film across the holes. After the spin coating, the electrodes were exposed by carefully dipping the bottom part of the chip in to acetone. The chip was then loaded in to the Fusion TEM holder and an initial heating was carried out in a Gatan TEM holder pumping station at 10^{-6} MPa for 5 hours at 600 ºC. This is to avoid the contamination of the TEM column by the gases evolved during the initial stages of pyrolysis. In the MEMS based heating chip, the heating is confined to the free-standing ceramic membrane that acts as both heating element and sample support and the graphitization only happens at this confined area. This will avoid the formation of conducting ncg on other parts of the chip which may lead to a short between the electrodes. After the initial graphitization, the chip was analyzed with optical microscopy and Raman spectroscopy.

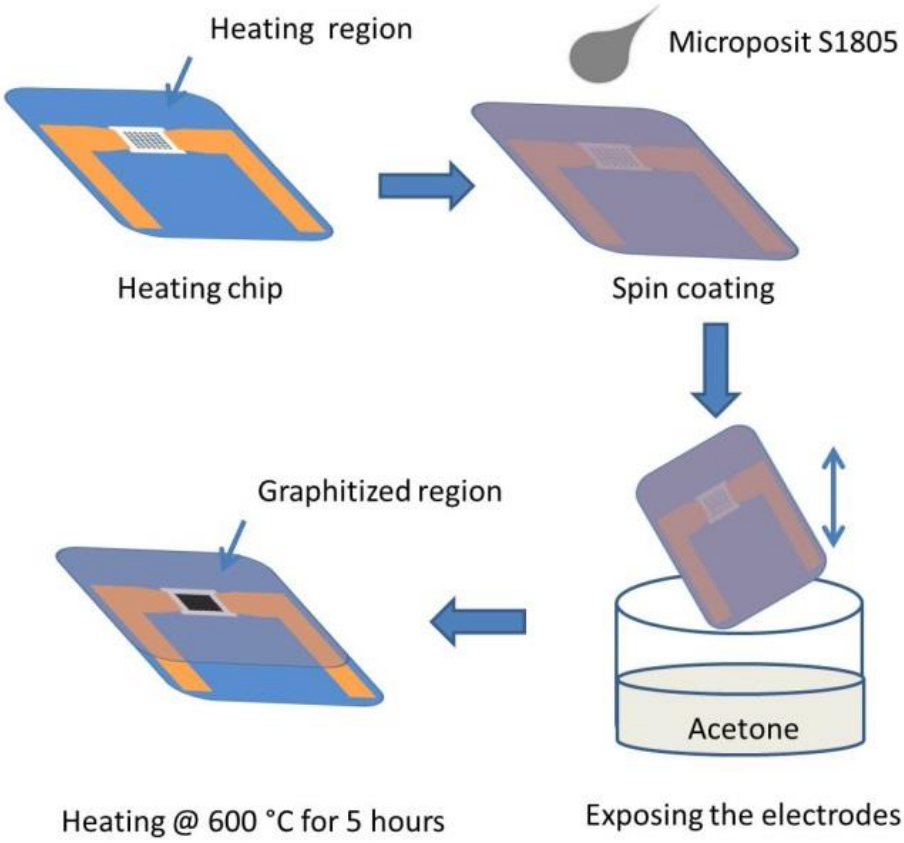

Figure 3.1: Schematic process flow of the graphitization on MEMS based heating device. The chip was spin coated with the photoresist and the electrodes were exposed by dipping in acetone. [132]

3.3. Graphitization of free-standing layer on MEMS device

Figure 3.2 shows the characterization of the annealed photoresist on the heating chip after *ex situ* graphitization at 600 °C. The Raman characterization of the samples was carried out using confocal Raman spectroscopy (Renishaw Raman microscope) with 514 nm laser excitation. Figure 3.2a gives the optical micrograph of the graphitized free-standing area of the heating chip. Carbonized films were formed across the 5 micron diameter holes in the SiN film. This means that a free-standing polymer film was formed across the holes during the spin coating and a substrate free graphitization has happened. The film shows broad D and G peaks at around 1600 cm^{-1} and around 1300 cm^{-1}, which is characteristic of partially graphitized materials (Figure 3.2b). To understand the quality of the free-standing film, the graphitization is compared with a film grown on SiO_2 using otherwise comparable condition. Comparing the Raman signature, we observe that the graphitic character of the free-standing film is similar to the substrate supported film (Figure 3.2b). The G peak position of the free-standing film is compared across the heating area to analyze the homogeneity of the graphitized film formed (Figure 3.2c). It can be observed from the G peak position that the graphitization is homogeneous across the heating area. This shows that with the adopted method, a large uniform film can be grown across the heating area of the chip. Furthermore, to understand the uniformity of the graphitized free-standing film, the I_D/I_G ratio map is acquired across the free-standing film extending to the substrate supported region. Figure 3.2d shows the higher resolution Raman map (I_D/I_G ratio) of the free-standing film across a hole. A uniform I_D/I_G ratio is observed which confirms the uniform graphitization over the free-standing layer. The substrate supported region outside the free-standing area shows a slight reduction in I_D/I_G ratio which can be attributed to the background from the Si supported region. Form the Raman signature (Peak positions and I_D/I_G ratio), comparing it with the graphitization trajectory proposed by Ferrari *et.al* [121], we can conclude that the material is partially graphitized with some amount of sp^3 coordinated amorphous carbon left. This is expected since the temperature is fairly low and does not facilitate complete graphitization.

The experiment shows that free-standing polymer films can be graphitized without support of a substrate and the graphitization yields similar results. This is important from a TEM point of view as a large area, thin free-standing film is ideal for detailed TEM analysis. Since the substrate free graphitization yields similar results, heating this film inside the TEM can provide information about the inherent structural changes happening during pyrolysis. The sample being graphitized on the heating chip itself, it is free from

defects or structural changes that could occur during sample preparation and transfer. The vacuum in the TEM is comparable or even better than the conventional vacuum ovens used for pyrolysis. With all these, the conditions for *in situ* heating inside the microscope are comparable to the normal pyrolysis at small length scales. Thus the structural changes during *in situ* heating can be directly correlated to the real pyrolysis at small length scales. By combining different analytical techniques, this can provide valuable information of the highly dynamic structural and chemical changes during graphitization.

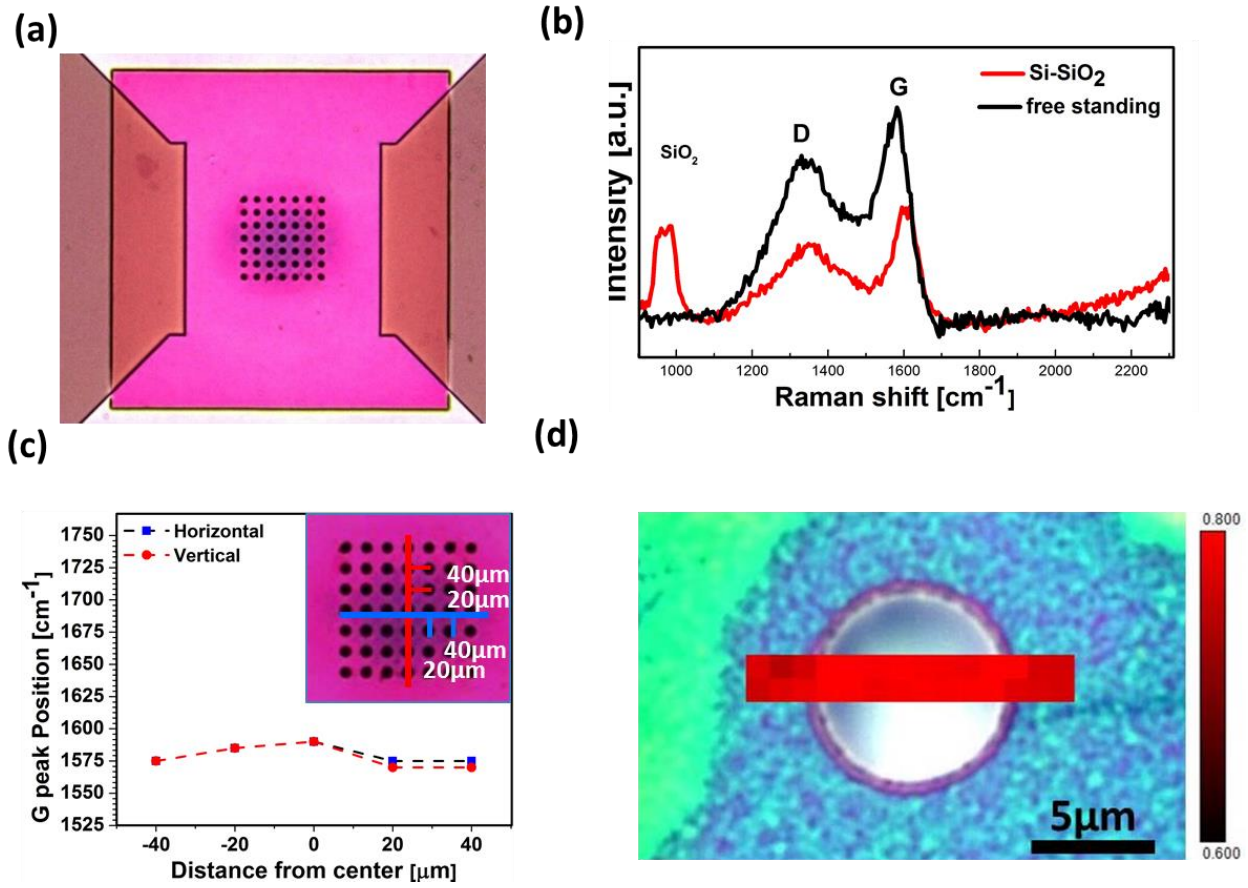

Figure 3.2: (a) Optical micrograph of the graphitized heating area, (b) Raman spectra of film graphitized at 600 °C, (c) G peak position near the center hole on heating chip, (d) I_D/I_G ratio map overlaid on an optical image of a film over a hole. [132]

The *ex situ* partially graphitized samples were heated inside the microscope and imaged starting from 600 °C. Since the samples were already graphitized until 600 °C, no major structural changes are expected to happen below this temperature. A heating rate of 10 °C per minute was always used and the samples were

heated to 600 °C without an electron beam to prevent beam induced transformations. Bright field TEM images and SAED patterns were acquired at every 100 °C interval after holding for 10 minutes. The holding time is to stabilize the temperature and reduce the drift of specimen. The beam was always blanked after imaging to minimize the exposure. Also images from the non-exposed areas were compared at each temperature to analyze the beam induced effect on the graphitization. *In situ* TEM observations were carried out on an aberration corrected (image) Titan 80-300 TEM (FEI company) operated at 80 kV equipped with a Tridium 863 imaging filter (Gatan Inc.).

3.4. Structural evolution during graphitization

Figure 3.3 (a-g) shows a series of bright field-TEM images of the growth of nanocrystalline domains during heating, (h) shows the SAED pattern of the sample graphitized to 1200 °C. At 600 °C the structure is dominated by curved and wrinkled small features. As the temperature increases, formation of domains and its further growth is observed as small domains start to appear by 800 °C. At 1000 °C, clear well defined domains are observed and further heating results in an increase of the domain size. It is well known that, during the graphitization of a polymer precursor, after the initial carbonization, the material consists of small crystallites of hexagonally coordinated aromatic molecules extending up to few nanometers in size with 2-3 layers. [43] These crystallites are separated by disordered carbon and voids in between them. As the temperature increases, two different mechanisms operate, 1. attachment of the disordered carbon to the edges of the crystallites thereby increasing the size and 2. ordering and merging of the crystallites leading to an increase in crystallite size. [41] This can be observed in the images at intermediate temperature (600 °C to 1000 °C), where the film transforms from a disordered structure to well-defined domains. At 1000 °C the domains are clearly visible and subsequent heating results in an increase of the domain and crystallite size by merging of small crystallites to form bigger ones. This high temperature growth by the merging of flakes can be observed (Figure 3.4), where two small domains merge together to form a large one during heating from 1100 °C to 1200 °C.

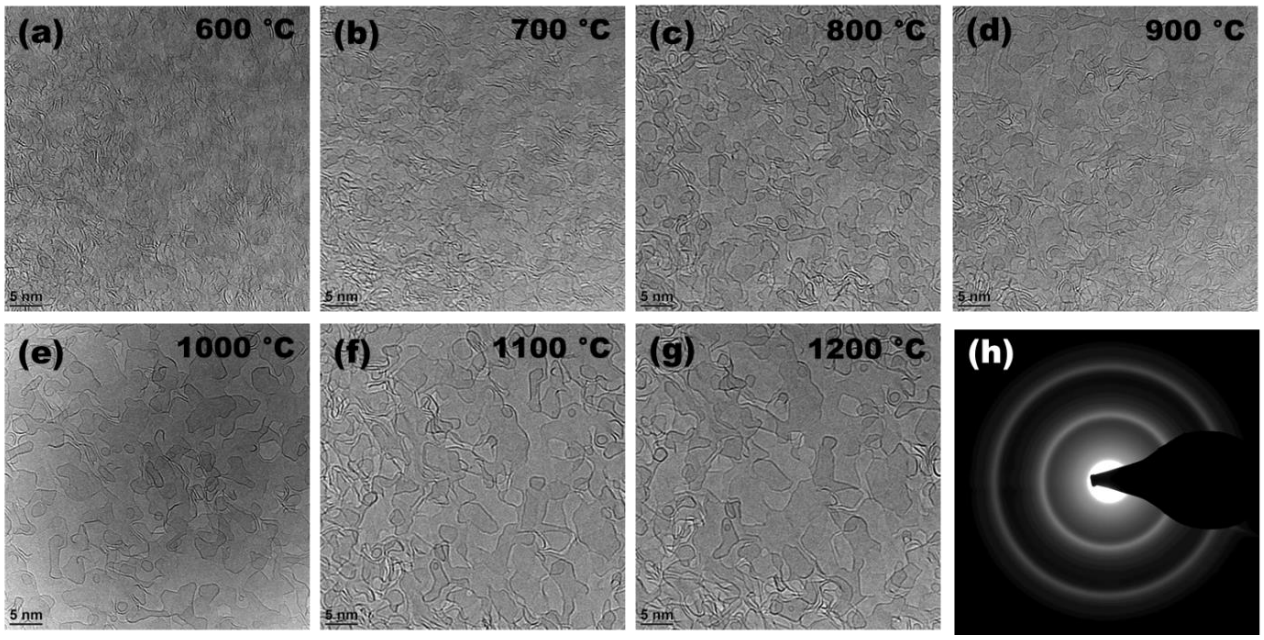

Figure 3.3: (a-g) Growth of nanocrystalline domains and (h) crystallite size with increasing temperature.

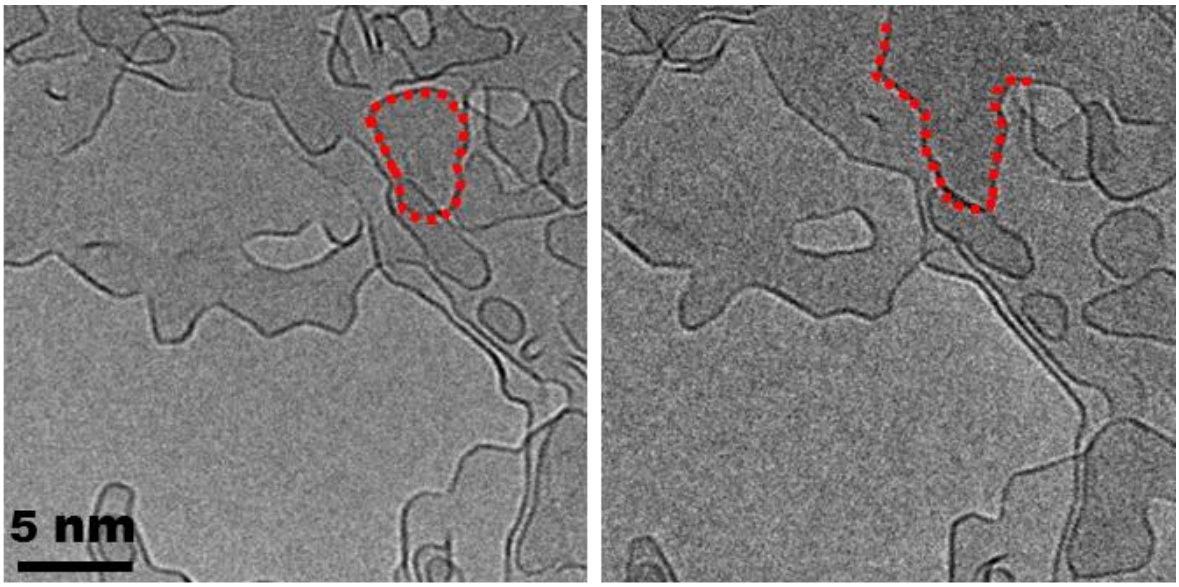

Figure 3.4: Merging of smaller domains to form larger ones during heating from 1100 °C to 1200 °C. [132]

3.5. SAED Analysis

SAED patterns were recorded along with the bright field images which provide information about the orientation and crystallite size. Figure 3.5a shows an intensity profile of the SAED patterns acquired at

different temperatures. The intensity profiles show two prominent peaks at 4.8 nm^{-1} and 8.5 nm^{-1}. These two peaks correspond to {100} and {110} planes in graphitic carbon. It should be noted that there is no indication for an {002} peak at around 2.9 nm^{-1}. This means that the growth of graphene is in plane with a strong [001] texture. The FWHM is reducing with increasing temperature, which can be attributed to crystallite growth during heating. In agreement with the ordering observed at around 800 °C in BF-TEM, a weak diffraction ring corresponding to (200) starts to evolve at 800 °C. This ring becomes more prominent at higher temperatures indicating an increasingly ordered crystallite structure. The crystallite size evolution was determined from SAED intensity profiles (Figure 3.5b) using a simple Scherer analysis of the {100} diffraction rings. [89,132] There is an increase of average crystallite size from 2 nm at 600 °C to 3.2 nm at 1200 °C. The observed crystallite size in the BF TEM images seems to be higher (6-8 nm) than the crystallite size obtained from the Scherer analysis. The difference arises from the fact that the electron diffraction measures the coherent scattering size, whereas the BF-TEM images are not very sensitive to small-angle boundaries and individual defects.

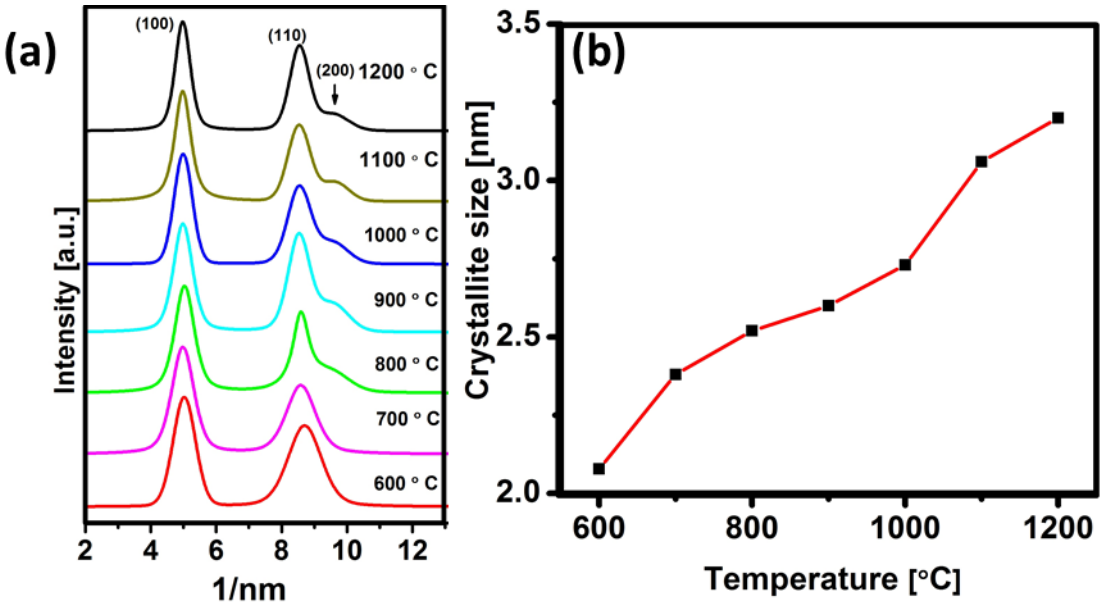

Figure 3.5: (a) Evolution of intensity profile and (b) crystallite size evolution with temperature.

In simple terms, this means that the observed domains in the BF TEM image need not be single crystals, but contains defects or small angle boundaries. Previous reports on *ex situ* graphitization on different substrates [11,25]at 1000 °C show a comparable crystallite size (2.7 nm). This indicates that the temperature

dependence of graphitization in free-standing films is comparable with the substrate supported graphitization.

3.6. EELS spectroscopy

EELS low loss and core loss spectra of the carbon edge were recorded at each temperature to further understand the structural evolution. Figure 3.6a. gives the carbon core loss edge at different temperatures during heating. At 600 °C, the core loss edge of carbon contains a low-intensity π^* peak at 285 eV and followed by a featureless σ^* and extended near edge region. The peak at 285 eV corresponds to a transition from the 1s to π^* orbital and shows the presence of sp^2 bonding in the material. The EELS spectrum at 600 °C is similar to the typical spectrum obtained from amorphous carbon films. This shows the structure of the material at 600 °C containing considerable amount of sp^2 and sp^3 bonding. [133] As the temperature increases, three major changes are observed in the carbon core loss edge: 1) the intensity of the π^* transition increases indicating an increase in sp^2 character, 2) evolution of a clear σ^* peak with a well-defined ELNES region indicating an increased graphitic order [134,135] and 3) evolution and increase in the intensity of the multiple scattering resonance (MSR) peak around 330 eV. [59] This evolution can be attributed to a decreasing variation in nearest neighbor and next nearest neighbor atomic distances and reflects the formation of well-defined coordination spheres. All these changes in the core loss spectra can be attributed to the increase in the graphitic content and also to the ordering of the crystallites. To understand the evolution of the sp^2 content quantitatively in the graphitized layer at different temperatures, the integrated intensity ratio of the π^*over the $\pi^* + \sigma^*$ transition is compared to a fully graphitized standard. [99] The integrated intensity of the π^* peak is calculated using a 5 eV window from the onset of the peak at 282.5 eV and the $\pi^* + \sigma^*$ integrated intensity is calculated using a 50 eV window starting from the same region. For statistical analysis five spectra from different places are acquired at each temperature. Figure 3.6b shows the calculated sp^2 content during pyrolysis. The sp^2 content increases from 70 % at 600 °C to almost 100 % at 1000 °C. This shows the transition from a disordered amorphous carbon structure at 600 °C to a completely graphitic structure at 1000 °C. A two stage growth mechanism can be identified here in which the intermediate temperature (600 °C to 1000 °C) growth of domains is mainly facilitated by consuming amorphous carbon around the domains and the high temperature growth (1000 °C to 1200 °C) proceeds by merging of graphitic domains.

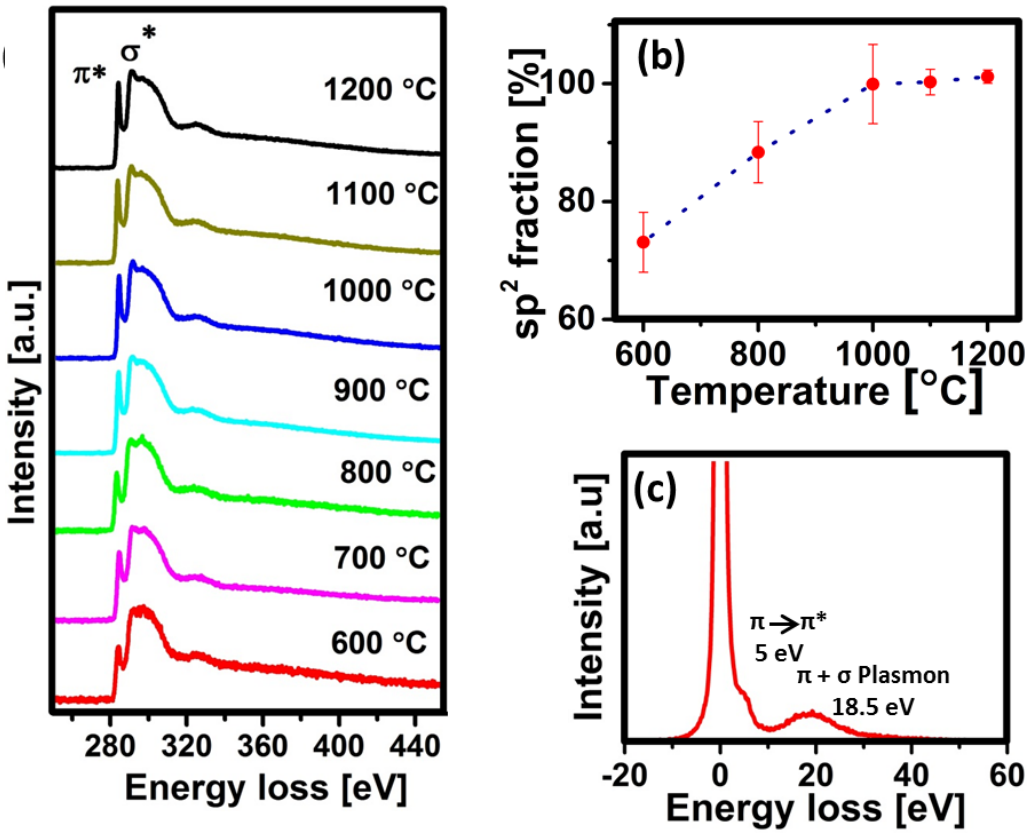

Figure 3.6: (a) EELS carbon core loss at different temperatures; (b) sp2 content at different temperatures and (c) low loss region of the free-standing layer at 1200 °C.

Figure 3.6c shows the low loss spectra of the free-standing film after graphitizing to 1200 °C. The low loss shows two distinct peaks around 5 eV and 18.5 eV, where the first peak corresponds to the π-π^* inter-band transition and the second one shows the collective oscillation of π+σ plasmon. These two peaks are sensitive with the thickness of the film. For single layer graphene, the π-π^* transition which is mainly due to the in-plane mode, appears at 4.8 eV. As the thickness increases the peak will shift towards higher values and appears at 7 eV for graphite. The π+σ Plasmon peak also shows a shift from 15 eV for graphene to 27 eV for graphite. [136] From the position and the structure of the peaks in low loss region and core loss region at 1200 °C, we can conclude that the structure consists of few layers of highly graphitic material

3.7. Raman spectroscopy of the structural evolution

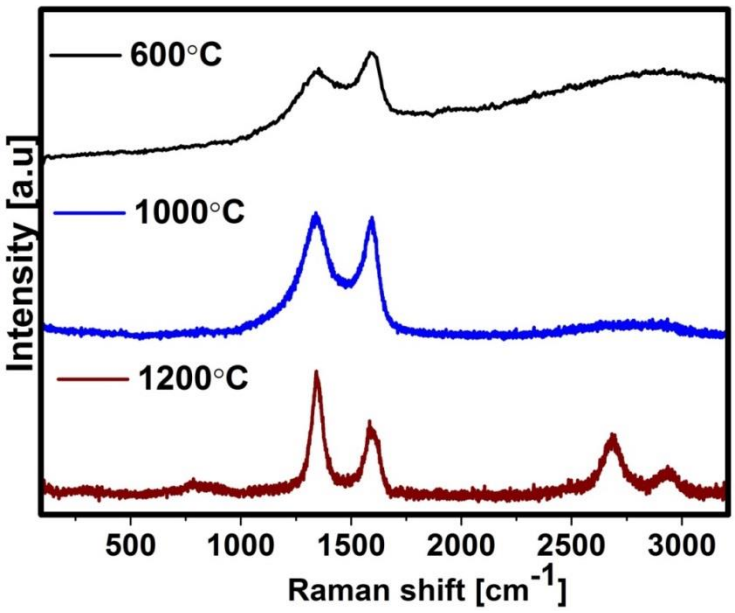

Figure 3.7: Raman spectra of samples graphitized at different temperatures.

To compare the TEM results, Raman spectra of sample heated to different temperatures were acquired. The first Raman spectrum was acquired at 600 °C after the initial *ex situ* heating. Two more spectra were collected after heating inside the TEM for 1 hour at 1000 °C and 1200 °C respectively. Figure 3.7 shows the evolution of Raman spectra with the temperature at 600 °C, the spectrum is similar to an amorphous carbon film with broad D and G peaks. The D and G peaks become sharp and I_D/I_G ratio increases during subsequent heating. At 1200 °C, the spectrum consists of sharp D and G peaks. The I_D/I_G ratio is 1.25 and the position of G peak position is 1585 cm^{-1}. This I_D/ I_G ratio (1.26) and G peak position (1585 cm^{-1}) confirms that the sample is fully graphitic in nature. This is also in agreement with the graphitization trajectory suggested by Ferrari *et al*. [118] The development of sharp 2D and D+G peaks at 1200 °C further shows the highly crystalline nature of the free-standing films.

By combining HRTEM imaging, SAED, EELS and Raman spectroscopy, we can understand the graphitization and growth of domains during pyrolysis. The graphitization observed here fits well with models proposed for the graphitization and crystallite growth during heating from different source materials. [41,43,52] As discussed in the introduction, after the initial carbonization of the polymer, at intermediate

temperatures, the structure consists of small misoriented crystallites containing 3 to 4 layers of hexagonally coordinated aromatic molecules with sizes extending up to a couple of nanometers. The space between these crystallites is filled with uncoordinated amorphous carbon or voids. The degree of misorientation of crystallites and the number of voids, decide on the further graphitizability of the material. [41–43,52]. The transformation from an initially disordered, partially graphitized structure to an ordered graphitized structure can be observed from the *in situ* TEM and Raman analysis. From the TEM images, transformation of domains from small misoriented crystallites in to more extended and ordered structure can be observed. This transformation and growth is also visible looking at the decreasing width of the (100) peak in SAED and the appearance of the (200) peak. From the EELS spectra we can see an increase in the sp^2 content, which shows the conversion of disordered carbon to a sp^2 carbon, which means that the amorphous carbon around the domains is consumed during this temperature range. This growth continues until the sample is almost completely graphitized at around 1000 °C. At temperatures above 1000 °C, the growth of the crystallites mainly proceeds by coalescence of the small crystallites. It should be noted that, in the present study, the layer formation is imaged for a completely free-standing film and the final structure of the graphitized film at 1200 °C is comparable to the graphitization of substrate supported films. This can be observed from the comparable average crystallite size and sp^2 content of the film grown on different substrates. [1,11,25,35]

3.8. High resolution imaging of the graphitized layers

To understand the structure of the graphitized film, HRTEM images were acquired immediately after cooling down from 1200 °C (Figure 3.8). HRTEM images show that the structure is highly defective, both with a lot of defects within the layers (marked by red arrow) as well as disordered edges. Extended graphene domains are stacked on top of each other with lot of small graphitic structure with size of 2 nm or less (marked by white arrows). The edges are disordered and do not show well defined facets which means that the edges may contain unsaturated bonds, non-six membered or a mixture of zigzag and armchair configuration. [20,137] Nevertheless, during extended heating we observe a transformation from curvy and disordered edges to more defined faceted edges (Figure 3.9).

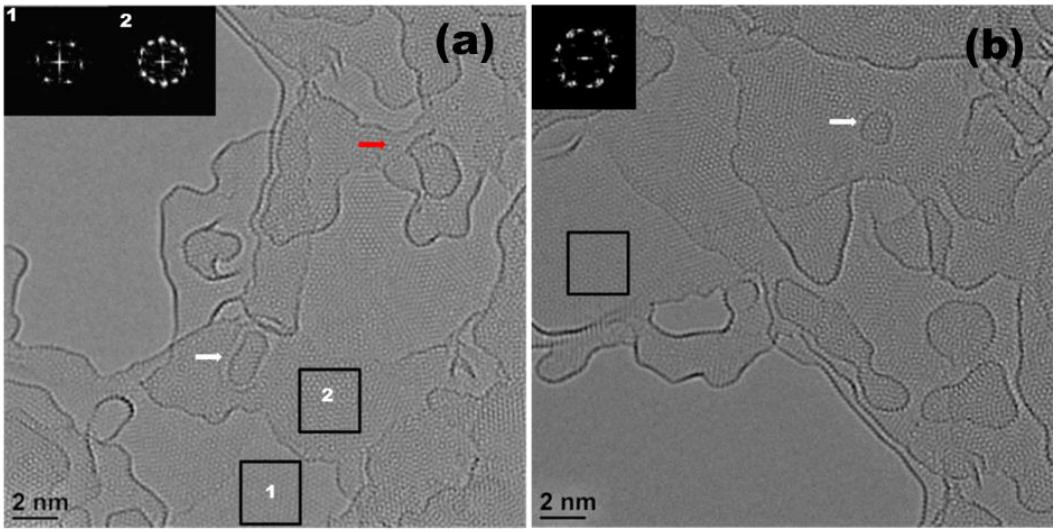

Figure 3.8: HRTEM images of a thin region heated to 1200 °C.

FFTs from two different regions are compared to understand the stacking of layers (Figure 3.8a). The first FFT shows six reflections corresponding to a single crystalline region, whereas the region marked as 2 contains another set of spots rotated by 22°. This corresponds to few layers of graphene misoriented by 22°. Similar misorientation between the layers is observed in the marked region (Figure 3.8b) and in other regions in the sample. This misorientation angle (21.79°) is commonly reported in multilayer graphene, corresponding to a low energy commensurate structure. [138–140] Similar rotation angles have been reported during catalyst free transformation of amorphous carbon on the top of a graphene substrate. [64]

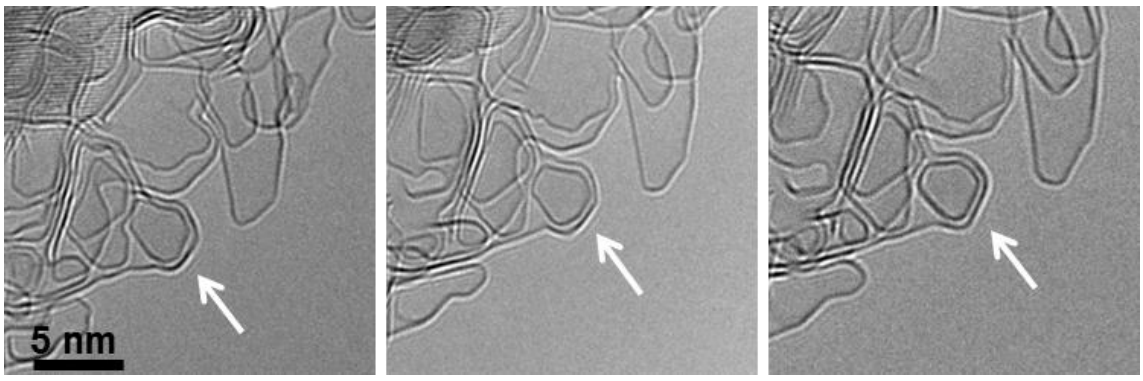

Figure 3.9: BF-TEM images of transformation of a domain with disordered edges to defined faceted edges during prolonged heating.

3.9. Reheating of ncg

HRTEM images of the graphitized samples show the presence of lot of carbon nanostructures on the top of the graphitized layers, even after heating to 1200 °C. These small structures are formed by the catalyst free transformation of amorphous carbon on the top of the graphitic substrate during intermediate temperatures. To understand the formation and dynamics of these carbon nanostructures, reheating experiments were carried out inside the TEM. *In situ* graphitized samples were taken out and exposed to the atmosphere. Exposing the samples to the atmosphere, after the first heating to 1200 ºC, resulted in the deposition of carbonaceous material on the top of the already graphitized samples. This is expected since the structure contains lot of free edges and active surface, favorable for adsorption of carbonaceous material. The structure consisting of active edges with a lot of amorphous carbon around is similar to the initial stages of graphitization where the crystallites are surrounded by amorphous carbon or voids. Thus reheating experiments can provide insights in to the structural changes during initial stages of graphitization and the dynamics of carbon nanostructures during heating. During the reheating experiments, images were acquired every 10 °C and the structure compared to non-exposed areas at each temperature.

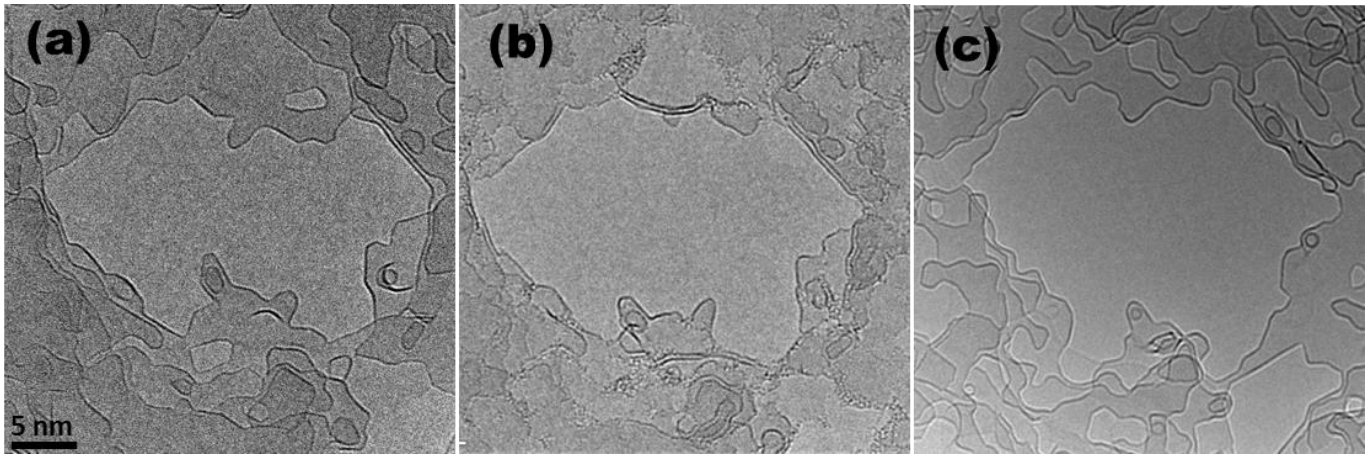

Figure 3.10: Deposition of amorphous carbon on the sample (a) sample before adsorption of amorphous carbon (b) sample with adsorbed amorphous carbon and (c) after reheating to 1200 °C. After reheating the sample, the amorphous carbon completely graphitizes.

Figure 3.10 shows a region in the sample after the first heating, after exposing to atmosphere and reheating inside the TEM. After the reheating, it can be seen that the amorphous carbon completely transformed.

During this reheating, two main transformations are observed for the amorphous carbon. 1) Amorphous carbon near domain edges attaches to the edge of the domain, increasing the size of the domain. 2) Amorphous carbon graphitizes on the top of the graphitic substrate to form different carbon nanostructures. The size/shape of these nanostructures is varying and they are highly mobile and can merge with edges of neighboring domains. Some of the observed structures have sizes comparable to fullerenes and could be cage-like structure. [104,141] The observed dynamics of the nanostructures is in agreement with previously reported studies. Current annealing experiments on graphene shows the catalyst free transformation of amorphous carbon absorbed on graphitic substrates to nanocrystalline graphene sheets. [64] It is shown by experiments and molecular dynamic simulations that the amorphous carbon on top of graphene will not sublimate but rather graphitize on the top of the graphitic substrate forming graphene nanoflakes. At higher temperatures, these nanoflakes merge forming larger graphene sheets. It is interesting to note that similar to what has been observed in the present study, a misorientation of 22°, was often observed between the layers. Thus the formation of graphene nanoflakes can be due to the catalyst free transformation of amorphous carbon on the top of the graphitic substrate.

We also observe some structures, which appear to be cage-like structures with a size comparable to fullerene. This formation of cage-like structures with sizes of less than 1 nm can be by bending and closing of small flakes formed during conversion. A similar mechanism has been reported by Chuvilin et al. [79] under the influence of the electron beam. Beam induced transformations result in knock on damage at the edges, leading to formation of pentagons and thus subsequent bending. Another similar study on transformations of small flakes into fullerene by repeated addition of atoms by an add-atom mechanism from a graphene edge has also been reported. [112] Adding atoms at the edge results in the formation of pentagon and heptagon rings which induces bending and formation of cage structure. The key to the folding of the small flakes is the formation of non-six membered rings. Even though the reported transformations are observed under the influence of the electron beam, in the present study, similar structures are observed in previously unexposed areas also. This means that the transformation can happen without the electron beam. At higher temperatures, the structures are highly dynamic with active edges, the formation of non-six membered rings can apparently happen without the electron beam. This could trigger the bending and closure of the edges as heating may provide the favorable condition.

These different nanostructures formed by the catalyst free transformation of amorphous carbon are highly dynamic at high temperatures. These structures are mobile on the surface of larger graphene domains and combines to form bigger domains when heated further. Figure 3.11 shows a similar dynamics of a carbon nanostructure during reheating. The carbon nanostructure (size less than 1 nm) is migrating and attaching to an edge extending the edge during reheating. This structure presumably formed during the reheating, at intermediate temperatures (475 °C to 500 °C), detaches from a minor edge and move on the graphitic substrate towards the edge of a larger domain. The migrated nanostructure attaches to the new edge. As the temperature increases (675 °C to 700 °C), both graphitic structures merge at the edge of the layer, extending the graphene sheet.

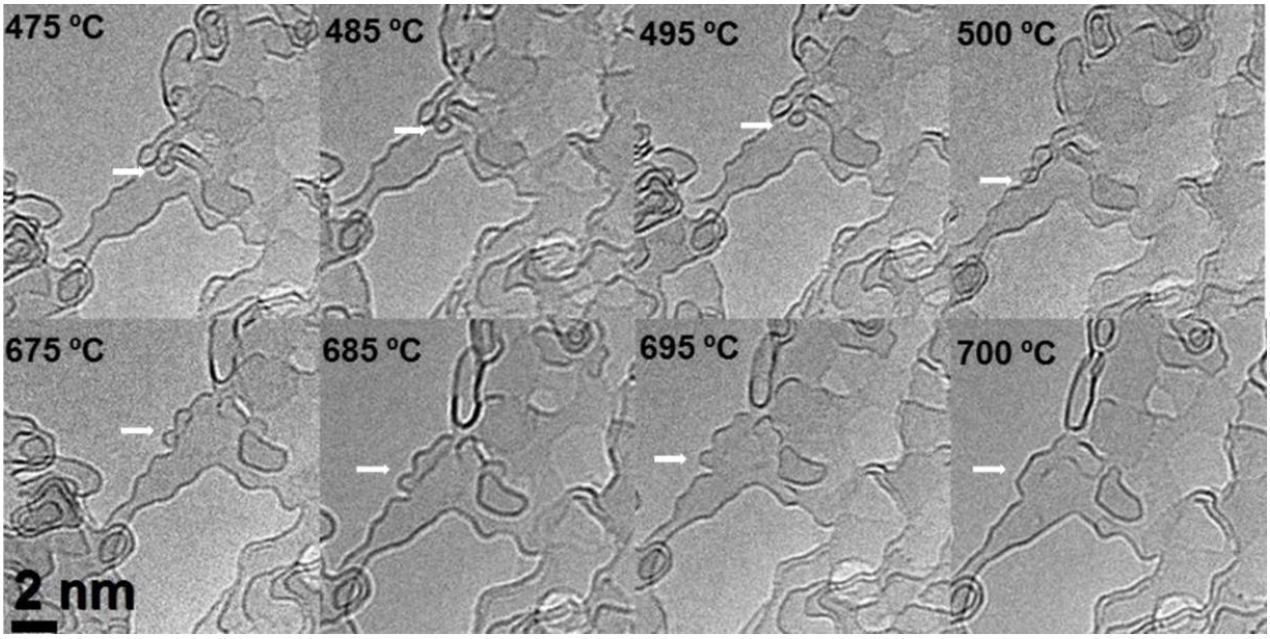

Figure 3.11: Migration and merging of a small graphitic domain.

Figure 3.12 c indicates the region where the nanostructure in previous figure (Figure 3.11) has merged with the edge. This image confirms that the small structure completely merged with the layer without noticeable discontinuity.

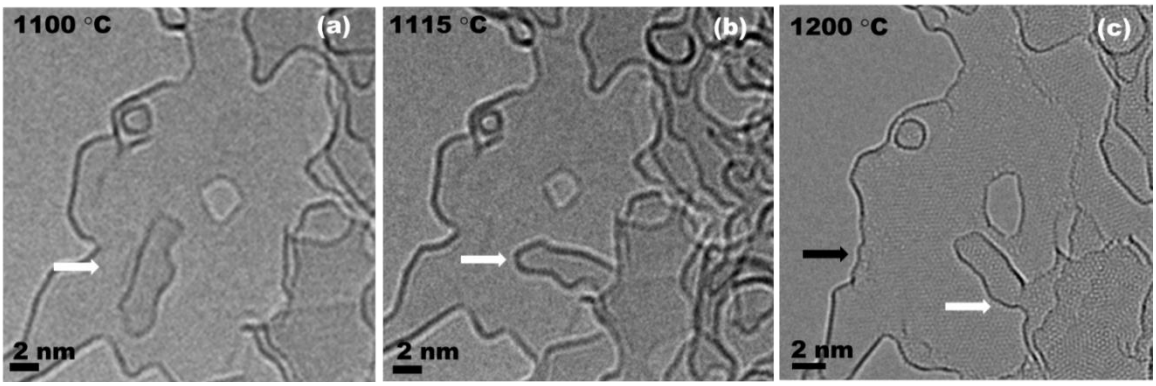

Figure 3.12: Migration of a small graphitic structure during heating merging with a domain edge (marked by white arrows). The black arrow shows the area where a small cage-like graphitic nuclei merged without discontinuity.

Figure 3.13 shows HRTEM images of the merging of two similar sized nanostructures. The nano structures are coming close and merge during heating to 1200 °C. It can be observed that there is a shape change in the small structures during merging. A similar shape change can be observed in the small structures adjacent to the merging structures. These structures are presumably flat flake-like structures with open edges formed by transformation of amorphous deposits, which are probably merging by bond formation between the open edges of the flake. These observed dynamics suggests that different nano structures with varying size shape and mobility are formed by the catalyst free transformation of amorphous carbon.

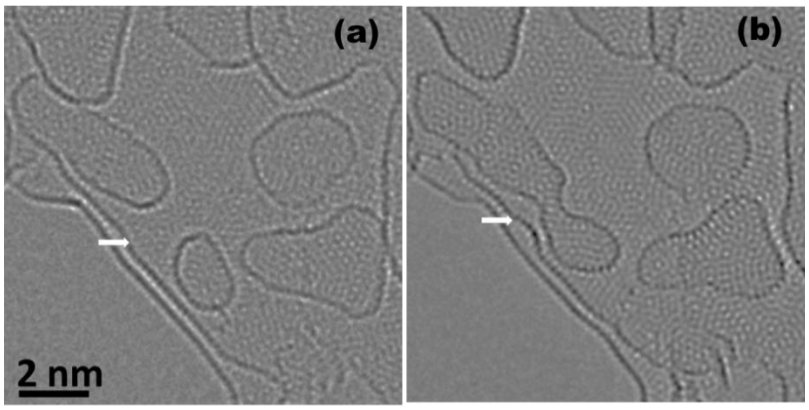

Figure 3.13: HRTEM images of the merging process of two similar sized domains.

Apart from the highly mobile structures we could observe some pinned structures that are not moving even after two cycles of heating. The immobility of these small structures is an interesting observation which is opposite to the already reported high mobility of the carbon nano structures on the top of graphitic substrate. Even more, cage-like structures are expected to be more mobile than the planar structures due to their weaker interactions with the substrate. However, with the substrate structure being far from perfectly crystalline, there are a considerable number of defect sites (sp^3 centers, voids, grain boundaries) which could pin the motion of small graphitic structures.

Apart from pinning, the size and the shape of these trapped structures are changing during heating. The size of the trapped structures reduces after reheating (Figure 3.14). This reduction in size is also observed in other structures during prolonged heating. This means that the structure is losing individual atoms or group of atoms and these detached atoms can move on the top of the graphitic substrate.

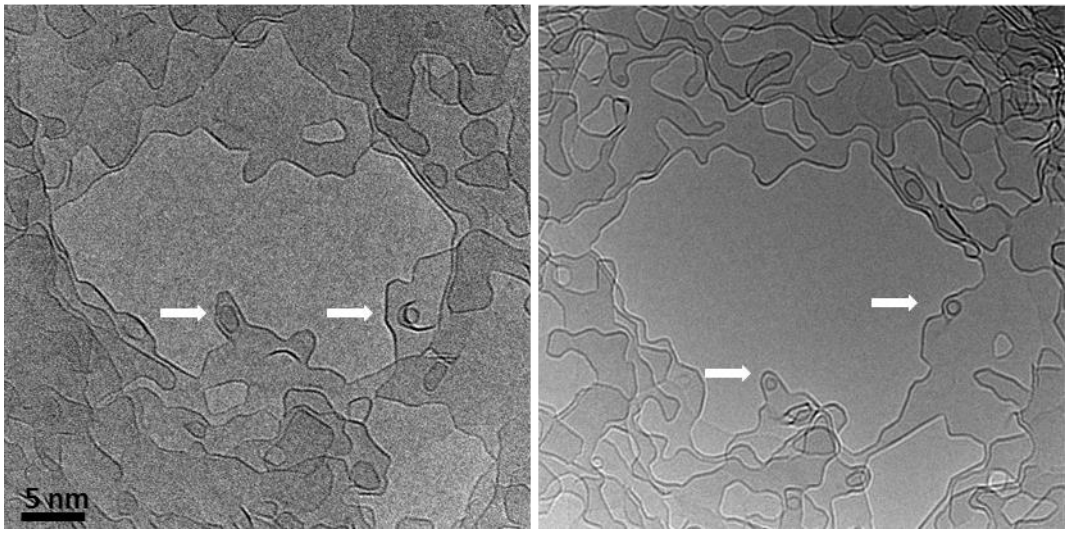

Figure 3.14: Trapped structures before and after reheating.

3.10. Conclusion

In situ TEM studies were performed to understand the graphitization and grain growth in nanocrystalline graphene during heating of a free-standing polymer film. Thin polymer films were formed on the top of the MEMS based heating chips by spin coating. Graphitizing the films on the chip eliminates defects and artifacts associated with sample preparation and transfer processes. The graphitization of the free-standing

film is comparable to substrate supported graphitization. *In situ* TEM studies showed that graphitization and grain growth during pyrolysis is a highly dynamic process with a lot of intermediate reactions and steps. With free-standing films showing graphitization comparable to the substrate supported heating, we can directly correlate the structural changes during *in situ* heating with conventional thin film pyrolysis processes. A two stage growth process was identified: growth of the crystallites in the intermediate temperature range of 600-1000 °C mainly occurs by consuming residual amorphous carbon around graphitic domains; at higher temperatures of 1000-1200 °C, growth proceeds by merging of mobile domains. The amorphous carbon transforms in one of two ways, either by attaching to active edges of graphitic domains or by catalyst free growth on top of a graphitic layer. The catalyst free transformation of amorphous carbon forms new small graphitic structures, some of which are highly mobile at higher temperatures and get attached to the edges, extending the edges. Apart from merging, the study also showed shrinking of pinned nanostructures by the detachment of atoms or group of atoms from the small pinned nanostructures.

4. *In situ* high temperature studies on nano crystalline graphene

4.1. Introduction

The *in situ* graphitization presented in the previous chapter showed the presence of carbon nanostructures with varying size, shape and mobility formed due to the catalyst free transformation of amorphous carbon on top of a graphitic substrate. *In situ* high temperature studies on ncg provide the possibility to understand the stability/dynamics of these nanostructures and their interaction with the graphitic substrate. Analyzing these interactions can help to understand the fundamental mechanisms that control graphene growth at high temperatures. Even though lot of research has been performed in the area of high temperature behavior of graphene using *in situ* TEM techniques, most of these studies are on single layer graphene with a focus on the stability and dynamics of individual defects or small groups of defects. [17,65,114,142] On the other hand, *in situ* TEM studies of the behavior of small carbon nanostructures on top of a graphitic substrate are mostly carried out at room temperature and the transformations were driven by electron beam induced effects. [79,143–145] The ncg films with a high density of defects, active edges and carbon nanostructures used here, provide a completely different system to study the high temperature dynamics and reactions of carbon nanostructures. *In situ* heating of nanocrystalline graphene combined with molecular dynamics studies provide an atomic level understanding of the fundamental processes during growth of ncg. This leads to better structure property correlations and eventually contributes to an efficient tailoring of the properties. This chapter discusses a series of *in situ* high temperature experiments to understand the high temperature dynamics of ncg. Time resolved HRTEM investigations, supported by molecular dynamics simulations, were carried out to identify characteristic processes during high temperature heating and assess their role in polymer pyrolysis.

The *in situ* studies were carried out using an aberration corrected (image) Titan 80-300 TEM (FEI Company) operated at 80 kV equipped with a US1000 slowscan CCD (Gatan Inc.) camera. The samples were heated at 10 °C per minute until the desired temperature is reached. Image acquisition was carried out at intervals of 5 seconds with a 1 second exposure time. The beam was blanked in between image acquisition to minimize beam-induced effects. The dose for each high-resolution TEM image varied between 2.0×10^7 e/nm^2 and 4.1×10^8 e/nm^2 depending on the magnification. To understand the structural changes in detail, we carried out 16 different heating experiments at various temperatures using 4 different samples. Due to

the high dynamic nature of the samples, more than hundreds of different events were observed during heating. Out of this, 30 different events were analyzed in detail to understand the main structural changes occurring during heating.

4.2. Migration of nanostructures

As already discussed, amorphous carbon is deposited on the graphene film every time the sample is exposed to atmosphere. This disordered carbon transforms and forms new nanostructures during every reheating process. Thus the amorphous carbon acts as a continuous source for new nanostructures, which helps to image and understand the dynamics of these structures at high temperatures. During continuous imaging, we observed nanostructures appearing and disappearing from the field of view, which shows that the nanostructures are highly dynamic at these high temperatures and can move fast on top of the substrate.

Figure 4.1 shows the dynamics of a small graphitic flake at 1200 ºC. The flake is not visible for the first 590 seconds (118 frames) of observation and migrates in to the field of view in the next frame (Figure 4.1b).The flake is pinned at this position for the next 100 seconds (20 frames). It moves to a nearby positon and comes back to the original position in next two frames. (Figure 4.1c,d). The flake remains at this position for the next 420 seconds (84 frames),then it quickly moves and attaches to an edge around 10 nm away. The nanostructure completely merges with this edge, thus extending it (Figure 4.1g). This observed migration is not in agreement with the previously reported high mobility of carbon nanostructures on top of graphitic substrates. GNF are known to be highly mobile on the top of defect-free graphitic substrates. Super fluidic behavior of graphene nanoflakes even at temperature as low as 5 K has been reported experimentally. [146] The theoretically calculated diffusion coefficient for GNF on top of defect-free graphene substrates at 300 K is $6.7\pm0.6\times10^{-6}$ cm^2/sec [147], which is significantly higher than the observed diffusion here. In fact, it would be difficult to clearly image nanostructures moving so fast with the present large acquisition time. However, in the case of nanocrystalline graphene with a high defect density, the defects are playing an important role in the observed dynamics. It is known that defects result in unsaturated bonds and strain fields in the graphene lattice. This can lead to local rearrangements and induce vertical displacements of carbon atoms close to the defect. [148] This displacement can cause bond formation between the unsaturated atoms at a flake edge and the defect site, thus pinning the flake. Molecular dynamics simulations also show the bond formation with underlying defects (Figure 4.2). MD simulation at 1500 K shows high diffusion

coefficient for the nanoflake on the top of defect free graphitic substrate. However the fast migration is largely hindered by the introduction of defects in the substrate. The nanoflakes tend to from bonds with the underlaying defects and this pins the flake to the defect. This can be observed in MD simulations (Figure 4.2 a) where the moving flake forms bond with the defect and it is pinned.

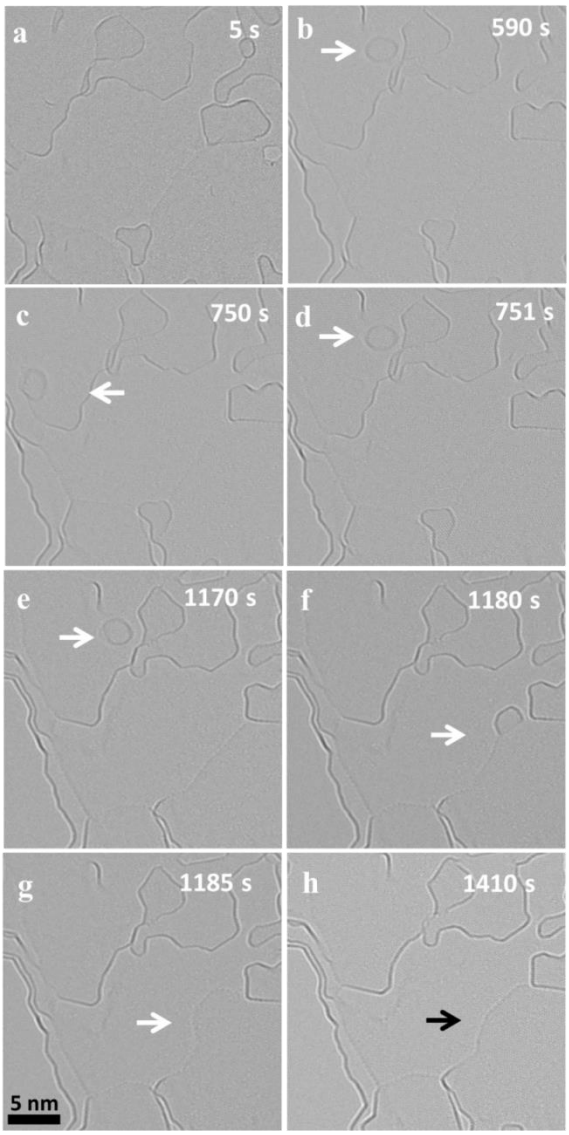

Figure 4.1: (a-h) Migration and merging of a nano-flake during heating at 1200 °C. The time stamp corresponding to each snap shot is shown as label in each micrograph.

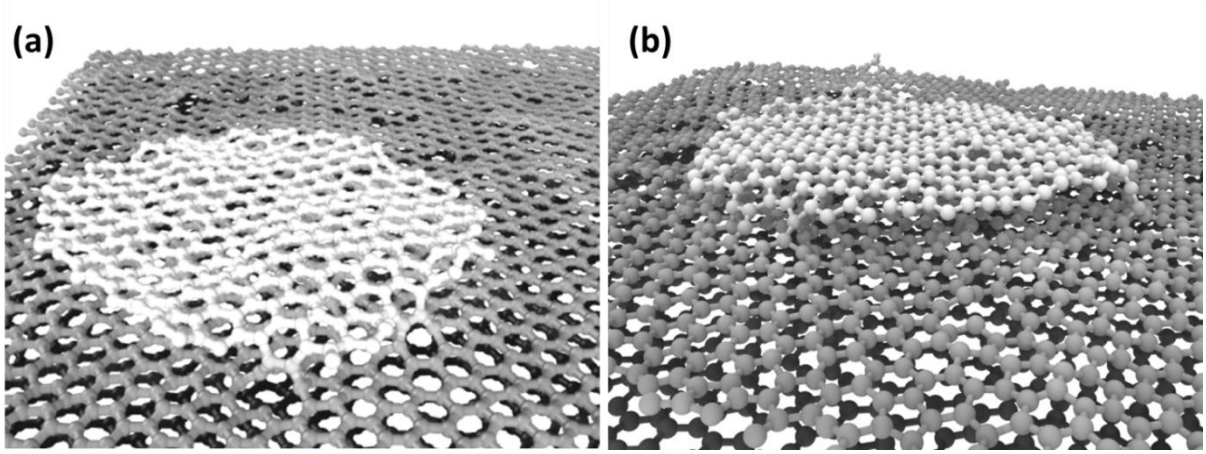

Figure 4.2: Pinning of defects to the underlying defects.

The nanoflake edges are observed to be highly reactive and constantly rearranging at high temperatures, which is favorable for bond formation and pinning. Depending on the number of defect sites, there can be simultaneous pinning at more than one site, which will further reduce the diffusion speed of the flakes (Figure 4.2b). This explains the observed low diffusion of the nanoflakes at high temperatures, which are not in agreement with the reported high diffusion of nanoflakes. The observed high structural dynamics of nanoflakes is in agreement with the theoretical studies on high temperature behavior of GNF. Previous ab initio calculations revealed strong out-of-plane vibrations for edges of an isolated nanoflake at high temperatures. [149] This structural vibrations of the edges are fast compared to the exposure time used in the experiments, so that only an average can be observed in the TEM images. Moreover, our simulations suggest that rearrangement of the edges are fast compared to the exposure time used in the experiments, so that only an average edge structure can be observed in the TEM images.

Apart from the nano flakes, we also observe structures that look similar to cage-like structures which show constant edge contrast (Figure 4.3). These structures also migrate and pin to defects, but we have not observed merging for these closed structures. This high shape and size stability can be attributed to the closed cage structure, which is known to be stable and less reactive. Nevertheless, these experimental results show that the defects play a major role in the migration of these nanostructures on the top of defective graphene.

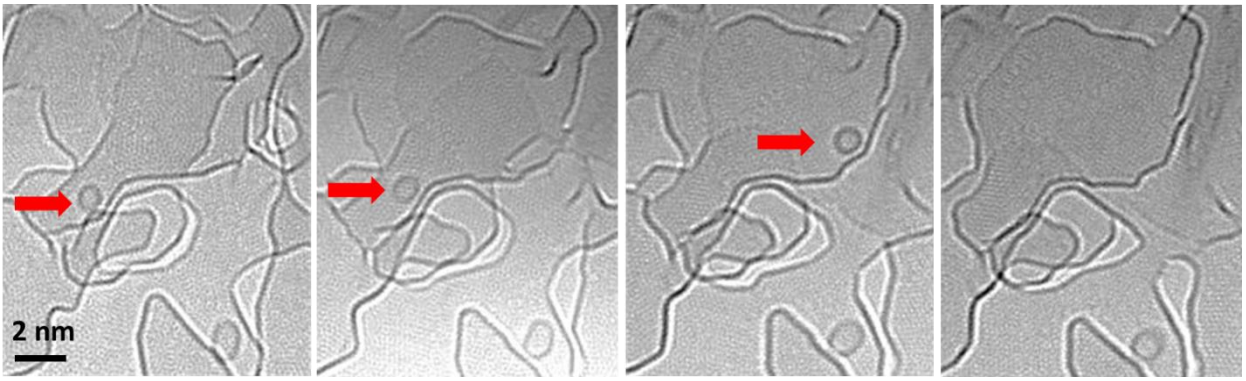

Figure 4.3: BF-TEM images show migrating cage-like nanostructure during continuous imaging for 30 minutes at 1200 °C.

4.3. Lateral and vertical merging of nano flakes

As observed in Figure 4.1, the migrating nanoflakes often merge with large flake edges during high temperature heating. The nanoflake observed in Figure 4.1 merges with a layer on the same graphene plane by lateral materials transfer. As seen in the images, this lateral merging is fast, the complete merging happened within a couple of frames. This merging depends on the mobility of the flake (the defect density of the support) and the availability of suitable edges to merge. As the structure of ncg consists of stacked graphitic domains with a lot of locally varying defects and free edges, the frequency of merging events can vary considerably. 10 different lateral merging events were analyzed and in all the cases, the distance and the time of merging were different.

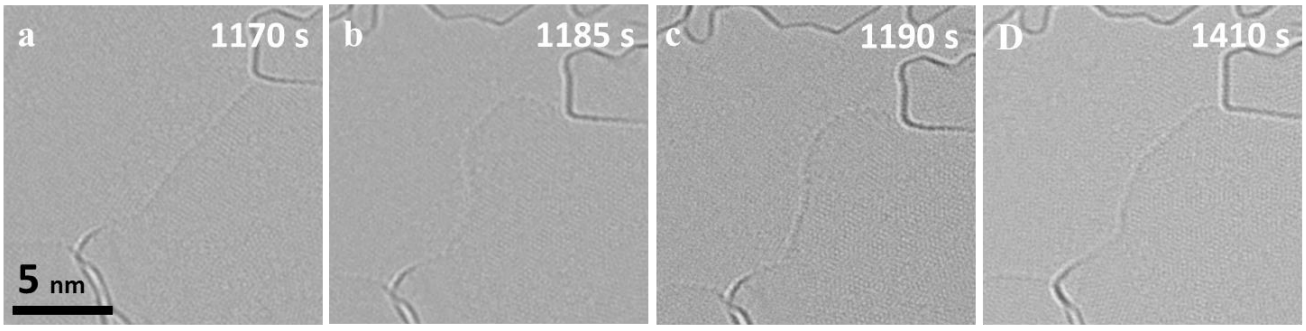

Figure 4.4: Dynamics of the large flake edge (a) before the attachment, (b) attachment of additional mass from the flake and (c,d) flake edge after complete distribution of additional mass. Parallel line like moiré patterns can be observed at the flake edge.

Similar to edge fluctuations in the smaller flakes, the large flake edges are also dynamic and constantly rearranging. The edge at which the small flake is merging is highly dynamic. After the merging of the flake, the additional mass is redistributed quickly and the flake tries to reduce the overall curvature until it reaches a flat dynamic equilibrium (Figure 4.4). This near edge region shows a continuous change of the Moiré pattern indicating strong structural rearrangements. Different Moiré patterns are observed intermittently indicating distinct commensurate rotation angles between the layers. This is similar to the previously observed superstructures in bilayer graphene. [150]

This highly dynamic nature of the edges can facilitate bond formation leading to a complete material transfer. MD simulations of small flakes heated on the top of the graphitic substrates show that lateral merging is initiated by the bond formation at the edges. Merging starts by the formation of bonds when the flakes get closer. This is flowed by further bond formation (Figure 4.5c) and can lead to a material transfer in the vertical direction.

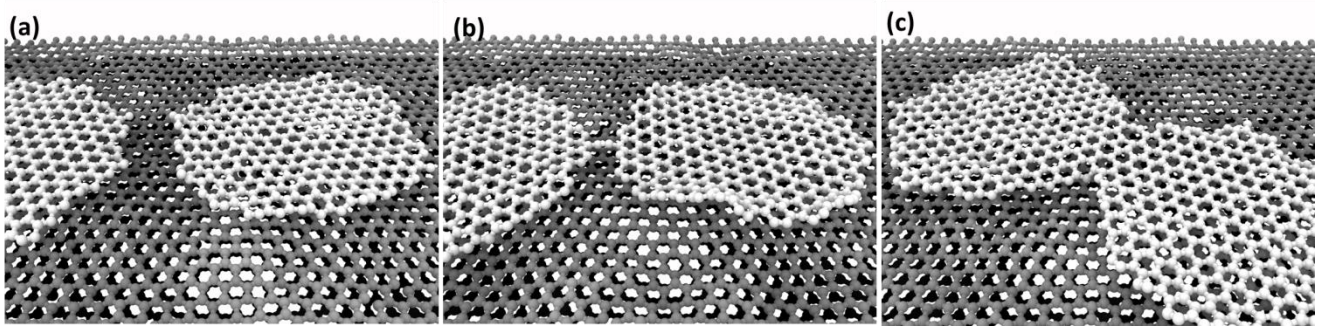

Figure 4.5: MD simulations of the lateral merging event.

The experiments also show that small flakes sitting on top of a step edge of a large layer can merge with the layer underneath. This kind of merging result in a vertical material transfer and the dynamics are slow compared with the fast lateral merging. Figure 4.6 shows such a merging event of a small flake sitting on top of an edge, merging completely with the graphene layer underneath. The uniform Fresnel contrast observed initially, is a good indication that the whole flake is sitting on top of the step edge. The contrast is initially uniform (up to Figure 4.6c), when the bottom edge of the upper flake attaches to the step edge below (Figure 4.6d). Subsequently, the edge of the upper flake slowly disappears as the flake is merging with the edge below. This means that the rearrangement and bonding mechanism is different in this type of

merging. Unlike the fast lateral merging happening in a couple of frames in Figure 4.1, this merging is slow and takes around 5 minutes. In order to merge vertically, there should be an initial bond formation between the reactive flake edge and the step edge below. This can be seen from the MD simulation in Figure 4.6r. Afterwards, this bond has to shift leading to an atom transfer to the step edge below and a new bond has to be formed at the flake edge. Thus, vertical merging requires a coordinated rearrangement at larger scales in contrast to the lateral rearrangements in the previous case. This slows down the vertical rearrangement to a time scale of several minutes, in contrast to the fast lateral merging shown in Figure 4.1.

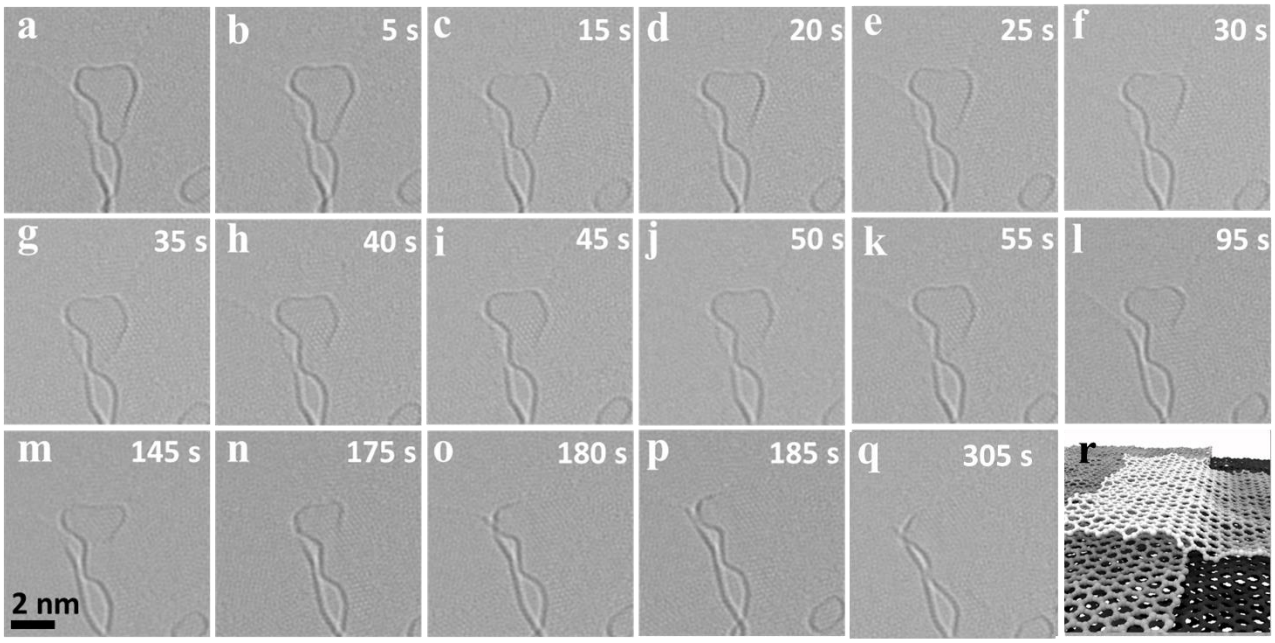

Figure 4.6: (a-l) Slow merging of a nanoflake with an edge in the layer underneath during heating at 1200 °C, the time interval is shown as label in each micrograph.

4.4. Dynamics and size evolution of graphene flakes

In addition to the observed migration and merging, the nanoflakes show strong structural and size fluctuations at high temperatures. Small flakes tend to loose atoms or group of atoms and at the same time larger flakes adjacent to it are seen growing. This is illustrated in Figure 4.7 for ncg heated to 1200 °C. Figure 4.7a shows the overall area investigated and as observed previously, a flake is migrating in to the field of view and merges with an edge. During migration, the small flake is constantly getting smaller, losing atoms, which can be observed from images (b-g). At the same time an adjacent large edge is growing by the

addition of atoms (h-m). This means that there is a simultaneous shrinking of small flakes and growth of large ones. It is to be noted that the shrinking and growth is observed under similar conditions of temperature and illumination. This does not imply that there is a direct material transfer happening from the shrinking small flakes to the growing large flake, but importantly shows the difference in behavior of two flakes under similar imaging conditions.

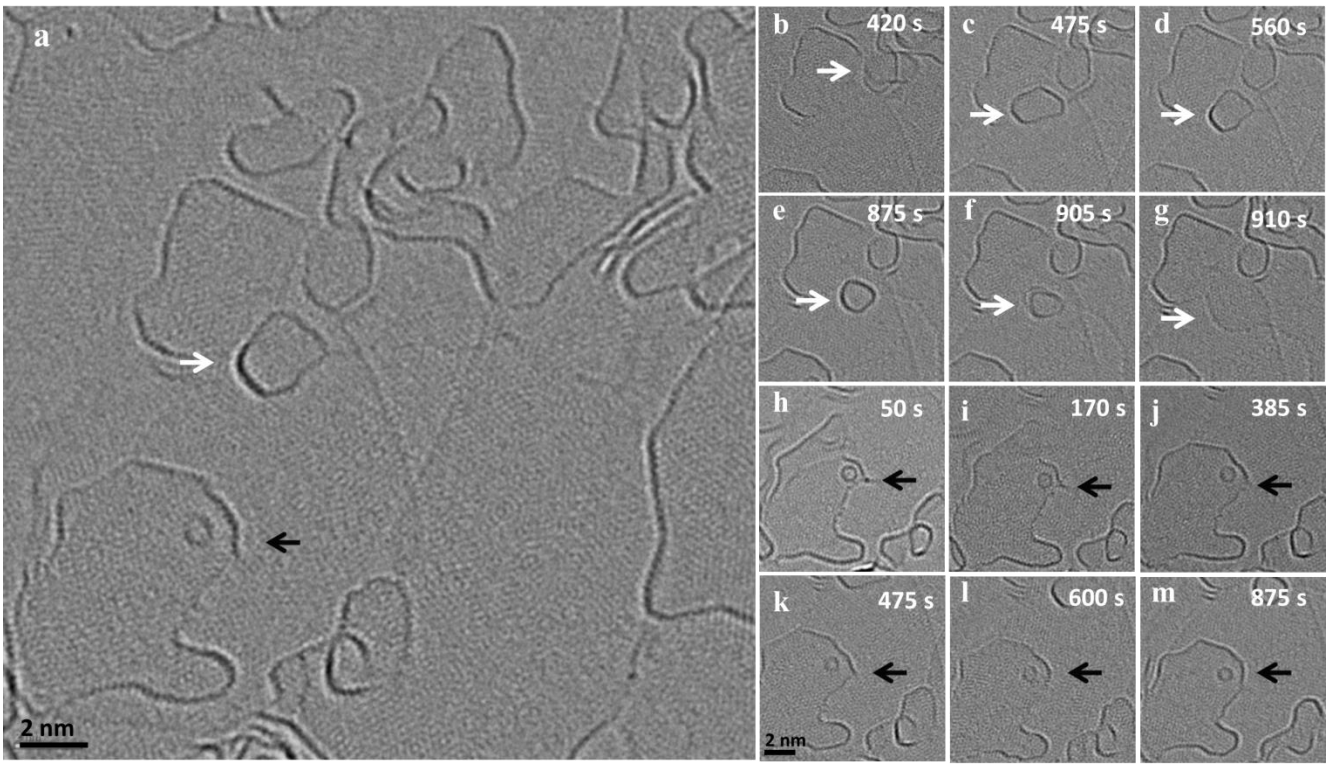

Figure 4.7: HRTEM images of an area in which shrinkage of a migrating flake (indicated by the white arrow, b-g) and growth of a larger flake (indicated by black arrow, h-m) has been observed simultaneously.

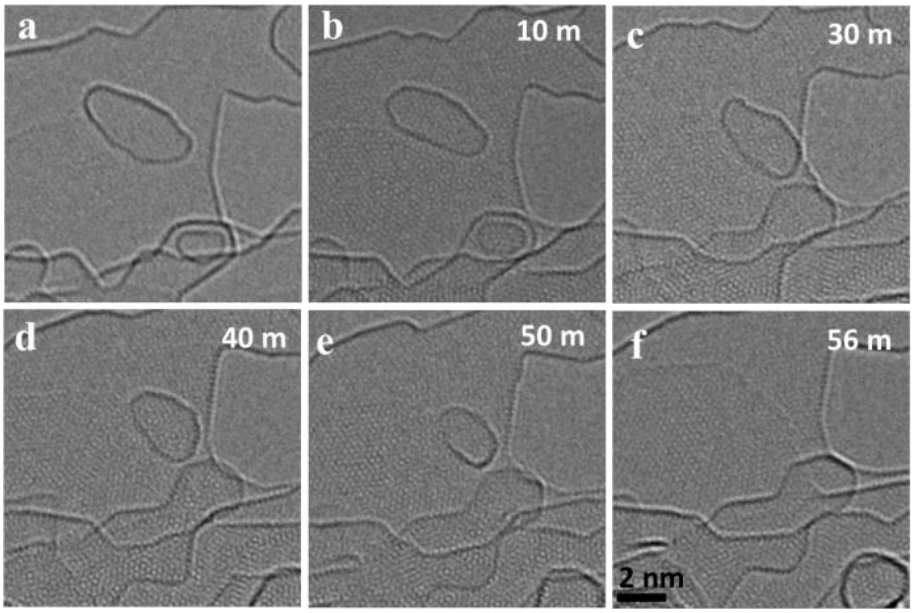

Figure 4.8: (a-f) Shows the dynamics of a small flake heated over a period of 56 minutes at 1200 °C, where images have been taken at 1 minute intervals.

Similar dynamics can be seen in Figure 4.8 where a small flake sitting on top of a layer is migrating to a nearby edge. The dynamics is imaged at 1200 °C at an acquisition rate of 1 frame per minute. This migrating flake is losing atoms at the same time we can observe growth of the adjacent layer. The flake seems to be sitting on top of an edge, which is connecting the shrinking and growing parts. The flake is slowly moving towards the adjacent edge along the edge it is pinned, before it finally disappears from the frame.

Simultaneous shrinkage and growth is also observed in pinned nanostructures that are not moving. Figure 4.9 shows the dynamics of a nanostructure pinned at an edge. This pinned nanostructure is gradually disappearing over a time of 14 minutes. Also in this case, we can observe an adjacent edge which is growing by the addition of atoms. Carefully looking at the edge (marked by black arrow), we can identify an active region which is no longer continuous and seems to open up due to the addition of atoms, similar to the feature highlighted by the black arrow for the growing fragment in Figure 4.7. A high resolution image acquired after the continuous imaging shows a connecting edge between the pinned nanostructure and the growing region in the large flake (Figure 4.9g). All of these examples show that individual atoms or small groups of atoms can detach from an unstable small nanostructure and attach to a nearby stable large flake.

This phenomenon looks similar to an Ostwald-like ripening, where small particles shrink and larger particles grow driven by the higher thermodynamic stability of the larger particles.

This size reduction is observed for structures pinned to defects and edges. There can be an atom transfer to the defects/edges as observed in the vertical merging. Two types of transfer can happen: 1. Transfer of atoms to the defect in the underlaying substrate which heals the defects and 2. Transfer of atoms to an active edge ,where the atom can either migrate along the edge by edge diffusion to another connected flake or can be attached to the same edge extending the edge. This means that the highly active edges can act as a diffusion pathway for the atoms detaching from the flakes. Similarly, an extended defect structure like a line defect or a grain boundary can also act as a possible reactive site for atom transfer and further diffusion.

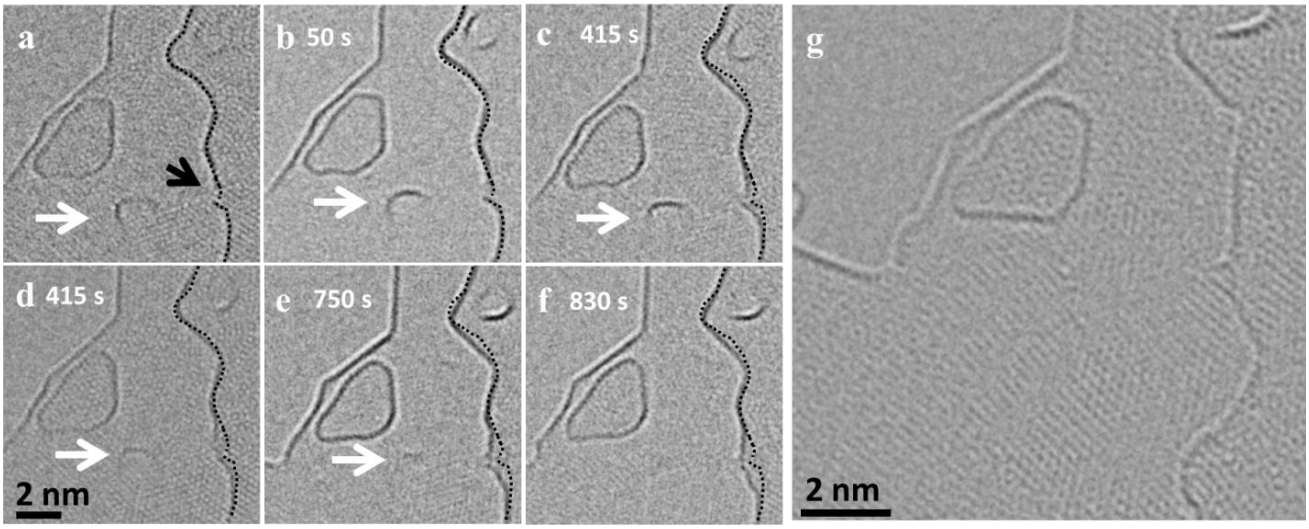

Figure 4.9: (a-f) HRTEM image of a slowly shrinking pinned nanostructure (marked by white arrow) at 900 °C and of an active region (marked by black arrow) in the adjacent layer where atoms are attaching, leading to a growth at the edge. The initial edge profile is overlaid on the following time steps to visualize the growth of the flake. g) HRTEM image taken after the series acquisition, which shows the presence of a connecting edge between the shrinking nanoflake and the growing large flake.

To understand more about the observed size reduction and other structural changes, activation energies associated with these high temperature dynamics were calculated using Nudged elastic band (NEB) calculations. [126] NEB calculations were carried out with the ASE package in conjunction with the semi-empirical solver MOPAC (MOPAC2016, Version: 18.117L), [127] using the PM7 functional. [128] For the

NEB calculations spring constants of $0.01\ \mathrm{eV/\AA^2}$ and a convergence criterion of $f_{max} = 0.1\ \mathrm{eV/\AA}$ were used, the transition states were determined with a climbing image. The visualizations of the changes are created with the OVITO software. [129]

In the case of observed reduction in size, the activation energy required for an atom removal directly from the edge is calculated. The NEB calculation shows high activation energy of 9.17 eV, which is higher than the thermal energy at the experimental condition. Thus, with this high activation, atom removal cannot occur by thermal activation (Figure 4.10a,c). However, when the flake is in close vicinity of reactive sites, such as defects in the substrate or active edges, the activation energy for the atom removal comes down drastically. As an example, NEB calculation of an atom transfer process to a point defect site is calculated (Figure 4.10b).

Here, the atom removal consists of 3 different processes (Figure 4.10d-i).Firstly there is pinning to the initial bound state which has very low energy barrier. This means that the pinning process is mainly limited by the availability of reactive sites. The initial pinning is followed by rearrangement processes lowering the energy. Finally, the depinning process occurs with simultaneous atom removal from the edge. This final process has a barrier of 2.47 eV, which is thermally accessible under the experimental conditions. This barrier will vary depending on the coordination and nature of the reactive site and can temporarily cause stationary nanoflakes. This explains that the point defects can lead to a continuous shrinkage of a mobile flake by losing atoms, saturating the defects along its hopping path. If the reactive site involved in the process is an edge, this can lead to a continuous atom loss, to the edge. Furthermore, the high mobility along edges can enable a continuous atom transfer and diffusion. Similarly, an extended defect structure like a line defect or a grain boundary may also act as a possible reactive site for atom transfer and further diffusion.

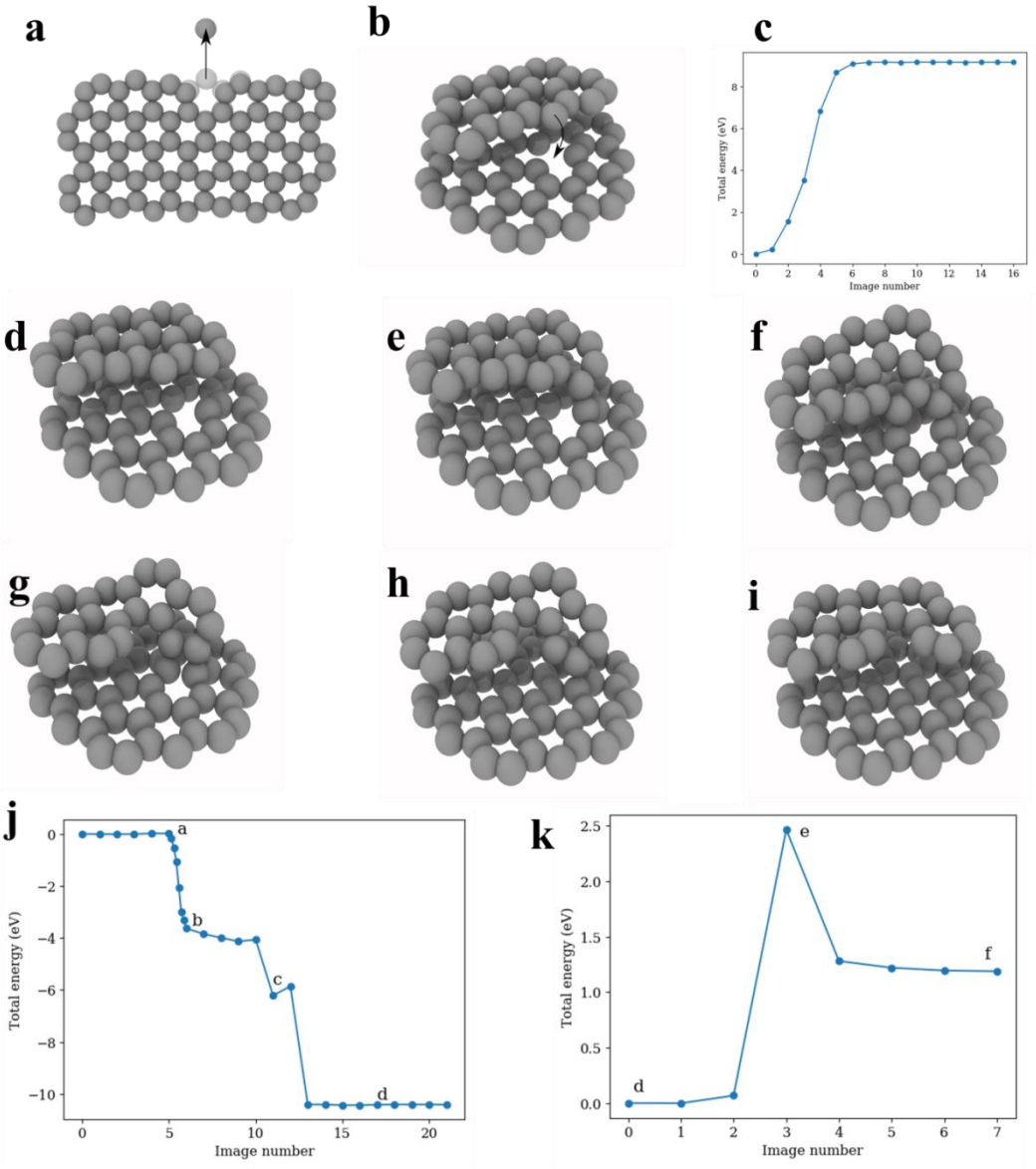

Figure 4.10: Activation energies of atom removal, a) Atom removal from a zig-zag edge b) atom removal to a vacancy, c) energy profile for a direct atom removal showing activation energy, ($\boldsymbol{E_A = 9.17\ eV}$). Intermediate stages of a pinning (d-g) and depinning (g-f) process. (j) energy profile of pinning process ($\boldsymbol{E_A = 0.015\ eV}$). The profile between image number 5 and 6 is recalculated with additional data points. The energies are shifted by the value of the initial state, (k) Energy profile of depinning process with simultaneous atom removal ($\boldsymbol{E_A = 2.47\ eV}$). The lowercase letters refer to the corresponding structures shown in the figure. The energies are shifted by the value of the initial state.

Experimentally, we also observe a continuous change in the edge structure both in small and large flakes during imaging. This means that the edge atoms can diffuse through the edges at high temperatures. Activation energies associated with the edge diffusion were calculated using two example transition which can lead to the observed shape change in the flake. The process rates of two processes, edge diffusion of an ad-atom and the reconstruction of a 6-membered ring to a 5-membered ring are estimated using the Arrhenius law for thermally activated processes which can be written as

$$\nu = \nu_0 \, e^{-\left[{E_A}/{k_B T}\right]} \tag{4.1}$$

The prefactor ν_0, which corresponds to a trial rate, can be estimated by the typical frequency of in-plane and out-of-plane optical phonon frequencies of graphene ($\approx 0.45 \cdot 10^{12}$ Hz). [151]

Using the above equation, activation energies for the edge diffusion process and for the ring reconstruction process obtained are 0.58 eV and 1.76 eV respectively (Figure 4.11). This results in process rates on the order of 10^9 and 10^5 Hz respectively at 1200 °C. This confirms that the observed shape change which is a result of edge diffusion and edge reconstruction can be thermally activated without the presence of beam. It is also worth to note that the frequency of these reactions is so high, so that it will not be able to image a single defined state of the edge structure in the high-temperature *in situ* TEM experiments.

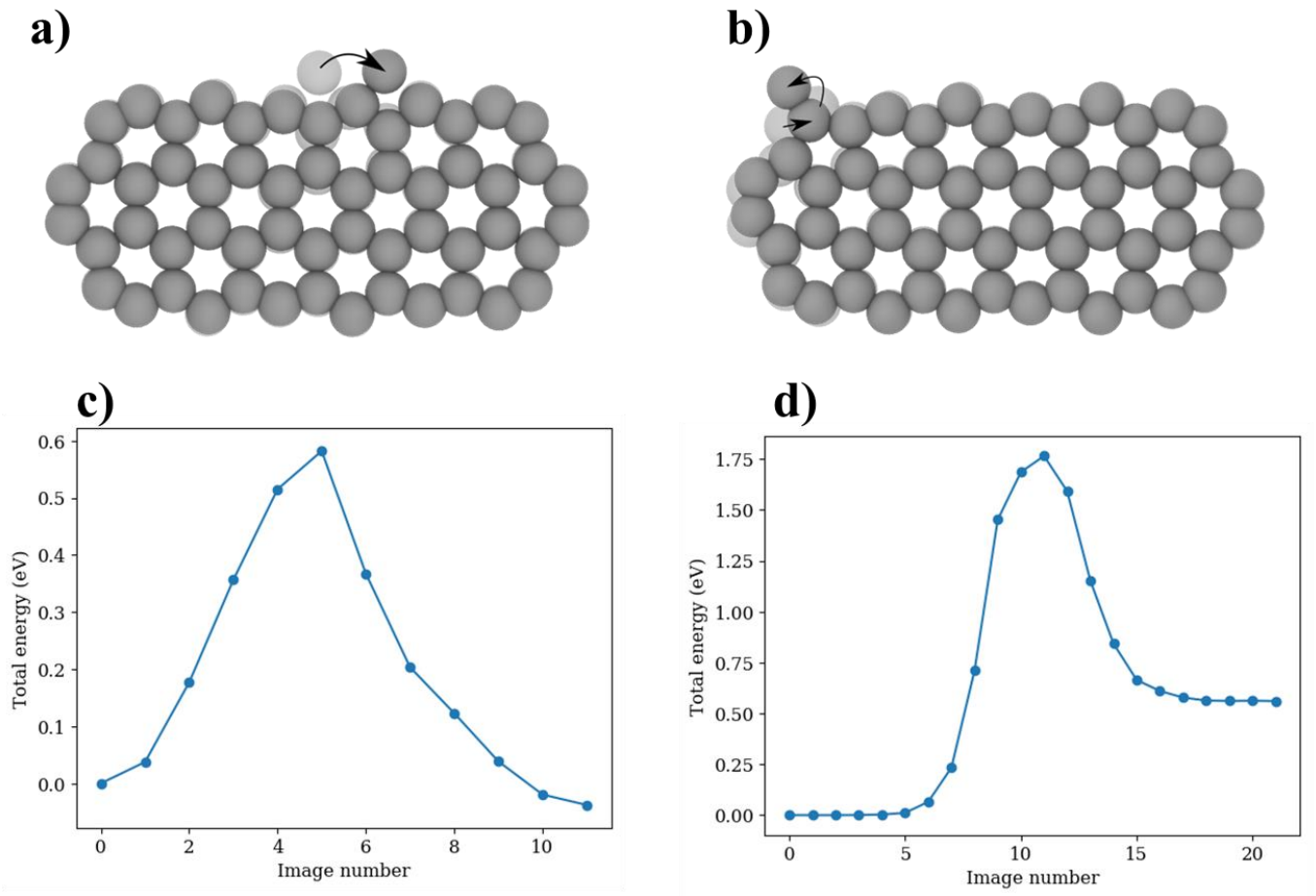

Figure 4.11: NEB determined activation energies for different processes, a) edge diffusion of an ad-atom ($\boldsymbol{E_A = 0.58\ eV}$), b) 6- to 5-membered ring reconstruction ($\boldsymbol{E_A = 1.76\ eV}$), c) energy profile of edge diffusion process, d) energy profile of edge reconstruction. The energies are shifted by the value of the initial state.

The experiments and simulation studies clearly show the role of defects on the observed dynamics. This can be further observed on the behavior of the carbon nanostructures (Figure 4.12). Here, two similar sized GNF behave differently when observed under the same temperature and illumination. The isolated flake (marked by red arrow) is stable with negligible or no mass loss whereas the flake near the edge (marked by blue arrow) loses atoms quickly before it migrates out of the field of view. The flake near the edges have higher amount of nearby reactive sites which increases the material transfer rate.

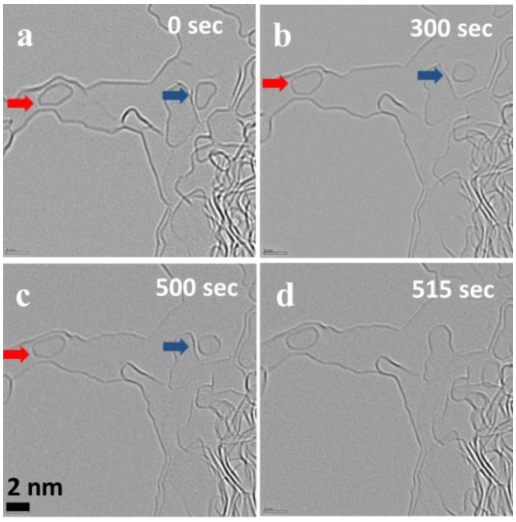

Figure 4.12: BF-TEM images showing the different behavior of two flakes at the same temperature and illumination conditions. The flake marked by a red arrow is stable with minimum mass loss while the one indicated in blue is losing atoms quickly before it migrates out of the field of view.

Also it is to be noted that Ostwald like ripening is observed only when there is a significant difference in the size of the flakes. In the experiments when two similar sized GNF comes closer, they typically merge directly, whereas we have never observed transfer of atoms between them (Figure 4.13).

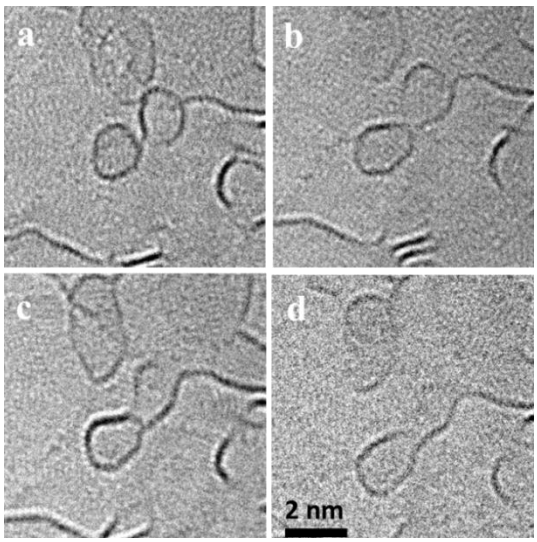

Figure 4.13: HRTEM images showing merging of two small, similar sized nanoflakes during heating at 900 °C.

4.5. Effect of the electron beam

To completely understand these observed dynamics, it is important to consider the influence of the electron beam on the processes. The electron beam is known to induce structural changes and transformations in graphene and carbon nano structures. A number of studies have shown the effect of the electron beam on the behavior of carbon nanostructures on the top of graphitic substrate. [79,113,143] Also, the electron beam has been used as a tool to modify graphene and other carbon nanostructures. [114,152–154] This suggests that the beam can have significant effects for the observed dynamics. The beam can directly affect it in two ways: sputtering of atoms and radiolysis, i.e. ionization due to inelastic scattering, resulting in a transition of an electron from a bonding to an antibonding state. This lowers the activation energy for bond rearrangements or breakage. [101] The threshold for knock on damage in defect free graphene is just above 80 kV. [102]However, the threshold is only around 50 kV for edges and defects. [15]As the structure of ncg is highly defective, the 80 kV beam used in the present study can have significant effects in the observed dynamics. At even lower voltage, the inelastic scattering cross-section is increasing significantly, thus resulting in stronger radiolysis effects for the growth processes.

TEM column can act as a source for carbon atoms by the dissociation of hydrocarbon impurity inside the TEM. These ad-atoms are highly mobile on the top of the graphitic substrate and can attach to the edges, extending the edges. High amount of ad-atoms have been observed previously during *in situ* heating of graphene in TEM which can attach and heal vacancies/nanopores at high temperatures. [114] Present heating experiments also show large amount of ad-atoms. This can be seen from the filling of a hole of ~2 nm diameter in less than a minute while heating at 1200 C (Figure 4.14).

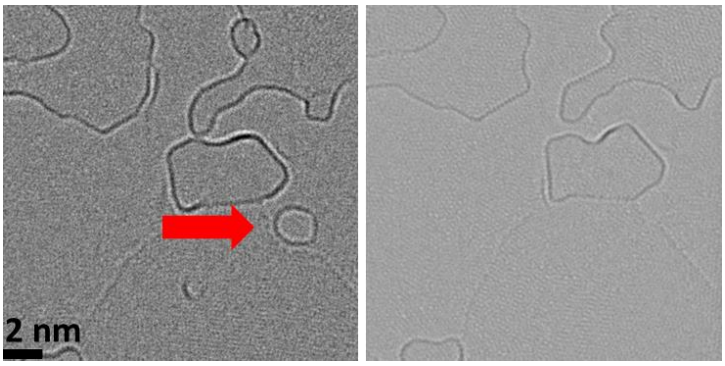

Figure 4.14: HRTEM images showing the filling of hole during heating at 1200 °C.

Another beam induced effect that can contribute to the reactions is the activation of oxygen, hydrogen and metallic impurities in the column by the electron beam. These reactions can form active elements which can react with the graphene edges resulting in etching. The effect of etching on the edge structure of graphene is a well-studied field. There are reports on etching by hydrogen during CVD growth of graphene. [155] The study shows that the increase in hydrogen flow results in a reduction of the flake size by etching by atomic hydrogen. Atomic hydrogen is formed by the catalytic dissociation of hydrogen by platinum. The electron beam can also dissociate oxygen, hydrogen and water present inside TEM column, which would lead to etching of the graphene edges. [101] This clearly indicates the importance to separate the inherent temperature driven mechanism and the beam induced transformations. For this, beam off heating experiments were conducted, which largely reduce the beam exposure. This is done by imaging a particular area during heating, switching off the beam for extended time of 20-30 min. and acquiring an image of the same area after this time interval.

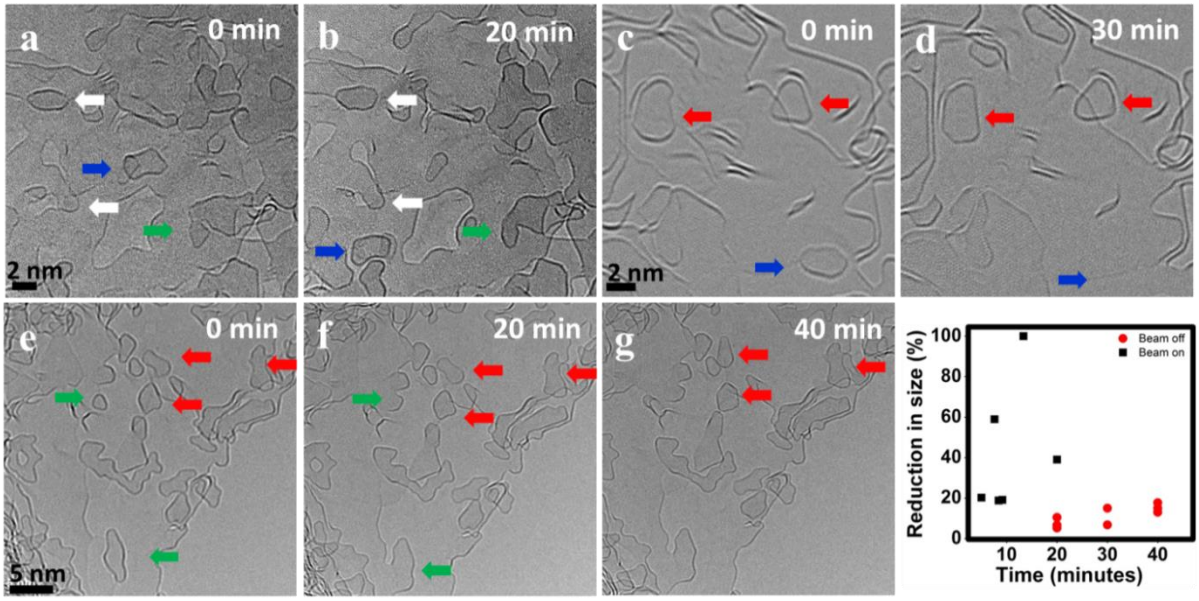

Figure 4.15: BF-TEM images of the same region before and after 20 minutes of heating at 900 °C (a,b) and (c-g) at 1200 °C. The graph shows the percentage of reduction in size of selected graphene flakes during heating with the electron beam on (black) and off (red).

Figure 4.15 shows three beam off heating experiments where the beam is turned off completely between the image acquisitions for 20 or 30 min. In the first set of images (Figure 4.15a,b), the flake indicated by the

blue arrow migrated from its initial position. Similarly, the flake in Figure 4.15c and d, indicated by a blue arrow, migrated out of the field of view. This flake might have merged with some edge below or might have migrated from the region. In any case, these images show that migration can happen without the electron beam and this is an inherent temperature driven process. Similarly, merging of domains (flakes marked by green arrows) is also observed during heating without the electron beam.

Apart from the observed migration and merging during beam off heating, the experiments show clear evidence for the shrinkage and growth of the flakes. Flakes marked by red arrows in Figure 4.15 exhibits a change in shape and reduction in size. The ones marked by white arrows show an increase in size. This shows that the size dynamics observed during continuous imaging also occurs without the electron beam, indicating that these are inherent temperature driven processes, not just beam induced. It is worth to note the presence of edges in the beam of experiments as in the case of continuous exposure. The flakes showing size reductions are sitting either on or nearby an edge. This suggests that a similar mechanism as suggested for the continuous exposure will be operating without the electron beam. The increase in size can be due to addition of atoms or by merging with a mobile flake. During beam off heating, with the long acquisition interval, it is difficult to identify the active regions in a growing flake and to differentiate between merging and addition of atoms.

With these beam off experiments, it is clear that the observed processes are inherent temperature driven. However, comparing the decrease in size with the electron beam on and without the electron beam during heating, it can be observed that the beam is significantly accelerating the dynamics. The graph in Figure 4.15 shows a comparison of the reduction in flake size without the electron beam and during continuous exposure. Without the electron beam, the flakes show a significantly lower reduction in size compare to with the electron beam on. This indicates that the beam is providing noticeable activation energy, thereby accelerating the dynamics. Beam induced sputtering of atoms at the edges of the graphene flakes can increase the dynamics. However, probably more important, the inelastic interaction with the electron beam leaves the graphene flakes in an excited state thus lowering the activation energy for further reactions.

To further understand the effect of temperature, the samples were exposed continuously for 10 minutes at room temperature. Figure 4.16 shows the images of the room temperature exposure studies. The exposure resulted in an expansion of a pre-existing hole and the creation of a new hole (indicated by red arrows). The

nanostructures (indicated by blue arrow) remained stable under the beam without any size/shape changes and migration, which shows that the electron beam by itself is not very efficient in inducing the observed migration and merging.

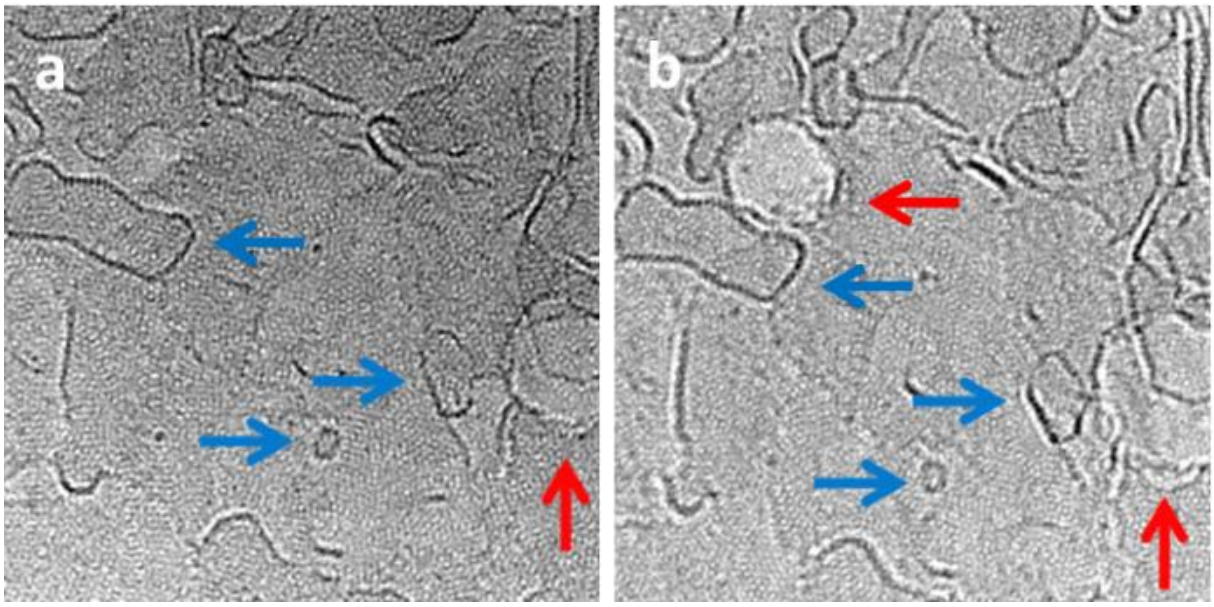

Figure 4.16: BF-TEM images at room temperature before (a) and after (b) continuous exposure for 10 minutes at a dose of and 4.1 x 108 e/nm^2 s.

This experimental and simulation studies confirm that the observed dynamics are inherently temperature driven and not beam induced. We observe selective shrinking of small flakes with respect to the large ones under the same condition of temperature and illumination. This can be explained by the edge structure, local curvature of the edges [155] and the higher energy per atom. [156] Effect of these factors on the stability of nanoflakes is well established in the literature and results in higher probability to lose atoms for a small nanoflake compared to larger flakes. Steered molecular dynamics (SMD) simulations are used to understand this which shows the effect of local curvature on the atom displacement from an edge (Figure 4.17). The simulations are carried out for a knock out event occurring due to a momentum transfer corresponding to 16 ev. This energy corresponds to the energy transfer from an 80 kV electron beam. [157] The momentum is set on the first time step parallel to the flake plane in vertical direction and with deviations ±18° and ±27°. According to the simulations, the corner/near corner atoms have a higher chance to escape compared to the flat and concave edges. This means that the nanoflakes with more convex edge curvature and consisting of

more corner/near corner atoms will have more probability for an atom escape than a flat or concave edge in the large flake. These experimental and simulation studies clearly show that highly defective graphene systems can show inherent temperature-driven Ostwald-like ripening even in the absence of electron irradiation.

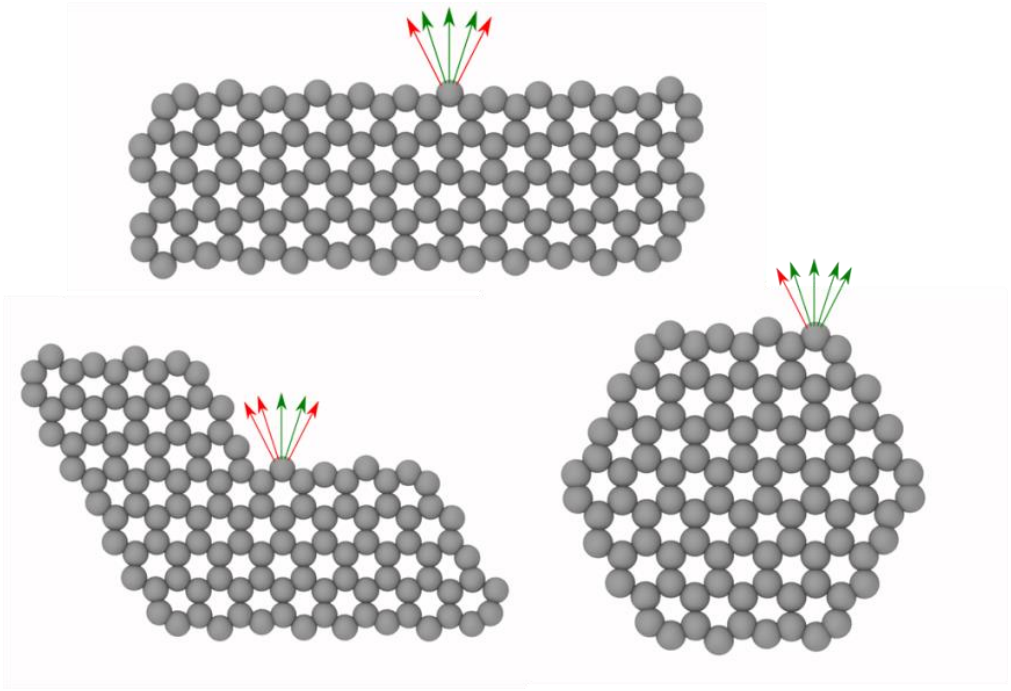

Figure 4.17: SMD simulations of knock-out events at different angles of momentum transfer (corresponding to a kinetic energy of 16 eV). Green arrows: successful atom escape, red arrows: unsuccessful atom escape.

4.6. Conclusion

The results show that the high-temperature behavior of the nanocrystalline graphene is different from pristine graphene. The high density of defects, carbon nanostructures and active edges greatly influences the dynamics and reactions of the carbon nanostructures and the growth of domains. High temperature *in situ* HRTEM investigations revealed the formation of different carbon nano-structures with varying size, shape and dynamics. The dynamics and interaction of these structures with the graphitic substrate show that the high temperature growth of ncg proceeds mainly by migration and merging of graphitic subunits. *In situ* experiments along with MD simulations reveal that unlike the observed high diffusion of nano-structures on defect-free graphene, in ncg migration is hindered by pinning to defect sites in the substrate. The flakes

can merge both laterally and with the underlying layers facilitating both lateral and vertical mass transfer. In addition to this, at high temperature, pinned graphene nano-flakes are highly unstable and tend to lose atoms or groups of atoms, while adjacent larger flakes grow by the addition of atoms, indicating an Ostwald type of ripening in these 2D materials as an additional growth mechanism. Experiments without the electron beam, supported by molecular dynamic simulations, confirm that these processes are direct temperature driven processes, whereas the beam is providing extra activation energy changing the reaction kinetics.

Two different mechanisms of growth are observed here, one by the migration and merging of domains and the other is the growth of large structures by the dissolution of small ones. These growth mechanisms are similar to the two well-known growth mechanisms for nanoparticle growth: Smoluchowski ripening [158,159] and Ostwald ripening. [160] The migration and merging of nanoflakes are already observed and reported in different studies. The dynamics of carbon nanoflakes/nanostructures on top of graphitic substrates are also observed inside the TEM. [64,65,161]. But there are no reported studies on the Ostwald like ripening in these 2D materials. The main reason for this is the high mobility of carbon nanostructures on top of defect-free graphitic substrates, which makes migration and merging favorable. The domains migrate and merge when the mobility is high and the dominating growth mechanism will be the migration and merging. But in the case of nanocrystalline graphene, the high defect density will hinder the migration and when the flakes are pinned, atoms or group of atoms can detach from the flake resulting in an Ostwald like ripening in these 2D materials. This is also supported by the molecular dynamic simulation studies which shows a reduction in the activation energy for atom removal when the flake is in proximity with the defects.

Apart from providing significant insights in to the high temperature dynamics of ncg, stability/mobility of nanostructure and the fundamental growth mechanisms of graphene, the present results provide a detailed understanding of the pyrolysis of polymers leading to the formation of bulk graphitizing and non-graphitizing carbons. It is important to note that the merging of domains can be both lateral and vertical. This will be more prominent in the graphitization of bulk samples. This different material transfer shows that not only the oriented domains can merge laterally but also the misoriented domains can grow by vertical merging, but at a much slower speed. This kind of vertical merging is important in graphitizing carbons, which might contribute to complete graphitization at very high temperatures. With the highly defective structure in bulk glassy carbons, apart from the merging of domains, Ostwald-like ripening can also be a

contributing growth mechanism. As the thickness increases, there are more defects and also a higher number of diffusion pathways in different orientations. This can increase the possibility for atom transfer between differently oriented inter-connected domains. These results open up new possibility to understand the graphitizing and non-graphitizing nature of carbons.

The results can also help to understand the the structure of bulk glassy carbon more in detail. *In situ* graphitzation and growth shows that flakes contain reactive edges on different side and the growth is not limited in one direction. The proposed ribbon like model, [49,50] which predicts more length compared to the thickness and width is not observed in the present study. The structure contains more flat flakes with reactive open edges growing in all directions. This is clearly in contrast with the fullerene like model which predicts closed edges and curved graphitic sheets. [53] With the observed results, the structure looks more close to the structure proposed by Franklin *et al.* and Oberlin *et al.*, [41,46] which predicts the presence of basic structural units of small groups of planar molecules. These crystallites grow laterally by the addition of amorphous carbon and by the merging of domains. The vertical growth is by ordering of domains at higher temperature. However, as proposed by the models, the crystallites are not flat but can be curved/twisted due to the presence of non-six membered rings.

5. Current annealing of ncg films

5.1. Introduction

The *in situ* studies on graphitization and high temperature dynamics of ncg helped to understand the structural evolution and the fundamental processes controlling the growth of ncg. The conventional pyrolysis process to produce bulk graphitizing carbon is carried out at ultra-high temperatures of up to 3000 ºC. [43,46,47,50,59] To gain a complete understanding of the pyrolysis process, these temperatures have to be reached and the structural changes occurring during these later stages of pyrolysis have to be understood. However, the maximum temperature that can be reached by the commercially available Aduro heating chips is 1200 ºC. The main limitation for this is a lack of suitable support & resistive materials sustaining these ultra-high temperatures.

A possible alternative is to heat the sample itself by resistive current heating. With current annealing confined heating to reach ultra-high temperatures becomes feasible. Previous studies on current annealing of graphene inside the TEM showed the possibility of reaching ultra-high temperatures. [64,65] However, there are only limited studies on the current annealing of amorphous carbon and all of them are carried out on thick samples and carbon fibers. [68–70] In ncg, studies predict the formation of polycrystalline graphene when heated to very high temperatures. [35] This can possibly be achieved by current annealing which results in the growth of nanocrystalline domains forming polycrystalline graphene. Furthermore, the evolution of resistance can be correlated with the structural changes. Thus current annealing opens up the possibility to tailor the structure and resistance of these films over a wide range of temperatures. In this chapter, ncg films pre-graphitized at 800 ºC is further current annealed inside the TEM to understand the structural changes happening at ultra-high temperatures.

5.2. Device fabrication

Electro contacting chip from Protochips were used for the *in situ* current annealing of ncg. To grow and pattern the ncg on the top of the chip, electrodes of the chip were removed by etching with aqua regia solution for four hours. The chips were cleaned with acetone and then cleaned with oxygen plasma for two minutes. The chip was spin coated with S1805 photoresist with a solution ratio 1:16. The solution ratio of 1:16 was used to get a final film thickness of 2 nm. The chip was graphitized inside a vacuum oven at 800

ºC for 2 hours. The electrodes were removed because of two reasons. First, the electrode thickness will affect the spin coating of polymers and is difficult to get a uniform thin layer when the electrodes are on the top of the chip. Second, the electrodes can be destroyed during the graphitization at 800 ºC. Ncg constrictions were patterned on top of the free-standing SiN membrane. After patterning the constrictions, tungsten electrodes were deposited using electron beam lithography. For electron beam lithography, the chip was spin coated with PMMA to make a film of 250 nm thickness. The chip was then baked at 150 ºC for 3 min. The PMMA layer was exposed to the electron beam for the required shape. The exposed areas were developed using MBIK/IPA solutions. 15 nm aluminum was then evaporated onto the sample. The sample was immersed in acetone to remove the PMMA and the aluminum in the unexposed regions. Reactive ion etching was used to remove the ncg from the unexposed region while the region of interest were protected by Al. Aluminum was removed by etching with commercially available AZ 726 MIF (Merck inc.) for 30 s. To make contact electrodes, the sample is coated again with PMMA and the required area is developed. Tungsten is evaporated on the sample to make the contact electrodes. The unexposed PMMA and tungsten is removed by acetone.

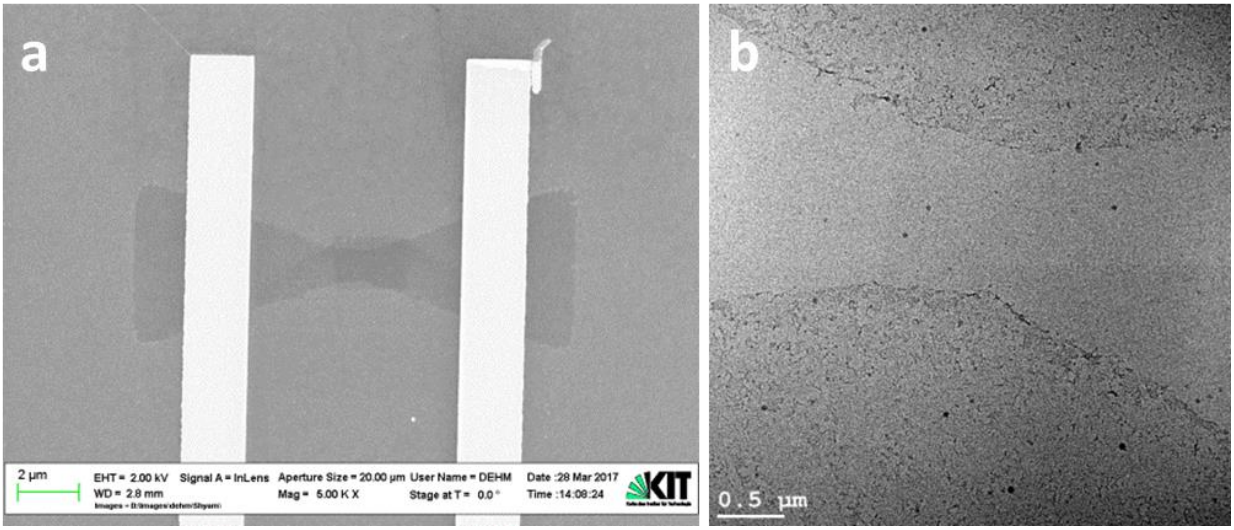

Figure 5.1: (a) SEM and (b) TEM image of the patterned ncg on the free-standing SiN membrane.

Figure 5.1 shows the SEM image of the patterned ncg constrictions. A rectangular region of 2 micron in length and 0.5 micron in width is connected to the electrodes by two triangular regions. This shape of the constriction is based on the reported previous studies, where the constricted region will exhibit a higher

resistance compared to the wider triangular regions and the electrode ncg junctions. [11] This constrains the heating to the rectangular strip and can be easily followed inside the microscope.

5.3. *In situ* current annealing of substrate supported ncg

The patterned ncg on top of the SiN free-standing membrane is current annealed inside the TEM by loading it in the Aduro holder from Protochips. The main problem encountered during the *in situ* current annealing was the crystallization of the amorphous SiN membrane. As the temperature increased, the amorphous membrane underneath the construction heats up and started crystallizing. This transformation results in a volume change and induces strain in the free-standing film eventually breaking the SiN film. This destroys the patterned ncg on top, limiting further current annealing.

This can be observed in Figure 5.2, were the constriction is current annealed inside TEM. Initially the heating produces small holes in the membrane due to sublimation of SiN (Figure 5.2a-c) and suddenly the membrane crystalizes and beaks, destroying the patterned ncg. The rapid extension of the crystallized region can be observed in the images (d to f). High resolution image of ncg can be observed on the top of crystallized SiN (g) and at the edge (h). The SAED pattern from the transformed region in (i) shows highly crystalline SiN. This amorphous to crystalline transformation can be a used to roughly estimate the maximum temperature reached by the current annealing. The amorphous to crystalline transition is reported to start at temperatures above 1400 ºC, which means that the temperature reached here is noticeably higher than the maximum temperature in the Aduro heating chip. [162] However, the presence of the thick SiN membrane during the initial stages and the breaking of the membrane prevented imaging the structural changes during heating.

Bright field TEM images from a broken region are given in Figure 5.3. Figure 5.3a. shows the broken SiN membrane and b shows the TEM image of the ncg at the broken region. Large flakes with sizes of ~10 nm are visible on top of large area graphene. The structure looks more crystalized than the structures observed previously during *in situ* heating. The SAED pattern shows discrete rings indicating an improved crystallinity. But with these substrate effects, it is difficult to see the structural changes occurring during the current annealing. To image the structural changes early, we modified the sample preparation procedure to prepare free-standing ncg samples for current annealing.

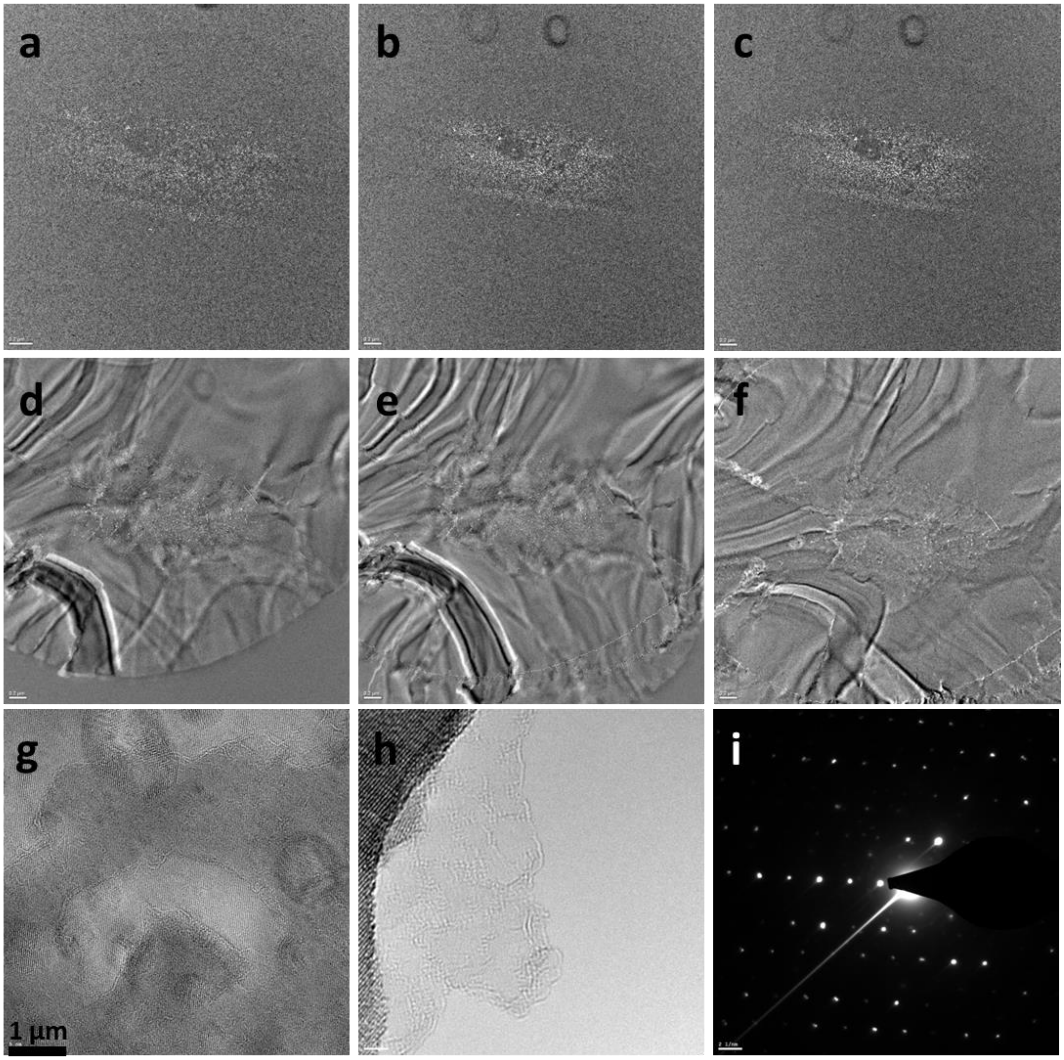

Figure 5.2: (a-c) Formation of holes in the SiN membrane during heating, (d-f) crystallization of the SiN membrane. Ncg film on the crystallized (g) and broken edge (h) of the SiN membrane. (i) The SAED pattern of crystallized SiN membrane.

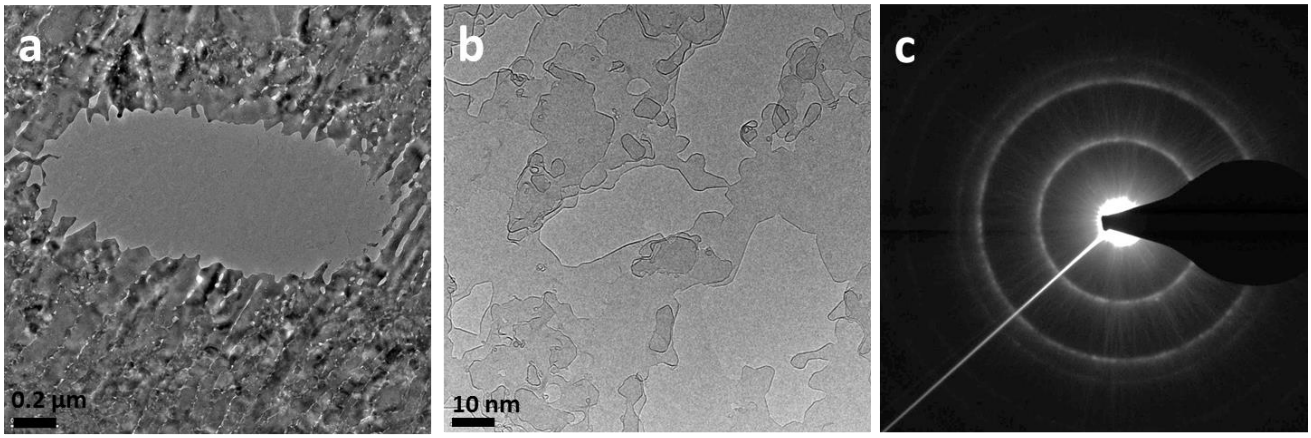

Figure 5.3: (a) Broken SiN membrane, (b) graphitized film at the broken region and (c) discrete ring pattern in the SAED showing high crystalline nature of the transformed film.

5.4. Free-standing sample preparation for current annealing

To get a free-standing film, rectangular holes were drilled between the electrodes in the SiN membrane using focus ion beam milling (Figure 5.4a). Large area thin films *ex situ* graphitized on a Si-SiO_2 membrane were etched and transferred to the Aduro chips. To transfer the ncg grown on the Si-SiO_2, the films were coated with PMMA using spin coating and the etching is carried out using 5 % NaOH solution at 70 ºC. The stack consisting of 300 nm PMMA and ncg film is floated and cleaned thoroughly by subsequent transfer to pure water. The cleaned stack is fished on to the Aduro chip and the PMMA was dissolved by dipping it in acetone for 4 hours. The clean thin films were patterned using electron beam lithography to form free-standing films across the electrodes (Figure 5.4c).

For patterning the free-standing films, a negative electron beam resist was used to reduce the processing steps, particularly the lift of using Al. While developing the negative resist, the solubility of the exposed area reduces. This means that the exposed resist will remain on the sample after developing them. Commercially available negative resist MaN 2403 was used for the lithography. A 300 nm film is formed on the top of the chip, baked at 90 ºC for 1 min and the required shape is exposed inside an SEM at 30kV. The exposed film was developed using commercially available AZ 726 MIF (Merck inc.) for 30 s. Ncg at other places was removed using RIE and the protective polymer layer was finally removed by dipping in acetone.

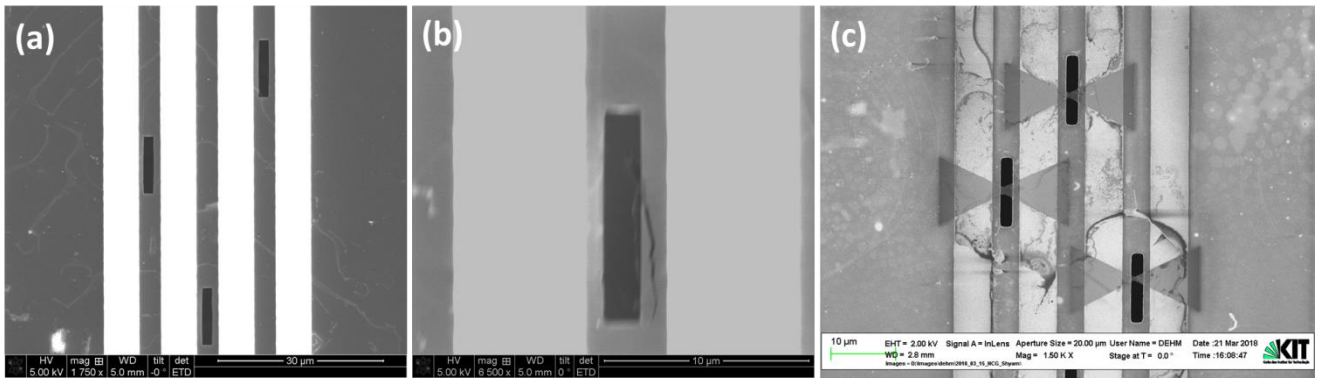

Figure 5.4: (a) Drilled holes between the electrodes of the electrical chip, (d) transferred ncg film across the holes and (c) lithographically patterned ncg constrictions across the holes.

5.5. Structural evolution during *in situ* current annealing

The free-standing lithographically patterned film shown in Figure 5.4 was current annealed inside the TEM. The structural evolution during current annealing of the free-standing film is shown in Figure 5.5. The initial structure consists of a lot of amorphous residues from the lithography procedure. These residues transform during the current annealing of the graphitized film. This transformation gives insights in to the structural changes during current annealing. It can be seen from the images that the evolution of the domains look similar to the evolution during thermal annealing. Evolution from a curved and wrinkled structure to an ordered structure and the subsequent growth of the domains can be seen in the images. On further heating, the edge of the hole in the silicon nitride membrane started crystallizing and resulted in cracking which prevented further heating of the film (Figure 5.5g, h).

Figure 5.6 shows the intensity profiles of the SAED patterns during the current annealing. As the current increases, the width of the intensity profiles comes down indicating an increase in the crystallite size. The crystallite size calculated from the SAED patterns using Scherer formula increases from 2.6 nm at 100 µA to 3.6 at 500 µA. This crystallite size is similar to the crystallite size calculated for the film thermal annealed to 1200 ºC. This means that the ncg constriction has already reached high temperatures and the structural evolution is comparable with the thermal annealing.

Graph (Figure 5.5h) shows the evolution of resistance during current annealing. The ncg film initially showed a very high resistance of the order of 10^7 ohm, which decreases 4 orders of magnitude during current annealing.

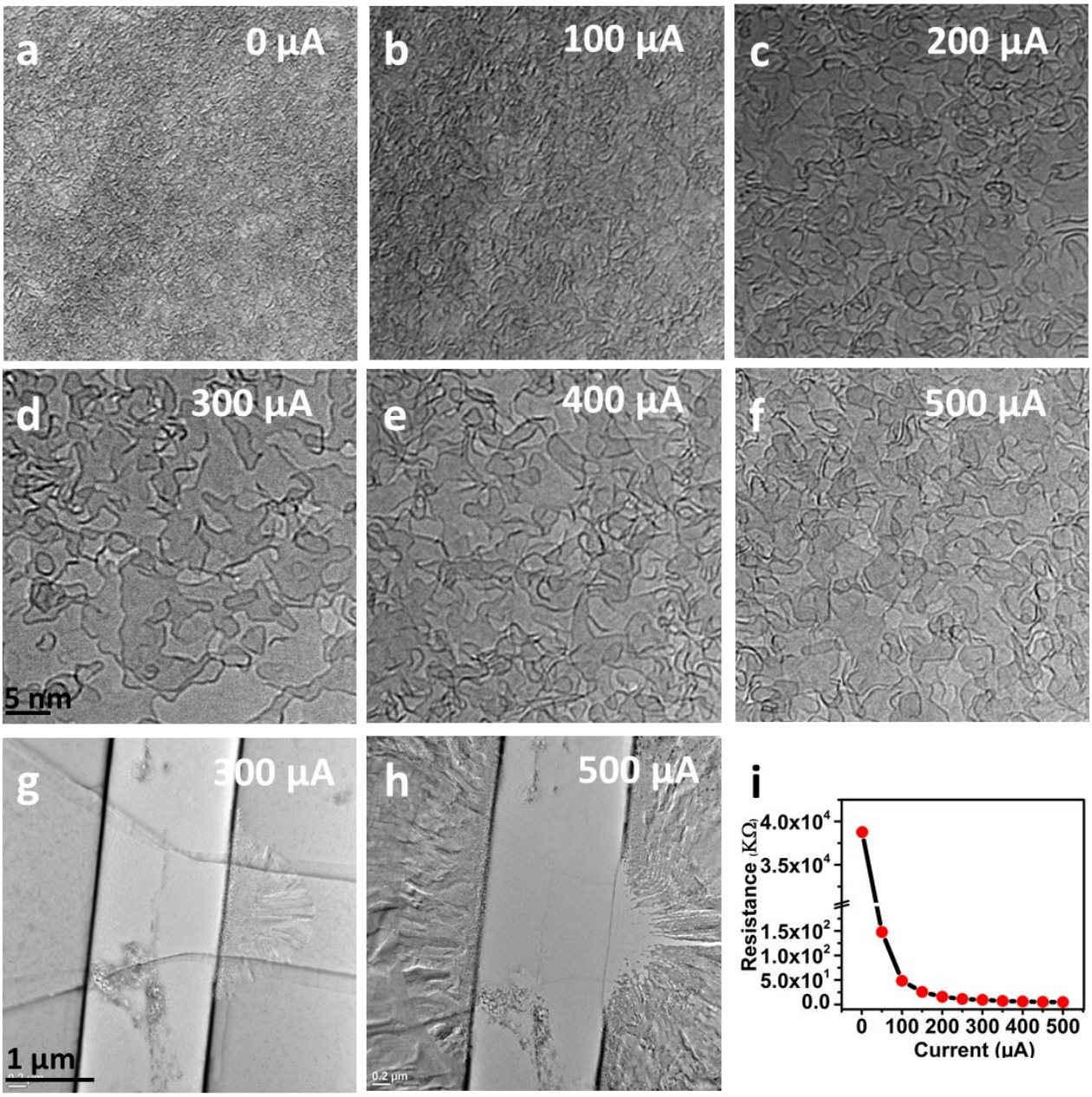

Figure 5.5: (a-f) Evolution of domains during current annealing, (g, h) crystallization of the SiN membrane near the edge and (c) evolution of resistance during current annealing.

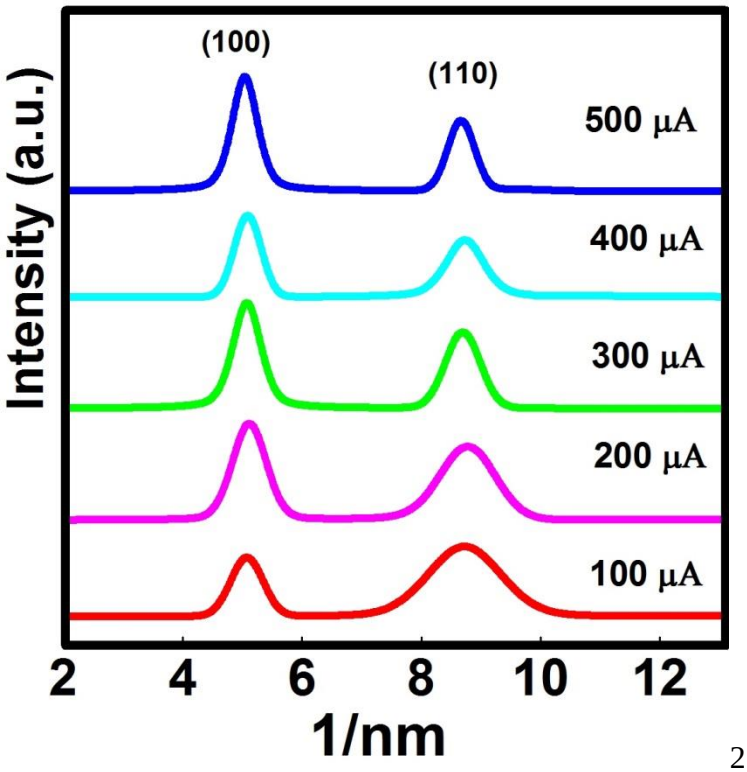

Figure 5.6: Intensity profiles of the diffraction pattern at different temperature.

These results show that after the initial carbonization, further graphitization of ncg can be carried out by current annealing. The flexibility of direct growth in different substrates, the possibility to control the thickness/shape and the comparable structural evolution during current annealing can provide new possibilities to tailor the structure and conductivity of ncg for different applications.

To further increase the temperature and to study the structural evolution at ultra-high temperatures, structures were carefully patterned to confine the heating and structural changes only to the free-standing area. This helped to reach higher temperatures but the sample broke in between. The early breaking can be because of the variation in thickness or the presence of cracks which results in sudden heating leading to an early breakage. Figure 5.7 shows the broken thin ncg film after current annealing. The structure shows the presence of distributed domains on the top of thin layer ncg. These distributed domains can be from the catalyst free transformation of the amorphous residues from the electron beam lithography process. Unlike observed in the early stages of pyrolysis, the domains are large and show defined shapes, e.g. seen in Figure 5.7. Figure 5.7e shows a large thin film area without any domains on the top of it. The FFT from an area of

around 20 nm^2 shows only two sets of hexagonal spots. This can be a twisted bilayer region or a single layer containing two differently oriented crystals. The size of the domains show that the structure has grown considerably from the measured maximum crystallite size of 3.2 nm reached by thermal annealing. Also it should be noted that FFT in images c, d and e shows only one ring corresponding to (100) plane in carbon. This corresponds to an in plane growth in these thin films. But while looking at more stacked region, (Figure 5.7f), the FFT shows a diffuse ring corresponding to the (002) plane. This shows some vertical stacking and deviation from an in plane ordered structure. This points towards thickness dependence in the ordering of domains.

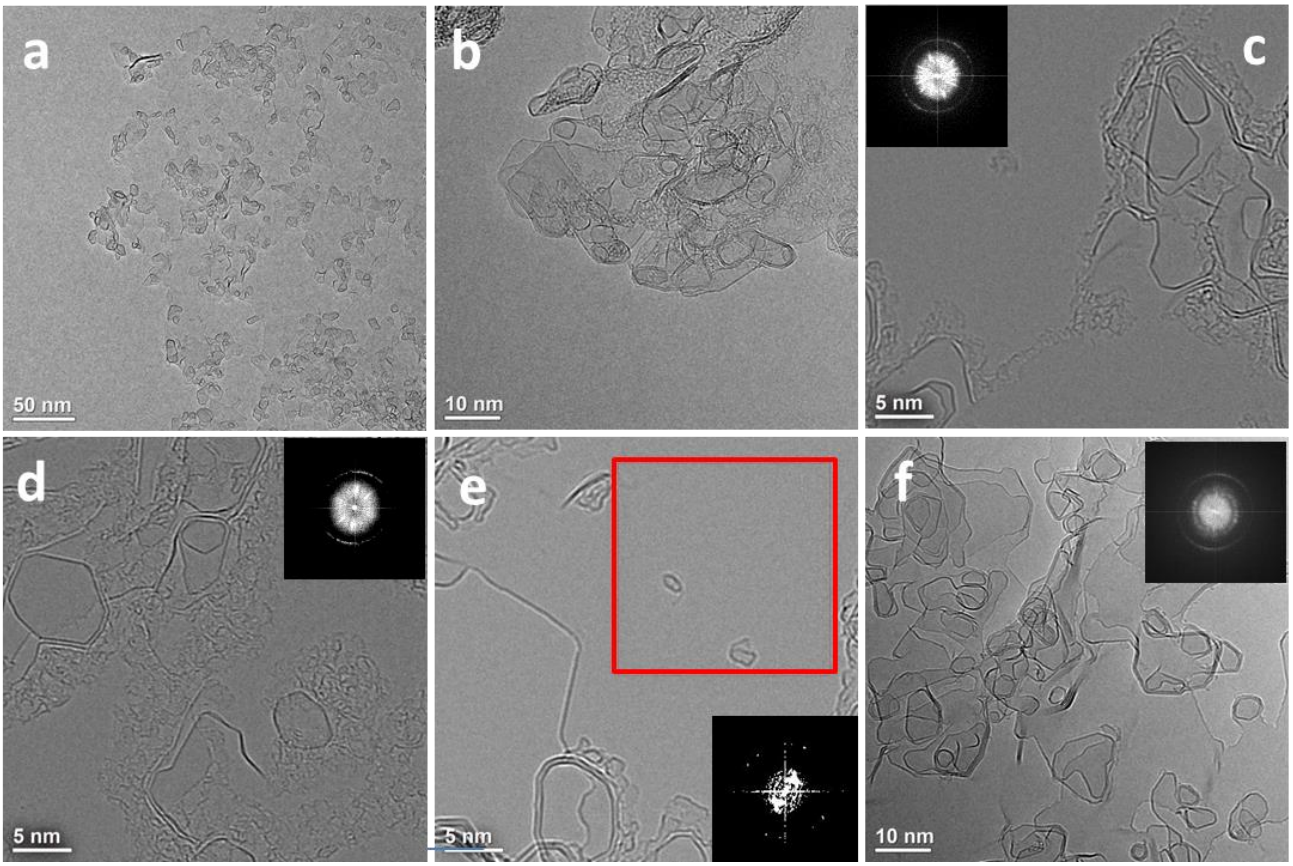

Figure 5.7: (a-f) Broken thin film after current annealing to ultra-high temperatures, showing the presence of large domains, (f) large area thin film showing two sets of hexagonal spots in FFT, corresponding to highly grown crystallites.

5.6. Structural evolution at ultra-high temperatures

To avoid early film breakage, current annealing experiments were conducted on thick samples with a thickness of more than 10 nm (Figure 5.8). These thick samples show structures with large multi-walled cage-like structures, resembling bamboo type MWCNTs with metallic impurities distributed in between. The metallic impurities are from molten platinum from the electrodes, which were migrating on the sample with the current running through the sample. The cages like structures show a directional elongation towards the electrodes. This can be either due to the stress induced in the film or because of the electro-migration during heating and transformation. Furthermore, the negative coefficient of thermal expansion for the graphitized films can induce a tensile stress in the film and cause an elongation in the cage-like structures. [163] More detailed studies would be necessary to separate out these effects and understand the reason for the observed directional elongation. Well stacked graphitic layers can be seen in Figure 5.8h and the FFT from the area marked is given in Figure 5.8f. FFT shows two sets of spots corresponding to 2.912 nm^{-1} and 4.77 nm^{-1}. These are {002} and {110} reflection respectively in graphite. The value 2.912 shows a uniform interlayer distance of 0.343 nm corresponding to ordered graphitic material. These tubular type structures are reported during *in situ* current annealing of amorphous carbon fibers inside TEM. [70] The amorphous carbon initially transformed in to graphitic onions and further annealing resulted in a tubule formation. Closed structures are also reported during current induced transformation on graphite. [67] Thus the size and shape of the structures show that current annealing can be used to grow the domain sizes in the order of hundreds of nanometers.

Along with the large domains, small domains are still visible, which did not transform, in both thin sample (Figure 5.7) and thick samples (Figure 5.8). The reason for this can be the high heating rate during current annealing. High heating rates can lead to the formation of a sudden narrow conduction channel with higher current flow. This region will be heated fast leaving the domains in the vicinity unchanged. Thickness variation, defect density etc. can induce local conduction channels, which will be transformed faster compared to others. The reason for formation of cage-like structures has to understand in detail. The thickness of the sample and the heating rate seem to have an effect in the formation.

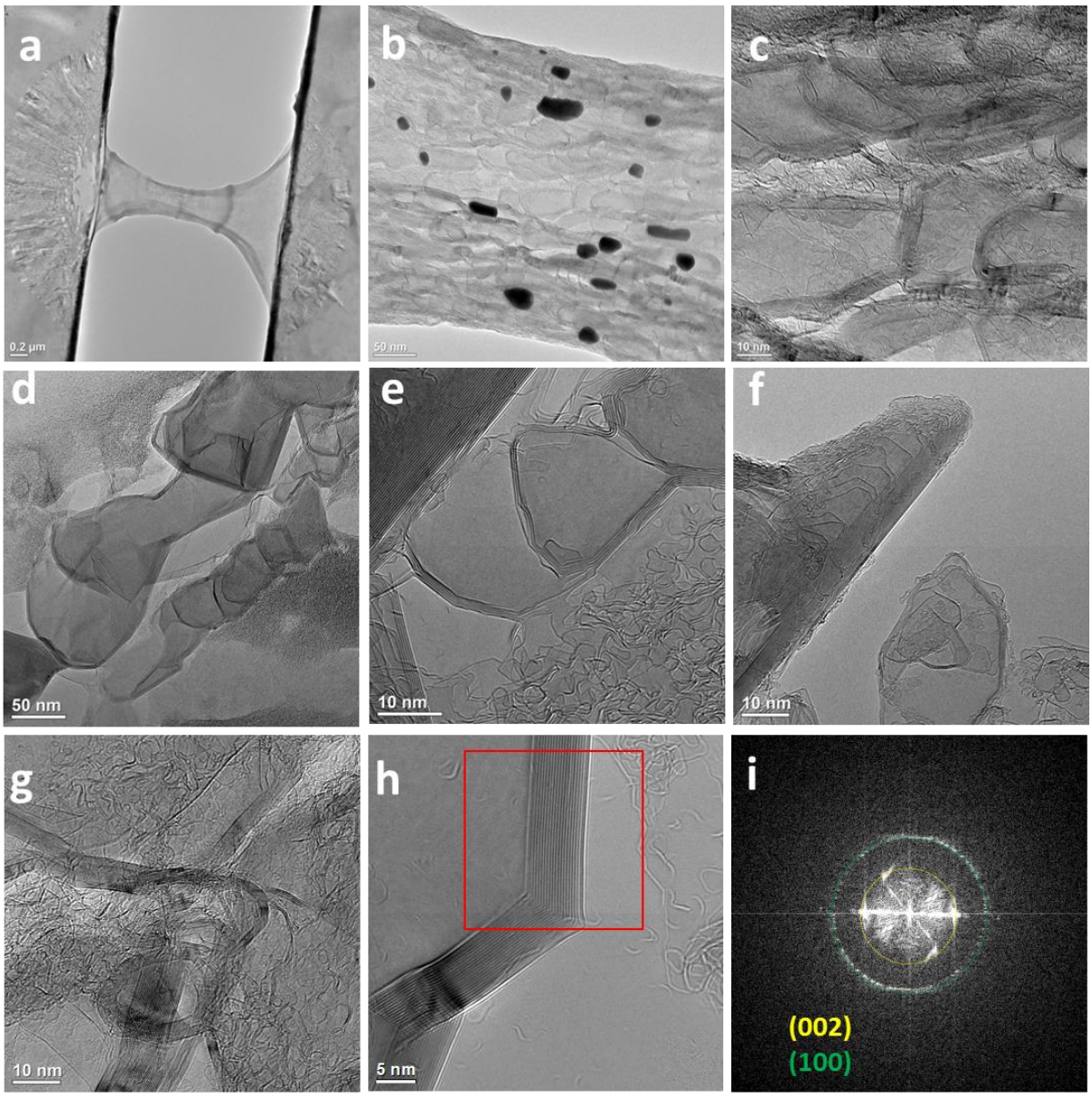

Figure 5.8: (a-f) Cage-like structures formed during current annealing of thick sample, (g,h) perfectly stacked walls of a closed cage structure formed and (i) FFT from the marked region showing two sets of rings corresponding to (002) and (110) reflections.

Formation of 3D hollow structures has been observed previously during current annealing of graphene [164] and graphite. [67–69] Current annealing in graphene resulted in bonded bilayers which showed higher stability than the open unsaturated edges. Similarly in the case of bulk graphite also, current annealing

resulted in the formation of aligned hollow 3 dimensional graphitic shells bounded by few layers of graphene. [165] Transformation of folded bilayer to hollow structures during passage of current is a proposed mechanism. [68] Here also, the edges might be playing an important role. During current annealing, due to the sublimation of species like O and H, free edges are created and to increase the stability, these edges might bond with underlying edges forming a multiwall closed structure. The high heating rate, compared to the conventional annealing might facilitate rapid sublimation of edge elements forming highly unstable free edges. This can result in bonding of edges and formation of closed structures unlike the formation of flat stacked layers in conventional thermal annealing. This can also happen to the thin films and some of the edges in the flat structures that we see can be bonded bilayer structures. But we also observe some isolated large flakes on the top of the graphitic substrate which shows the presence of non-bonded isolated flakes. Controlled experiments and more detailed characterization of the edge structure are needed to understand the formation of these different kinds of structures.

5.7. Conclusion

This chapter studies the effect of current annealing on graphitization and structural evolution of nano crystalline graphene. Current annealing on the top of free-standing SiN membrane was restricted to lower temperature due to the crystallization and breaking of SIN membrane. The breaking of SiN destroys the thin ncg membrane on the top preventing further heating. To avoid this, free-standing ncg constrictions were fabricated and current annealed inside TEM following the transformations *in situ*. The study showed that the graphitization until high temperature is comparable with thermal annealing. Furthermore with current annealing, we can reach ultra-high temperatures, ($T > 2000$ ºC) and domains can grow as large as 50 nm. However, at least in the thick samples, the study showed the formation of cage-like structures during the current annealing, where we have not seen a counter part in the thermally grown graphite. The thickness of the sample and the heating rate seems to have an influence on the structural evolution during current annealing. This opens up new possibilities to tailor the microstructure and conductivity by controlling the thickness the heating rate in the sample.

6. Conclusion and out look

6.1. Conclusion

In the present study *in situ* HRTEM studies have been carried out to understand the graphitization and grain growth in nanocrystalline graphene during pyrolysis of a free-standing polymer film. HRTEM, selected area electron diffraction (SAED) and electron energy loss spectroscopy (EELS) techniques were used to follow the graphitization *in situ* and to understand the evolution of nanocrystalline domains at different temperatures. Beam off experiments were carried out to understand the effect of electron beam. Furthermore atomistic simulation studies were carried out in collaboration to estimate the activation energy for the different processes and to understand the role of defects in the substrate for the observed dynamics. The key outcomings of the present thesis are

6.1.1. Method development for *in situ* heating and current annealing

The study put forward an efficient and flexible sample preparation procedure for the *in situ* heating studies and current annealing studies that can be extended to other polymer systems also. For *in situ* graphitization, it is required to form thin polymer films on MEMS based heating chips. This is accomplished by spin coating the polymer on to the MEMS based heating chip. This forms free-standing polymer films over the holes of the heating chips which can undergo substrate less graphitization forming large area thin films suitable for TEM analysis. *In situ* graphitization eliminates the possible defects and structural changes associated with sample preparation in the conventional TEM analysis. The use of pre-calibrated, MEMS based heating chips enables a good correlation of the temperature and the corresponding structural changes. For *in situ* current annealing studies, *ex situ* pre graphitized films were transferred and then lithographically patterned to form free-standing thin ncg constrictions. This provided the possibility to current anneal the film to ultrahigh temperatures and to image the structural changes during heating.

6.1.2. Understanding graphitization

In situ graphitization provided new insights in to the pyrolysis process. The graphitization of the free-standing film was comparable to the substrate supported graphitization. This allowed direct correlation of the structural changes during *in situ* heating with conventional pyrolysis process. The *in situ* studies showed that the graphitization process is highly dynamic in nature with a number of intermediate reactions leading

to the formation of different carbon nanostructures A two-step growth mechanism was identified where the growth of the crystallites in the intermediate temperature range of 600-1000 °C mainly occurs by consuming residual amorphous carbon around graphitic domains. At higher temperatures of 1000-1200 °C, larger domains become mobile and the growth proceeds by merging of these mobile domains on the surface of preformed graphene layers. The amorphous carbon transforms in one of two ways, either by attaching to active edges of graphitic domains or by catalyst free growth on top of a graphitic layer. This catalyst free transformation forms new small graphitic structures, some of which are highly mobile at higher temperatures and get attached to the edges, extending the edges. Studying the dynamics of these carbon nanostructures provided insights into the high temperature stability/mobility and the interaction with the graphitic substrates.

6.1.3. Insights into the high temperature growth of ncg

Time resolved HRTEM investigations on the high temperature behavior of ncg gave new insights in to the fundamental mechanisms controlling the ncg growth. The results show that the high-temperature behavior of the nanocrystalline graphene is different from pristine graphene. *In situ* HRTEM investigations supported by the atomistic simulations show the critical role of defects in the high temperature dynamics. The main growth mechanism identified is the migration and merging of domains. *In situ* experiments along with MD simulations reveal that unlike the observed high diffusion of nano-structures on defect-free graphene, in ncg migration is hindered by pinning to defect sites in the substrate. The flakes can merge both laterally and with the underlying layers facilitating both lateral and vertical mass transfer. The merging is facilitated by initial bond formation between the highly dynamic and constantly rearranging domain edges. The dynamics of the merging events differ considerably according to the material transfer direction. In addition to this, the study provides experimental evidence for Ostwald like ripening in these 2D materials. At high temperature, graphene nano-flakes are highly unstable and tend to lose atoms or groups of atoms, while adjacent larger flakes grow by the addition of atoms, indicating an Ostwald like ripening in these 2D materials. The role of electron beam was analyzed by beam off experiments. The beam off experiments confirm that the observed dynamics are inherent temperature driven and the beam is only providing some additional activation energy, increasing the dynamics. Furthermore, Nudged Elastic Band (NEB) calculations were carried out to find out the activation energies associated with different observed dynamics. Beam off experiments and the

atomistic simulation studies confirm that the observed dynamics are inherent temperature driven processes and the electron beam is only providing an additional activation energy increasing the reaction kinetics.

6.1.4. Ultra-high temperature structure and dynamics

In situ current annealing experiments enabled direct visualization of the structural evolution of ncg at ultra-high temperatures. Graphitization by current annealing was comparable with thermal annealing until high temperature (T = 1200 ºC). Furthermore with current annealing, it is possible to reach ultra-high temperatures, (T > 2000 ºC) and domains grow as large as 50 nm. In the thick samples, formation of multi walled cage-like structures are observed, whereas no such structures are reported in thermally grown graphite. The thickness of the sample and the heating rate seems to have an influence on the structural evolution during current annealing. This opens up new possibilities to tailor the microstructure and conductivity by controlling the thickness by controlling the heating rate in the sample.

6.1.5. New insights into the polymer pyrolysis

The present study can give new valuable inputs in understanding polymer pyrolysis leading to the formation of bulk graphitizing and non-graphitizing carbons. *In situ* graphitization and growth shows that most of the growing flakes are flat and contain reactive edges growing in all directions. The study also shows that the merging of domains can be both lateral and vertical. This means that not only the oriented domains can merge laterally but also the misoriented domains can grow by vertical merging. This kind of vertical merging is important in graphitizing carbons, which might contribute to complete graphitization at very high temperatures. With the highly defective structure in bulk glassy carbons, apart from the merging of domains, Ostwald-like ripening can also be a contributing growth mechanism. As the thickness increases, there are more defects and also a higher number of diffusion pathways in different orientations. This can increase the possibility for atom transfer between differently oriented inter-connected domains. These results open up new possibility to understand the graphitizing and non-graphitizing nature of carbons.

6.2. Outlook

With the interesting electronic, structural properties and the flexibility in fabrication, ncg can be used in wide variety of technological fields and this necessitates a detailed understanding of the structure property

correlations. Variety of characterization methods can be envisioned to accomplish this. However, thinking from the scope of the present study, considering *in situ* TEM methods, some interesting directions can be

6.2.1. High resolution STEM study on the structure

High resolution *in situ* STEM study of the structural changes observed will provide added information about the stacking of domains and the high temperature edge structure of the large and small flakes. This can provide better understanding of the lateral/vertical merging and the difference in dynamics. It is clear from the experiment and simulation studies that the Ostwald like ripening is also greatly influenced by local edge curvature and edge structure. This can throw light in to the mechanism of atom removal and the opening of edge for the addition of atom. HRSTEM study of the edge structure can be instrumental in understanding the formation of multi-walled cage-like structures during the current annealing.

6.2.2. Controlled *in situ* current annealing

Even though the present study briefly discuss about the structural evolution during current annealing experiments, correlation of the sheet resistance with graphitization will be an important step forward towards property specific ncg material. This can be achieved by precisely designing the free-standing heating constrictions confining the heating to a small measurable area. Electron beam sculpting can be used to precisely cut the free-standing thin films transferred on to the electro contacting chip. This can produce small constructions that can be uniformly heated and imaged. Furthermore the effect of passing current, heating rate and the thickness of the film on the formation, size /shape of the large cage-like structures can be understood by controlled *in situ* current annealing experiments.

6.2.3. *In situ* Mechanical deformation studies

In situ straining of nanocrystalline graphene inside the microscope can be exciting to study the mechanical properties of nanocrystalline graphene. This can provide information about the deformation mechanisms and the structural changes during deformation. For *In situ* straining studies, commercially available push to pull device (Hysitron) can be used. Ncg thin films can be directly transferred to the push to pull device after etching out the substrate. This large area films can be patterned using 300 kV electron beam and can be strained inside the TEM. This can provide information about the mechanical properties and deformation mechanisms operation during the straining of ncg. Furthermore a straining electrical chip from Hystiron can

be used to get the variation in resistance during straining. Combination of electrical measurements with straining can provide important information about the origin of piezo resistivity in ncg.

References

[1] Z. Zhang, B. Ge, Y. Guo, D. Tang, X. Wang, F. Wang, Catalyst-free growth of nanocrystalline graphene/graphite patterns from photoresist, Chem. Commun. 49 (2013) 2789–2791. doi:10.1039/c3cc00089c.

[2] K.S. Novoselov, V.I. Fal′ko, L. Colombo, P.R. Gellert, M.G. Schwab, K. Kim, A roadmap for graphene, Nature. 490 (2012) 192–200. doi:10.1038/nature11458.

[3] H. Nguyen Bich, H. Nguyen Van, Promising applications of graphene and graphene-based nanostructures, Adv. Nat. Sci. Nanosci. Nanotechnol. 7 (2016) 1–15. doi:10.1088/2043-6262/7/2/023002.

[4] D.R. Cooper, B. D'Anjou, N. Ghattamaneni, B. Harack, M. Hilke, A. Horth, N. Majlis, M. Massicotte, L. Vandsburger, E. Whiteway, V. Yu, Experimental Review of Graphene, ISRN Condens. Matter Phys. 2012 (2012) 1–56. doi:10.5402/2012/501686.

[5] G. Yang, L. Li, W.B. Lee, M.C. Ng, Structure of graphene and its disorders: a review, Sci. Technol. Adv. Mater. 19 (2018) 613–648. doi:10.1080/14686996.2018.1494493.

[6] A.S. Mayorov, R. V. Gorbachev, S. V. Morozov, L. Britnell, R. Jalil, L.A. Ponomarenko, P. Blake, K.S. Novoselov, K. Watanabe, T. Taniguchi, A.K. Geim, Micrometer-Scale Ballistic Transport in Encapsulated Graphene at Room Temperature, Nano Lett. 11 (2011) 2396–2399. doi:10.1021/nl200758b.

[7] A.A. Balandin, Thermal properties of graphene and nanostructured carbon materials, Nat. Mater. 10 (2011) 569–581. doi:10.1038/nmat3064.

[8] C. Lee, X. Wei, J.W. Kysar, J. Hone, Measurement of the Elastic Properties and Intrinsic Strength of Monolayer Graphene, Science (80-.). 321 (2008) 385–388. doi:10.1126/science.1157996.

[9] Z. Zhang, Y. Guo, X. Wang, D. Li, F. Wang, S. Xie, Direct growth of nanocrystalline graphene/graphite transparent electrodes on Si/SiO2 for metal-free schottky junction photodetectors, Adv. Funct. Mater. 24 (2014) 835–840. doi:10.1002/adfm.201301924.

[10] S. Sharma, A. Khalajhedayati, T.J. Rupert, M.J. Madou, SU8 Derived Glassy Carbon for Lithium Ion Batteries, ECS Trans. 61 (2014) 75–84. doi:10.1149/06107.0075ecst.

[11] A. Riaz, F. Pyatkov, A. Alam, S. Dehm, A. Felten, V.S.K. Chakravadhanula, B.S. Flavel, C. Kübel, U. Lemmer, R. Krupke, Light emission, light detection and strain sensing with nanocrystalline graphene, Nanotechnology. 26 (2015) 325202. doi:10.1088/0957-4484/26/32/325202.

[12] J.A. Rodríguez-Manzo, A. V Krasheninnikov, F. Banhart, Engineering the Atomic Structure of Carbon Nanotubes by a Focused Electron Beam: New Morphologies at the Sub-Nanometer Scale, ChemPhysChem. 13 (2012) 2596–2600. doi:10.1002/cphc.201101000.

[13] F. Banhart, J. Kotakoski, A. V Krasheninnikov, Structural defects in graphene., ACS Nano. 5 (2011) 26–41. doi:10.1021/nn102598m.

[14] J.C. Meyer, A.K. Geim, M.I. Katsnelson, K.S. Novoselov, T.J. Booth, S. Roth, The structure of suspended graphene sheets, Nature. 446 (2007) 60–63. doi:10.1038/nature05545.

[15] C.O. Girit, J.C. Meyer, R. Erni, M.D. Rossell, C. Kisielowski, L. Yang, C.-H. Park, M.F. Crommie, M.L. Cohen, S.G. Louie, A. Zettl, Graphene at the Edge: Stability and Dynamics, Science (80-.). 323 (2009) 1705–1708. doi:10.1126/science.1166999.

[16] J. Kotakoski, J.C. Meyer, S. Kurasch, D. Santos-Cottin, U. Kaiser, a. V. Krasheninnikov, Stone-Wales-type transformations in carbon nanostructures driven by electron irradiation, Phys. Rev. B. 83 (2011) 245420. doi:10.1103/PhysRevB.83.245420.

[17] A.W. Robertson, G.-D. Lee, K. He, E. Yoon, A.I. Kirkland, J.H. Warner, Stability and dynamics of the tetravacancy in graphene., Nano Lett. 14 (2014) 1634–42. doi:10.1021/nl500119p.

[18] O. Lehtinen, I.-L. Tsai, R. Jalil, R.R. Nair, J. Keinonen, U. Kaiser, I. V Grigorieva, Non-invasive transmission electron microscopy of vacancy defects in graphene produced by ion irradiation, Nanoscale. 6 (2014) 6569–6576. doi:10.1039/c4nr01918k.

[19] N. Lu, J. Wang, H.C. Floresca, M.J. Kim, In situ studies on the shrinkage and expansion of graphene nanopores under electron beam irradiation at temperatures in the range of 400-1200 ??c, Carbon N. Y. 50 (2012) 2961–2965. doi:10.1016/j.carbon.2012.02.078.

[20] K. He, A.W. Robertson, Y. Fan, C.S. Allen, Y. Lin, K. Suenaga, A.I. Kirkland, J.H. Warner, Temperature Dependence of the Reconstruction of Zigzag Edges in Graphene, ACS Nano. 9 (2015) 4786–4795. doi:10.1021/acsnano.5b01130.

[21] Z.J. Qi, J.A. Rodríguez-Manzo, A.R. Botello-Méndez, S.J. Hong, E. a Stach, Y.W. Park, J. Charlier, M. Drndić, a T.C. Johnson, Correlating Atomic Structure and Transport in Suspended Graphene Nanoribbons, Nano Lett. 14 (2014) 4238–4244. doi:10.1021/nl501872x.

[22] Q. Wang, R. Kitaura, S. Suzuki, Y. Miyauchi, K. Matsuda, Y. Yamamoto, S. Arai, H. Shinohara, Fabrication and In Situ Transmission Electron Microscope Characterization of Free-Standing Graphene Nanoribbon Devices, ACS Nano. 10 (2016) 1475–1480. doi:10.1021/acsnano.5b06975.

[23] P.Y. Huang, C.S. Ruiz-Vargas, A.M. van der Zande, W.S. Whitney, M.P. Levendorf, J.W. Kevek, S. Garg, J.S. Alden, C.J. Hustedt, Y. Zhu, J. Park, P.L. McEuen, D.A. Muller, Grains and grain boundaries in single-layer graphene atomic patchwork quilts, Nature. 469 (2011) 389–392. doi:10.1038/nature09718.

[24] A.W. Robertson, J.H. Warner, Atomic resolution imaging of graphene by transmission electron microscopy, Nanoscale. 5 (2013) 4079. doi:10.1039/c3nr00934c.

[25] P. Angelova, H. Vieker, N.E. Weber, D. Matei, O. Reimer, I. Meier, S. Kurasch, J. Biskupek, D. Lorbach, K. Wunderlich, L. Chen, A. Terfort, M. Klapper, K. Müllen, U. Kaiser, A. Gölzhäuser, A. Turchanin, A universal scheme to convert aromatic molecular monolayers into functional carbon nanomembranes, ACS Nano. 7 (2013) 6489–6497. doi:10.1021/nn402652f.

[26] A. Turchanin, D. Weber, M. Büenfeld, C. Kisielowski, M. V. Fistul, K.B. Efetov, T. Weimann, R. Stosch, J. Mayer, A. Gölzhäuser, Conversion of self-assembled monolayers into nanocrystalline graphene: Structure and electric transport, ACS Nano. 5 (2011) 3896–3904. doi:10.1021/nn200297n.

[27] S.-Y. Son, Y.-J. Noh, C. Bok, S. Lee, B.G. Kim, S.-I. Na, H.-I. Joh, One-step synthesis of carbon nanosheets converted from a polycyclic compound and their direct use as transparent electrodes of ITO-free organic solar cells., Nanoscale. 6 (2014) 678–82. doi:10.1039/c3nr04828d.

[28] H. Medina, Y.C. Lin, C. Jin, C.C. Lu, C.H. Yeh, K.P. Huang, K. Suenaga, J. Robertson, P.W. Chiu, Metal-free growth of nanographene on silicon oxides for transparent conducting applications, Adv. Funct. Mater. 22 (2012) 2123–2128. doi:10.1002/adfm.201102423.

[29] S. Bae, H. Kim, Y. Lee, X. Xu, J.S. Park, Y. Zheng, J. Balakrishnan, T. Lei, H. Ri Kim, Y. Il Song, Y.J. Kim, K.S. Kim, B. Özyilmaz, J.H. Ahn, B.H. Hong, S. Iijima, Roll-to-roll production of 30-inch graphene films for transparent electrodes, Nat. Nanotechnol. 5 (2010) 574–578. doi:10.1038/nnano.2010.132.

[30] A. Shekhawat, R.O. Ritchie, Toughness and strength of nanocrystalline graphene, Nat. Commun. 7 (2016) 10546. doi:10.1038/ncomms10546.

[31] T. Zhang, X. Li, S. Kadkhodaei, H. Gao, Flaw Insensitive Fracture in Nanocrystalline Graphene, Nano Lett. 12 (2012) 4605–4610. doi:10.1021/nl301908b.

[32] M.H. Rümmeli, A. Bachmatiuk, A. Scott, F. Börrnert, J.H. Warner, V. Hoffmann, J.-H. Lin, G. Cuniberti, B. Büchner, Direct Low Temperature Nano-Graphene Synthesis over a Dielectric Insulator, ACS Nano. 4 (2011) 4206–4210. doi:10.1021/nn100971s.

[33] J. Sun, N. Lindvall, M.T. Cole, K.B.K. Teo, A. Yurgens, Chemical vapor deposition of nanocrystalline graphene directly on arbitrary high-temperature insulating substrates, 2012 7th IEEE Int. Conf. Nano/Micro Eng. Mol. Syst. NEMS 2012. (2012) 11–14. doi:10.1109/NEMS.2012.6196711.

[34] J. Chen, Y. Wen, Y. Guo, B. Wu, L. Huang, Y. Xue, D. Geng, D. Wang, G. Yu, Y. Liu, Oxygen-aided synthesis of polycrystalline graphene on silicon dioxide substrates, J. Am. Chem. Soc. 133 (2011) 17548–17551. doi:10.1021/ja2063633.

[35] L. Zhang, Z. Shi, Y. Wang, R. Yang, D. Shi, G. Zhang, Catalyst-free growth of nanographene films on various substrates, Nano Res. 4 (2011) 315–321. doi:10.1007/s12274-010-0086-5.

[36] M.H. Oliveira, T. Schumann, R. Gargallo-Caballero, F. Fromm, T. Seyller, M. Ramsteiner, A. Trampert, L. Geelhaar, J.M.J. Lopes, H. Riechert, Mono- and few-layer nanocrystalline graphene grown

on Al2O3(0001) by molecular beam epitaxy, Carbon N. Y. 56 (2013) 339–350. doi:10.1016/j.carbon.2013.01.032.

[37] S.K. Jerng, D.S. Yu, Y.S. Kim, J. Ryou, S. Hong, C. Kim, S. Yoon, D.K. Efetov, P. Kim, S.H. Chun, Nanocrystalline graphite growth on sapphire by carbon molecular beam epitaxy, J. Phys. Chem. C. 115 (2011) 4491–4494. doi:10.1021/jp110650d.

[38] T. Schumann, M. Dubslaff, M.H. Oliveira, M. Hanke, F. Fromm, T. Seyller, L. Nemec, V. Blum, M. Scheffler, J.M.J. Lopes, H. Riechert, Structural investigation of nanocrystalline graphene grown on ($6\sqrt{3} \times 6\sqrt{3}$) R 30°-reconstructed SiC surfaces by molecular beam epitaxy, New J. Phys. 15 (2013) 123034. doi:10.1088/1367-2630/15/12/123034.

[39] C.T. Nottbohm, a. Turchanin, a. Beyer, a. Gölzhäuser, Direct e-beam writing of 1 nm thin carbon nanoribbons, J. Vac. Sci. Technol. B Microelectron. Nanom. Struct. 27 (2009) 3059. doi:10.1116/1.3253536.

[40] M. Min, S. Seo, Y. Yoon, K. Cho, S.M. Lee, T. Lee, H. Lee, Catalyst-free bottom-up growth of graphene nanofeatures along with molecular templates on dielectric substrates, Nanoscale. 8 (2016) 17022–17029. doi:10.1039/C6NR05657A.

[41] R.E. Franklin, Crystallite Growth in Graphitizing and Non-Graphitizing Carbons, Proc. R. Soc. A Math. Phys. Eng. Sci. 209 (1951) 196–218. doi:10.1098/rspa.1951.0197.

[42] J.N. Rouzaud, A. Oberlin, Structure, microtexture, and optical properties of anthracene and saccharose-based carbons, Carbon N. Y. 27 (1989) 517–529. doi:10.1016/0008-6223(89)90002-X.

[43] P.J.F. Harris, New Perspectives on the Structure of Graphitic Carbons, Crit. Rev. Solid State Mater. Sci. 30 (2005) 235–253. doi:10.1080/10408430500406265.

[44] P.J.F. Harris, S.C. Tsang, High-resolution electron microscopy studies of non-graphitizing carbons, Philos. Mag. A. 76 (1997) 667–677. doi:10.1080/01418619708214028.

[45] J.D. BROOKS, G.H. TAYLOR, Formation of Graphitizing Carbons from the Liquid Phase, Nature. 206 (1965) 697–699. doi:10.1038/206697a0.

[46] A. Oberlin, Carbonization and graphitization, Carbon N. Y. 22 (1984) 521–541. doi:10.1016/0008-6223(84)90086-1.

[47] R.E. Franklin, Crystallite Growth in Graphitizing and Non-Graphitizing Carbons, Proc. R. Soc. A Math. Phys. Eng. Sci. 209 (1951) 196–218. doi:10.1098/rspa.1951.0197.

[48] J. Biscoe, B.E. Warren, An X-Ray Study of Carbon Black, J. Appl. Phys. 13 (1942) 364–371. doi:10.1063/1.1714879.

[49] A. Celzard, V. Fierro, Fundamental and Applied Nano-Electromagnetics, Springer Netherlands, Dordrecht, 2016. doi:10.1007/978-94-017-7478-9.

[50] G.M. JENKINS, K. KAWAMURA, Structure of Glassy Carbon, Nature. 231 (1971) 175–176. doi:10.1038/231175a0.

[51] L.L. Ban, D. Crawford, H. Marsh, Lattice-resolution electron microscopy in structural studies of non-graphitizing carbons from polyvinylidene chloride (PVDC), J. Appl. Crystallogr. 8 (1975) 415–420. doi:10.1107/S0021889875010904.

[52] J. Goma, M. Oberlin, Graphitization of thin carbon films, Thin Solid Films. 65 (1980) 221–232. doi:10.1016/0040-6090(80)90256-4.

[53] P.J.F. Harris, Fullerene-related structure of commercial glassy carbons, Philos. Mag. 84 (2004) 3159–3167. doi:10.1080/14786430410001720363.

[54] S. Kodera, N. Minami, T. Ino, The Structure of Glassy Carbon, Jpn. J. Appl. Phys. 25 (1986) 328–335. doi:10.1143/JJAP.25.328.

[55] S. Ergun, R.R. Schehl, Analysis of the structure of a glassy carbon using the fourier transform technique, Carbon N. Y. 11 (1973) 127–138. doi:10.1016/0008-6223(73)90063-8.

[56] D.F.R. Mildner, J.M. Carpenter, On the short range atomic structure of non-crystalline carbon, J. Non. Cryst. Solids. 47 (1982) 391–402. doi:10.1016/0022-3093(82)90215-0.

[57] M.I. Nathan, J.E. Smith, K.N. Tu, Raman spectra of glassy carbon, J. Appl. Phys. 45 (1974) 2370–2370. doi:10.1063/1.1663599.

[58] L.A. Pesin, Structure and properties of glass-like carbon, J. Mater. Sci. 37 (2002) 1–28. doi:10.1023/A:1013100920130.

[59] H. Daniels, R. Brydson, B. Rand, A. Brown, Investigating carbonization and graphitization using electron energy loss spectroscopy (EELS) in the transmission electron microscope (TEM), Philos. Mag. 87 (2007) 4073–4092. doi:10.1080/14786430701394041.

[60] J.Y. Huang, S. Chen, S.H. Jo, Z. Wang, D.X. Han, G. Chen, M.S. Dresselhaus, Z.F. Ren, Atomic-Scale Imaging of Wall-by-Wall Breakdown and Concurrent Transport Measurements in Multiwall Carbon Nanotubes, Phys. Rev. Lett. 94 (2005) 236802. doi:10.1103/PhysRevLett.94.236802.

[61] J.Y. Huang, S. Chen, Z.Q. Wang, K. Kempa, Y.M. Wang, S.H. Jo, G. Chen, M.S. Dresselhaus, Z.F. Ren, Superplastic carbon nanotubes, Nature. 439 (2006) 281–281. doi:10.1038/439281a.

[62] R. Murali, Y. Yang, K. Brenner, T. Beck, J.D. Meindl, Breakdown current density of graphene nanoribbons, Appl. Phys. Lett. 94 (2009) 243114. doi:10.1063/1.3147183.

[63] H. Zhang, W. Bao, Z. Zhao, J.-W. Huang, B. Standley, G. Liu, F. Wang, P. Kratz, L. Jing, M. Bockrath, C.N. Lau, Visualizing Electrical Breakdown and ON/OFF States in Electrically Switchable Suspended Graphene Break Junctions, Nano Lett. 12 (2012) 1772–1775. doi:10.1021/nl203160x.

[64] A. Barreiro, F. Börrnert, S.M. Avdoshenko, B. Rellinghaus, G. Cuniberti, M.H. Rümmeli, L.M.K. Vandersypen, Understanding the catalyst-free transformation of amorphous carbon into graphene by current-induced annealing, Sci. Rep. 3 (2013) 1115. doi:10.1038/srep01115.

[65] B. Westenfelder, J.C. Meyer, J. Biskupek, S. Kurasch, F. Scholz, C.E. Krill, U. Kaiser, Transformations of Carbon Adsorbates on Graphene Substrates under Extreme Heat, Nano Lett. 11 (2011) 5123–5127. doi:10.1021/nl203224z.

[66] Y. Lu, C.A. Merchant, M. Drndić, A.T.C. Johnson, In situ electronic characterization of graphene nanoconstrictions fabricated in a transmission electron microscope, Nano Lett. 11 (2011) 5184–5188. doi:10.1021/nl2023756.

[67] P.J.F. Harris, T.J.A. Slater, S.J. Haigh, F.S. Hage, D.M. Kepaptsoglou, Q.M. Ramasse, R. Brydson, Bilayer graphene formed by passage of current through graphite: evidence for a three-dimensional structure, Nanotechnology. 25 (2014) 465601. doi:10.1088/0957-4484/25/46/465601.

[68] P.J.F. Harris, Hollow structures with bilayer graphene walls, Carbon N. Y. 50 (2012) 3195–3199. doi:10.1016/j.carbon.2011.10.050.

[69] P.J.F. Harris, Structural transformation of graphite by arc-discharge, Philos. Mag. 91 (2011) 2355–2363. doi:10.1080/14786435.2011.562250.

[70] J.Y. Huang, S. Chen, Z.F. Ren, G. Chen, M.S. Dresselhaus, Real-Time Observation of Tubule Formation from Amorphous Carbon Nanowires under High-Bias Joule Heating, Nano Lett. 6 (2006) 1699–1705. doi:10.1021/nl0609910.

[71] K. Zheng, R. Shao, J. Wang, Z. Liao, N. Marks, P. Chen, W. Lu, X. Han, J. Zou, Fabrication of individual carbon nanotubes and their arrays in a transmission electron microscope, Carbon N. Y. 100 (2016) 435–440. doi:10.1016/j.carbon.2015.12.029.

[72] B. Wang, D.E. Wolfe, M. Terrones, M.A. Haque, S. Ganguly, A.K. Roy, Electro-graphitization and exfoliation of graphene on carbon nanofibers, Carbon N. Y. 117 (2017) 201–207. doi:10.1016/j.carbon.2017.02.086.

[73] R.C. Powles, N.A. Marks, D.W.M. Lau, Self-assembly of s p2 -bonded carbon nanostructures from amorphous precursors, Phys. Rev. B - Condens. Matter Mater. Phys. 79 (2009) 1–11. doi:10.1103/PhysRevB.79.075430.

[74] I. Suarez-Martinez, N.A. Marks, Amorphous carbon nanorods as a precursor for carbon nanotubes, Carbon N. Y. 50 (2012) 5441–5449. doi:10.1016/j.carbon.2012.07.030.

[75] J. Bauer, A. Schroer, R. Schwaiger, O. Kraft, Approaching theoretical strength in glassy carbon nanolattices, Nat. Mater. 15 (2016) 438–443. doi:10.1038/nmat4561.

[76] J. Bauer, Fabricating lightweight and ultrastrong mechanical metamaterials, SPIE Newsroom. (2017) 10–11. doi:10.1117/2.1201703.006832.

[77] M.H. Rummeli, H.Q. Ta, R.G. Mendes, I.G. Gonzalez-Martinez, L. Zhao, J. Gao, L. Fu, T. Gemming, A. Bachmatiuk, Z. Liu, New Frontiers in Electron Beam-Driven Chemistry in and around Graphene, Adv. Mater. 1800715 (2018) 1800715. doi:10.1002/adma.201800715.

[78] Z. Liu, Y.-C. Lin, C.-C. Lu, C.-H. Yeh, P.-W. Chiu, S. Iijima, K. Suenaga, In situ observation of step-edge in-plane growth of graphene in a STEM, Nat. Commun. 5 (2014) 1–7. doi:10.1038/ncomms5055.

[79] A. Chuvilin, U. Kaiser, E. Bichoutskaia, N. a Besley, A.N. Khlobystov, Direct transformation of graphene to fullerene, Nat. Chem. 2 (2010) 450–453. doi:10.1038/nchem.644.

[80] M. Knoll, E. Ruska, Das Elektronenmikroskop, Zeitschrift Für Phys. 78 (1932) 318–339. doi:10.1007/BF01342199.

[81] J.W. Menter, The Direct Study by Electron Microscopy of Crystal Lattices and their Imperfections, Proc. R. Soc. A Math. Phys. Eng. Sci. 236 (1956) 119–135. doi:10.1098/rspa.1956.0117.

[82] J.C. Russ, X-ray spectroscopy on the electron microscope, X-Ray Spectrom. 2 (1973) 11–14. doi:10.1002/xrs.1300020105.

[83] R.M. Henkelman, F.P. Ottensmeyer, An energy filter for biological electron microscopy, J. Microsc. 102 (1974) 79–94. doi:10.1111/j.1365-2818.1974.tb03968.x.

[84] M. Haider, S. Uhlemann, E. Schwan, H. Rose, B. Kabius, K. Urban, Electron microscopy image enhanced, Nature. 392 (1998) 768–769. doi:10.1038/33823.

[85] U. Kaiser, J. Meyer, J. Biskupek, J. Leschner, A. Khlobystov, H. Müller, P. Hartel, M. Haider, S. Eyhusen, G. Benner, High Resolution 20kV Transmission Electron Microscopy of Nanosystems – First Results Towards Sub Ångstrøm Low Voltage EM (SALVE – Microscopy), Microsc. Microanal. 16 (2010) 1702–1703. doi:10.1017/S1431927610060496.

[86] H.C. Nerl, A Combined Electron Microscopy and Computational Study on Cellular Uptake and Stability of Carbon Nanotubes, Imperial College London, 2012. http://hdl.handle.net/10044/1/10172.

[87] http://www.wikiwand.com/en/Transmission_electron_microscopy#/Optics, (2018).

[88] https://sites.google.com/site/bsatpati, (2018).

[89] C. Oprea, V. Ciupina, G. Prodan, Investigation of nanocrystals using TEM micrographs and electron diffraction technique, Rom. Reports Phys. 53 (2008) 223–230.

[90] http://www.globalsino.com, (2018).

[91] P. Hartel, M. Linck, F. Kahl, H. Müller, M. Haider, On Proper Phase Contrast Imaging in Aberration Corrected TEM, Microsc. Microanal. 20 (2014) 926–927. doi:10.1017/S1431927614006357.

[92] H. Rose, W. Wan, L. Berkeley, Aberration Correction in Electron Microscopy *, (2005) 44–48.

[93] M. Haider, H. Rose, S. Uhlemann, B. Kabius, K. Urban, Towards 0.1 nm resolution with the first spherically corrected transmission electron microscope, J. Electron Microsc. (Tokyo). 47 (1998) 395–405. doi:10.1093/oxfordjournals.jmicro.a023610.

[94] S. Uhlemann, M. Haider, Residual wave aberrations in the first spherical aberration corrected transmission electron microscope, Ultramicroscopy. 72 (1998) 109–119. doi:10.1016/S0304-3991(97)00102-2.

[95] D.B. Williams, C.B. Carter, Transmission Electron Microscopy, 1996. doi:10.1007/978-0-387-34758-5.

[96] T. Malis, S.C. Cheng, R.F. Egerton, EELS log-ratio technique for specimen-thickness measurement in the TEM, J. Electron Microsc. Tech. 8 (1988) 193–200. doi:10.1002/jemt.1060080206.

[97] C. Hébert, P. Schattschneider, H. Franco, B. Jouffrey, ELNES at magic angle conditions, Ultramicroscopy. 106 (2006) 1139–1143. doi:10.1016/j.ultramic.2006.04.030.

[98] H. Daniels, A. Brown, A. Scott, T. Nichells, B. Rand, R. Brydson, Experimental and theoretical evidence for the magic angle in transmission electron energy loss spectroscopy, Ultramicroscopy. 96 (2003) 523–534. doi:10.1016/S0304-3991(03)00113-X.

[99] S.D. Berger, D.R. McKenzie, P.J. Martin, EELS analysis of vacuum arc-deposited diamond-like films, Philos. Mag. Lett. 57 (1988) 285–290. doi:10.1080/09500838808214715.

[100] R.F. Egerton, P. Li, M. Malac, Radiation damage in the TEM and SEM, Micron. 35 (2004) 399–409. doi:10.1016/j.micron.2004.02.003.

[101] R.F. Egerton, Mechanisms of radiation damage in beam-sensitive specimens, for TEM accelerating voltages between 10 and 300 kV, Microsc. Res. Tech. 75 (2012) 1550–1556. doi:10.1002/jemt.22099.

[102] J.C. Meyer, F. Eder, S. Kurasch, V. Skakalova, J. Kotakoski, H.J. Park, S. Roth, A. Chuvilin, S. Eyhusen, G. Benner, A. V. Krasheninnikov, U. Kaiser, Accurate Measurement of Electron Beam Induced Displacement Cross Sections for Single-Layer Graphene, Phys. Rev. Lett. 108 (2012) 196102. doi:10.1103/PhysRevLett.108.196102.

[103] F. Banhart, Formation and transformation of carbon nanoparticles under electron irradiation, Philos. Trans. R. Soc. A Math. Phys. Eng. Sci. 362 (2004) 2205–2222. doi:10.1098/rsta.2004.1436.

[104] T. Füller, F. Banhart, In situ observation of the formation and stability of single fullerene molecules under electron irradiation, Chem. Phys. Lett. 254 (1996) 372–378. doi:10.1016/0009-2614(96)00338-7.

[105] B.W. Smith, D.E. Luzzi, Electron irradiation effects in single wall carbon nanotubes, J. Appl. Phys. 90 (2001) 3509–3515. doi:10.1063/1.1383020.

[106] J. Kotakoski, D. Santos-Cottin, A. V. Krasheninnikov, Stability of Graphene Edges under Electron Beam: Equilibrium Energetics versus Dynamic Effects, ACS Nano. 6 (2012) 671–676. doi:10.1021/nn204148h.

[107] K. Murakami, T. Kadowaki, J.I. Fujita, Damage and strain in single-layer graphene induced by very-low-energy electron-beam irradiation, Appl. Phys. Lett. 102 (2013). doi:10.1063/1.4790388.

[108] D. Teweldebrhan, A.A. Balandin, Modification of graphene properties due to electron-beam irradiation, Appl. Phys. Lett. 94 (2008) 013101. doi:10.1063/1.3062851.

[109] G. Liu, D. Teweldebrhan, A.A. Balandin, Tuning of Graphene Properties via Controlled Exposure to Electron Beams, IEEE Trans. Nanotechnol. 10 (2011) 865–870. doi:10.1109/TNANO.2010.2087391.

[110] S. Suzuki, K. Yamaya, Y. Homma, Y. Kobayashi, Activation energy of healing of low-energy irradiation-induced defects in single-wall carbon nanotubes, Carbon N. Y. 48 (2010) 3211–3217. doi:10.1016/j.carbon.2010.05.006.

[111] S. Suzuki, K. Kanzaki, Y. Homma, S. Fukuba, Low-Acceleration-Voltage Electron Irradiation Damage in Single-Walled Carbon Nanotubes, Jpn. J. Appl. Phys. 43 (2004) L1118–L1120. doi:10.1143/JJAP.43.L1118.

[112] W. Neng, L. Shuang-ying, X. Jun, M. Matteo, Z. Yi-long, W. Shu, S. Li-tao, H. Qing-an, Fullerene growth from encapsulated graphene flakes, Nanoscale. 6 (2014) 11213–11218. doi:10.1039/C4NR03680H.

[113] G. Algara-Siller, A. Santana, R. Onions, M. Suyetin, J. Biskupek, E. Bichoutskaia, U. Kaiser, Electron-beam engineering of single-walled carbon nanotubes from bilayer graphene, Carbon N. Y. 65 (2013) 80–86. doi:10.1016/j.carbon.2013.07.107.

[114] N. Lu, J. Wang, H.C. Floresca, M.J. Kim, In situ studies on the shrinkage and expansion of graphene nanopores under electron beam irradiation at temperatures in the range of 400–1200°C, Carbon N. Y. 50 (2012) 2961–2965. doi:10.1016/j.carbon.2012.02.078.

[115] M. Altissimo, E-beam lithography for micro-/nanofabrication, Biomicrofluidics. 4 (2010) 026503. doi:10.1063/1.3437589.

[116] https://www.protochips.com, (2008).

[117] A.C. Ferrari, J.C. Meyer, V. Scardaci, C. Casiraghi, M. Lazzeri, F. Mauri, S. Piscanec, D. Jiang, K.S. Novoselov, S. Roth, A.K. Geim, Raman Spectrum of Graphene and Graphene Layers, Phys. Rev. Lett. 97 (2006) 187401. doi:10.1103/PhysRevLett.97.187401.

[118] A.C. Ferrari, J. Robertson, Resonant Raman spectroscopy of disordered, amorphous, and diamondlike carbon, Phys. Rev. B. 64 (2001) 075414. doi:10.1103/PhysRevB.64.075414.

[119] F. Tuinstra, J.L. Koenig, Raman Spectrum of Graphite, J. Chem. Phys. 53 (1970) 1126–1130. doi:10.1063/1.1674108.

[120] M.M. Lucchese, F. Stavale, E.H.M. Ferreira, C. Vilani, M.V.O. Moutinho, R.B. Capaz, C.A. Achete, A. Jorio, Quantifying ion-induced defects and Raman relaxation length in graphene, Carbon N. Y. 48 (2010) 1592–1597. doi:10.1016/j.carbon.2009.12.057.

[121] A.C. Ferrari, J. Robertson, Raman spectroscopy of amorphous, nanostructured, diamond-like carbon, and nanodiamond, Philos. Trans. R. Soc. A Math. Phys. Eng. Sci. 362 (2004) 2477–2512. doi:10.1098/rsta.2004.1452.

[122] L.G. Cançado, K. Takai, T. Enoki, M. Endo, Y.A. Kim, H. Mizusaki, A. Jorio, L.N. Coelho, R. Magalhães-Paniago, M.A. Pimenta, General equation for the determination of the crystallite size La of nanographite by Raman spectroscopy, Appl. Phys. Lett. 88 (2006) 163106. doi:10.1063/1.2196057.

[123] L.G. Cançado, A. Jorio, M.A. Pimenta, Measuring the absolute Raman cross section of nanographites as a function of laser energy and crystallite size, Phys. Rev. B. 76 (2007) 064304. doi:10.1103/PhysRevB.76.064304.

[124] S. Plimpton, Fast Parallel Algorithms for Short-Range Molecular Dynamics, J. Comput. Phys. 117 (1995) 1–19. doi:10.1006/jcph.1995.1039.

[125] S.J. Stuart, A.B. Tutein, J.A. Harrison, A reactive potential for hydrocarbons with intermolecular interactions, J. Chem. Phys. 112 (2000) 6472–6486. doi:10.1063/1.481208.

[126] G. Henkelman, B.P. Uberuaga, H. Jónsson, A climbing image nudged elastic band method for finding saddle points and minimum energy paths, J. Chem. Phys. 113 (2000) 9901–9904. doi:10.1063/1.1329672.

[127] J.J.P. Stewart, MOPAC, Stewart Comput. Chem. Color. Springs, CO, USA, HTTP//OpenMOPAC.net (2016). (2016).

[128] J.J.P. Stewart, Optimization of parameters for semiempirical methods VI: more modifications to the NDDO approximations and re-optimization of parameters, J. Mol. Model. 19 (2013) 1–32. doi:10.1007/s00894-012-1667-x.

[129] A. Stukowski, Visualization and analysis of atomistic simulation data with OVITO–the Open Visualization Tool, Model. Simul. Mater. Sci. Eng. 18 (2010) 015012. doi:10.1088/0965-0393/18/1/015012.

[130] S. Jiang, T. Shi, X. Zhan, S. Xi, H. Long, B. Gong, J. Li, S. Cheng, Y. Huang, Z. Tang, Scalable fabrication of carbon-based MEMS/NEMS and their applications: A review, J. Micromechanics Microengineering. 25 (2015) 113001. doi:10.1088/0960-1317/25/11/113001.

[131] S. Sharma, A. Sharma, Y.K. Cho, M. Madou, Increased graphitization in electrospun single suspended carbon nanowires integrated with carbon-MEMS and carbon-NEMS platforms, ACS Appl. Mater. Interfaces. 4 (2012) 34–39. doi:10.1021/am2014376.

[132] C.N. Shyam Kumar, V.S.K. Chakravadhanula, A. Riaz, S. Dehm, D. Wang, X. Mu, B. Flavel, R. Krupke, C. Kübel, Understanding the graphitization and growth of free-standing nanocrystalline graphene using in situ transmission electron microscopy, Nanoscale. 9 (2017) 12835–12842. doi:10.1039/C7NR03276E.

[133] P.K. Chu, L. Li, Characterization of amorphous and nanocrystalline carbon films, Mater. Chem. Phys. 96 (2006) 253–277. doi:10.1016/j.matchemphys.2005.07.048.

[134] R.A. Rosenberg, P.J. Love, V. Rehn, Polarization-dependent C(K) near-edge x-ray-absorption fine structure of graphite, Phys. Rev. B. 33 (1986) 4034–4037. doi:10.1103/PhysRevB.33.4034.

[135] A.C. Ferrari, A. Libassi, B.K. Tanner, V. Stolojan, J. Yuan, L.M. Brown, S.E. Rodil, B. Kleinsorge, J. Robertson, Density, fraction, and cross-sectional structure of amorphous carbon films determined by x-ray reflectivity and electron energy-loss spectroscopy, Phys. Rev. B. 62 (2000) 11089–11103. doi:10.1103/PhysRevB.62.11089.

[136] T. Eberlein, U. Bangert, R.R. Nair, R. Jones, M. Gass, A.L. Bleloch, K.S. Novoselov, A. Geim, P.R. Briddon, Plasmon spectroscopy of free-standing graphene films, Phys. Rev. B - Condens. Matter Mater. Phys. 77 (2008) 1–4. doi:10.1103/PhysRevB.77.233406.

[137] P. Koskinen, S. Malola, H. Häkkinen, Evidence for graphene edges beyond zigzag and armchair, Phys. Rev. B. 80 (2009) 073401. doi:10.1103/PhysRevB.80.073401.

[138] J.M. Campanera, G. Savini, I. Suarez-Martinez, M.I. Heggie, Density functional calculations on the intricacies of Moiré patterns on graphite, Phys. Rev. B. 75 (2007) 235449. doi:10.1103/PhysRevB.75.235449.

[139] E. Cisternas, M. Flores, P. Vargas, Superstructures in arrays of rotated graphene layers: Electronic structure calculations, Phys. Rev. B. 78 (2008) 125406. doi:10.1103/PhysRevB.78.125406.

[140] T.G. Mendes-de-Sa, A.M.B. Goncalves, M.J.S. Matos, P.M. Coelho, R. Magalhaes-Paniago, R.G. Lacerda, Correlation between (in)commensurate domains of multilayer epitaxial graphene grown on

SiC(0001) and single layer electronic behavior, Nanotechnology. 23 (2012) 475602. doi:10.1088/0957-4484/23/47/475602.

[141] T. Uwanno, Y. Hattori, T. Taniguchi, K. Watanabe, K. Nagashio, Fully dry PMMA transfer of graphene on h -BN using a heating/cooling system, 2D Mater. 2 (2015) 041002. doi:10.1088/2053-1583/2/4/041002.

[142] A.W. Robertson, G.-D. Lee, K. He, Y. Fan, C.S. Allen, S. Lee, H. Kim, E. Yoon, H. Zheng, A.I. Kirkland, J.H. Warner, Partial Dislocations in Graphene and Their Atomic Level Migration Dynamics, Nano Lett. 15 (2015) 5950–5955. doi:10.1021/acs.nanolett.5b02080.

[143] J. Choe, Y. Lee, L. Fang, G.-D. Lee, Z. Bao, K. Kim, S_Direct imaging of rotating molecules anchored on graphene, Nanoscale. (2016) 1–4. doi:10.1039/C6NR04251A.

[144] A. Chuvilin, U. Kaiser, E. Bichoutskaia, N. a Besley, A.N. Khlobystov, Direct transformation of graphene to fullerene, Nat. Chem. 2 (2010) 450–3. doi:10.1038/nchem.644.

[145] T.W. Chamberlain, J. Biskupek, S.T. Skowron, A. V. Markevich, S. Kurasch, O. Reimer, K.E. Walker, G.A. Rance, X. Feng, K. Müllen, A. Turchanin, M.A. Lebedeva, A.G. Majouga, V.G. Nenajdenko, U. Kaiser, E. Besley, A.N. Khlobystov, Stop-Frame Filming and Discovery of Reactions at the Single-Molecule Level by Transmission Electron Microscopy, ACS Nano. 11 (2017) 2509–2520. doi:10.1021/acsnano.6b08228.

[146] X. Feng, S. Kwon, J.Y. Park, M. Salmeron, Superlubric Sliding of Graphene Nano fl akes on Graphene, ACS Nano. 7 (2013) 1718–1724. doi:10.1021/nn305722d.

[147] I. V. Lebedeva, A.A. Knizhnik, A.M. Popov, O. V. Ershova, Y.E. Lozovik, B. V. Potapkin, Fast diffusion of a graphene flake on a graphene layer, Phys. Rev. B - Condens. Matter Mater. Phys. 82 (2010) 1–10. doi:10.1103/PhysRevB.82.155460.

[148] A. El-Barbary, H. Telling, P. Ewels, I. Heggie, R. Briddon, Structure and energetics of the vacancy in graphite, Phys. Rev. B - Condens. Matter Mater. Phys. 68 (2003) 1–7. doi:10.1103/PhysRevB.68.144107.

[149] A.S. Barnard, I.K. Snook, Thermal stability of graphene edge structure and graphene nanoflakes, J. Chem. Phys. 128 (2008). doi:10.1063/1.2841366.

[150] E. Cisternas, J.D. Correa, Theoretical reproduction of superstructures revealed by STM on bilayer graphene, Chem. Phys. 409 (2012) 74–78. doi:10.1016/j.chemphys.2012.09.021.

[151] L. Wirtz, A. Rubio, The phonon dispersion of graphite revisited, Solid State Commun. 131 (2004) 141–152. doi:10.1016/j.ssc.2004.04.042.

[152] A. V. Krasheninnikov, F. Banhart, Engineering of nanostructured carbon materials with electron or ion beams, Nat. Mater. 6 (2007) 723–733. doi:10.1038/nmat1996.

[153] K. He, A.W. Robertson, C. Gong, C.S. Allen, Q. Xu, H. Zandbergen, J.C. Grossman, A.I. Kirkland, J.H. Warner, Controlled formation of closed-edge nanopores in graphene, Nanoscale. 7 (2015) 11602–11610. doi:10.1039/C5NR02277K.

[154] B. Song, G.F. Schneider, Q. Xu, G. Pandraud, C. Dekker, H. Zandbergen, Atomic-Scale Electron-Beam Sculpting of Near-Defect-Free Graphene Nanostructures, Nano Lett. 11 (2011) 2247–2250. doi:10.1021/nl200369r.

[155] T. Ma, W. Ren, X. Zhang, Z. Liu, Y. Gao, L.-C. Yin, X.-L. Ma, F. Ding, H.-M. Cheng, Edge-controlled growth and kinetics of single-crystal graphene domains by chemical vapor deposition, Proc. Natl. Acad. Sci. 110 (2013) 20386–20391. doi:10.1073/pnas.1312802110.

[156] S.K. Singh, M. Neek-Amal, F.M. Peeters, Electronic properties of graphene nano-flakes: Energy gap, permanent dipole, termination effect, and Raman spectroscopy, J. Chem. Phys. 140 (2014) 074304. doi:10.1063/1.4865414.

[157] R.F. Egerton, P. Li, M. Malac, Radiation damage in the TEM and SEM, Micron. 35 (2004) 399–409. doi:10.1016/j.micron.2004.02.003.

[158] C.R. Stoldt, C.J. Jenks, P.A. Thiel, A.M. Cadilhe, J.W. Evans, Smoluchowski ripening of Ag islands on Ag(100), J. Chem. Phys. 111 (1999) 5157–5166. doi:10.1063/1.479770.

[159] R.A. Budiman, H.E. Ruda, Smoluchowski ripening and random percolation in epitaxial Si1−xGex/Si(001) islands, Phys. Rev. B. 65 (2002) 045315. doi:10.1103/PhysRevB.65.045315.

[160] S.T. Gentry, S.F. Kendra, M.W. Bezpalko, Ostwald Ripening in Metallic Nanoparticles: Stochastic Kinetics, J. Phys. Chem. C. 115 (2011) 12736–12741. doi:10.1021/jp2009786.

[161] M. Jiao, W. Song, H.-J. Qian, Y. Wang, Z. Wu, S. Irle, K. Morokuma, QM/MD studies on graphene growth from small islands on the Ni(111) surface, Nanoscale. 8 (2016) 3067–3074. doi:10.1039/C5NR07680C.

[162] Y.-K. Chung, S.-A. Kim, J.-H. Koo, H.-C. Oh, E.-O. Chi, J.-H. Hahn, C. Park, Crystallization Behavior of Amorphous Si3N4 and Particle Size Control of the Crystallized α-Si3N4, J. Nanosci. Nanotechnol. 16 (2016) 5403–5409. doi:10.1166/jnn.2016.12220.

[163] D. Yoon, Y.-W. Son, H. Cheong, Negative Thermal Expansion Coefficient of Graphene Measured by Raman Spectroscopy, Nano Lett. 11 (2011) 3227–3231. doi:10.1021/nl201488g.

[164] J.Y. Huang, F. Ding, B.I. Yakobson, P. Lu, L. Qi, J. Li, In situ observation of graphene sublimation and multi-layer edge reconstructions, Proc. Natl. Acad. Sci. 106 (2009) 10103–10108. doi:10.1073/pnas.0905193106.

[165] P.J.F. Harris, Structural transformation of natural graphite by passage of an electric current, Carbon N. Y. 107 (2016) 132–137. doi:10.1016/j.carbon.2016.05.064

CURRICULUM VITAE

Personal Information

Name	:	Shyam Kumar Chethala Neelakandhan
Nationality	:	Indian
Date of birth	:	04-02-1986,
Place of birth	:	Kerala, India

Education:

PhD in Materials and Earth Sciences *2015-Present*
Technical University of Darmstadt, Darmstadt, Germany.

Master of Science in Metallurgical and Materials Engineering 2011-2014
Indian Institute of Technology-Madras, Chennai, Tamil Nadu, India.

Bachelor of Technology in Mechanical Engineering *2005-2009*
Amrita School of Engineering, Kollam, Kerala, India.

Additional research experience

Senior research fellow 2014-2015
Indian Institute of Technology Madras, Chennai, Tamil Nadu, India

List of publications:

Publications relevant to the thesis:

C. N. Shyam Kumar, M. Konrad, V. S. K.Chakravadhanula, S. Dehm, D.Wang, X.Mu, R. Krupke, C. Kübel, Nanocrystalline Graphene at high Temperatures: Insight into Nanoscale Processes, Nanoscale Advances 2019 (accepted)

S. Sharma, ***C. N. Shyam Kumar***, J.G. Korvink, C. Kübel, Evolution of Glassy Carbon Microstructure: In Situ Transmission Electron Microscopy of the Pyrolysis Process, Sci. Rep. 8 (2018) 16282.

C.N. Shyam Kumar, V.S.K. Chakravadhanula, A. Riaz, S. Dehm, D. Wang, X. Mu, B. Flavel, R. Krupke, C. Kübel, Understanding the graphitization and growth of free-standing nanocrystalline graphene using in situ transmission electron microscopy, Nanoscale. 9 (2017) 12835–12842.

Other publications:

C. Lutz, U. Bog, T. Loritz, J. Syurik, S. Malik, ***C.N.Shyam Kumar***, C. Kübel, M. Bruns, C. Greiner, M. Hirtz, H. Hölscher, Locally Controlled Growth of Individual Lambda-Shaped Carbon Nanofibers, Small. 1803944 (2019) 1803944.

C. Lutz, J. Syurik, ***C.N. Shyam Kumar***, C. Kübel, M. Bruns, H. Hölscher, Dry adhesives from carbon nanofibers grown in an open ethanol flame, Beilstein J. Nanotechnol. 8 (2017) 2719–2728.

H. Li, G. Gordeev, S. Wasserroth, V.S.K. Chakravadhanula, **S.K.C. Neelakandhan**, F. Hennrich, A. Jorio, S. Reich, R. Krupke, B.S. Flavel, Inner- and outer-wall sorting of double-walled carbon nanotubes, Nat. Nanotechnol. 12 (2017) 1176–1182.

C.N. Shyam Kumar, R. Bauri, D. Yadav, Wear properties of 5083 Al–W surface composite fabricated by friction stir processing, Tribol. Int. 101 (2016) 284–290.

R. Bauri, D. Yadav, ***C.N. Shyam Kumar***, B. Balaji, Tungsten particle reinforced Al 5083 composite with high strength and ductility, Mater. Sci. Eng. A. 620 (2015) 67–75.

C.N. Shyam Kumar, D. Yadav, R. Bauri, G.D. Janaki Ram, Effects of ball milling and particle size on microstructure and properties 5083 Al–Ni composites fabricated by friction stir processing, Mater. Sci. Eng. A. 645 (2015) 205–212.

R. Bauri, G.D.J. Ram, D. Yadav, ***C.N.Shyam Kumar***, Effect of Process Parameters and Tool Geometry on Fabrication of Ni Particles Reinforced 5083 Al Composite by Friction Stir Processing, Mater. Today Proc. 2 (2015) 3203–3211.

R. Bauri, D. Yadav, ***C.N. Shyam Kumar***, G.D. Janaki Ram, Optimized process parameters for fabricating metal particles reinforced 5083 Al composite by friction stir processing, Data Br.5 (2015) 309-3013.

C.N. Shyam Kumar, R. Bauri, Enhancing the phase stability and ionic conductivity of scandia stabilized zirconia by rare earth co-doping, J. Phys. Chem. Solids. 75 (2014) 642–650.

Acknowledgement

First, I would like to thank all my teachers, right from my primary school, who took me to the world of knowledge, supported me, trusted me, and transformed me academically and personally.

I express my sincere gratitude towards Prof. Christian Kübel for his continuous support. I thank him for his guidance and support starting from the application for the DAAD scholarship. His valuable support and guidance enabled me to successfully complete this thesis. I thank Prof. Ralf Krupke for his constant support and guidance throughout my thesis. He was always there guiding me during difficult situations. I am indebted to both of them for all the knowledge and experience I gained during my research stay at INT.

I would like to mention the great support from senior colleagues in Christian Kübel group, especially Kiran Chakravadhanula for his inputs in to my research and for introducing me to TEM. Also, I would like to sincerely thank Simone Dehm for her continuous support during my research period.

I would like to thank my colleagues and friends in INT. Those beautiful people around me, who made my research and life at INT memorable. Especially, I would like to thank all my colleagues in the research group of Christian Kübel and Ralph Krupke for all the help and support. Also, all other friends who supported me during my research stay at INT.

I would like to thank DAAD for the financial support during my PhD research.

Last but not the least, I would like to thank my parents, my brother, my in-laws for their continuous support. Special thanks to my wife, for tolerating me and for the continuous support throughout the time of this thesis.